INTERNAL OSCILLATIONS OF THE THERMOHALINE CIRCULATION AND ABRUPT CLIMATE CHANGES DURING THE LAST ICE AGE AND PERHAPS IN THE FUTURE

Ming Yang

A dissertation submitted to the faculty of the University of North Carolina at Chapel Hill in partial fulfillment of the requirements for the degree of Doctor of Philosophy in the Department of Geological Sciences.

Chapel Hill
2006

Approved by

Advisor: José A. Rial

Reader: John M. Bane Jr.

Reader: Adel Hanna

Reader: Christopher K. R. T. Jones

Reader: Stephen R. Meyers

Reader: Peter J. Robinson

ABSTRACT

MING YANG: Internal Oscillations of the Thermohaline Circulation and Abrupt Climate Changes during the Last Ice Age and Perhaps in the Future
(Under the direction of José A. Rial)

The first half of this dissertation presents a hypothesis to explain the abrupt climate changes that occurred during the last ice age. The Dansgaard-Oeschger (DO) oscillations are a prime example of abrupt climate changes in the paleoclimate record, clear evidence that large and extremely rapid climate fluctuations have repeatedly happened in the recent past. There is wide agreement that a likely driver for the DO oscillations may involve changes in the strength of the Atlantic thermohaline circulation (THC). A 3D coupled global atmosphere-ocean-sea-ice model of intermediate complexity, ECBilt-Clio, is used here to study the natural variability of the THC and associated climate changes in the North Atlantic. Under boundary conditions appropriate for the last glacial period the model simulations produce large amplitude, DO-like oscillations. Since no varying external forcing is applied, this is an internally driven, self-sustained, nonlinear free oscillation of the THC. It is argued that the free oscillation is caused by energy imbalance between the advection of cold water and the diffusion of heat by vertical turbulent mixing in the high latitude deep ocean. In addition, another hypothesis is proposed to explain the timing of the DO events. It is argued that the pattern is created by the Northern Hemisphere summer insolation, which modulates the free oscillating

mode of the THC. This speculation is supported by the ECBilt-Clio model, as well as an independent conceptual model SVO (Saltzman-van der Pol Oscillator). This hypothesis suggests that abrupt climate change is most likely to happen when insolation is rapidly changing. Since astronomical forcing is readily predictable, it is in principle possible to anticipate long-term (centennial to millennial), large amplitude, abrupt climate change events.

In the second half, the work from my secondary PhD project, which is totally independent from the aforementioned study, is presented. An inversion scheme is introduced to deduce subsurface crack model, namely crack strike, dip and crack density, by using shear-wave splitting polarization and delay time observations.

ACKNOWLEDGEMENTS

I would like to thank my advisor Dr. José Rial. His supervision and advice is invaluable. Dr. John Bane Jr., Dr. Adel Hanna, Dr. Christopher Jones, Dr. Stephen Meyers, and Peter Robinson served as committee members and helped me with their comments and questions.

I would especially like to thank my Dad and Mom for their support. I would also like to thank Ron Knight, Heggy Yoon, Phoebe Lee, Yue Hu and Nan Hao for their friendship.

I would like to thank the faculty, staff, and graduate students in the Department of Geological Sciences as well for their support during my years at Carolina.

This project is funded by NSF grant ATM-0241274 and by the U.S. Department of Energy grant DE-FG07-00ID1395.

TABLE OF CONTENTS

Page

LIST OF TABLES

LIST OF FIGURES

CHAPTER I

ABRUPT CLIMATE CHANGES

I.1 Introduction

I.1.1 The Problem

The current scientific debate about the sources of global warming has captured wide attention. The problem, essentially, is whether the observed twentieth century ~0.6°C global warming is due to the increasing atmospheric concentration of anthropogenic greenhouse gases, or is merely the warm phase of an episode of natural climate variability. Recent reconstructions of temperature variations during the last few millennia and numerical experiments reveal potential long-period warming events that almost reach present values during the middle ages (von Storch et al., 2004; Moberg et al, 2005). These findings contradict the widely popular "hockey stick" temperature variation of the last millennium proposed by Mann et al. (1998). In addition, the existence of frequent, abrupt, unpredictable 10-15^{o}C warming episodes during the last ice age suggests that a definitive answer as to the natural behavior of the climate system critically relies on a better understanding of its complex history (e.g., Rial et al., 2004).

How do we know the climate state in the distant past before the appearance of instrumental measurements? Nature provides its own recording mechanism. Among the

most important indicators of climate change is the stable oxygen isotope ratio $(^{18}O/^{16}O)$, measured as departures from a laboratory standard value by the general formula,

$$\delta^{18}O = \left[\frac{(^{18}O/^{16}O)_{\text{sample}}}{(^{18}O/^{16}O)_{\text{standard}}} - 1 \right] \times 10^3 \qquad \text{(I.1.1)}$$

in sedimentary cores (Saltzman, 2002). Dansgaard et al. (1971) argued that the $\delta^{18}O$ series measured in the deep ice are linearly related to the atmospheric temperature when the snow was formed in the clouds.

The stable isotope paleoclimate proxies $\delta^{18}O$ recorded in the ice cores of Greenland (GRIP, GISP2, NGRIP) are arguably the best available proxy data recording the past climate changes during the last 100 ky (1 ky = 1000 years). This data set shows abrupt regional air temperature increases of up to 15°C occurring in just a few decades or even a few years, both during the last glacial period and in the transition to the present interglacial (Severinghaus and Brook 1999). Following these rapid warming events there is a gradual cooling that lasts centuries to millennia, and then, abruptly again, the air temperature drops back to glacial values. This peculiar combination of temperature variations results in pulse-like time series with a distinctive saw-tooth appearance, commonly known as Dansgaard-Oeschger (DO) oscillations (Figure 1). Stable isotope proxy records show that at least 24 of these puzzling saw-toothed pulses, lasting between a few centuries and 4ky, occurred between 110 and 10 ky before the present (BP) (Dansgaard et al., 1982; Oeschger et al., 1984). The DO are best recorded in Greenland ice cores, but the extent of their influence may be global since highly correlated signals

have been detected in sediment cores taken off the coast of Africa (Zhao et al., 1995), in the subtropical Atlantic (Sachs and Lehman, 1999), in the Cariaco basin (Peterson et al. 2000), in the Arabian Sea (Schulz et al., 1998), and in the Hulu cave in China (Wang et al., 2001). In Antarctica, it is possible to identify DO-like features in the temperature proxy record (Jouzel et al., 1987; Bender et al., 1994), and the proxy data from many sites, especially those in the South Atlantic, reveal a hemispheric see-saw effect (cooling in the south while the north is warming). Furthermore, Bond and Lotti (1995) show that the rapid oscillations in air temperatures above Greenland is highly correlated with the iceberg calving cycles derived from North Atlantic deep ocean core records.

This study aims to gain insights into the mechanisms governing the recurrence of the intriguing DO events and the peculiar—and as yet unexplained—timing of the saw-tooth pulses of the DO over the last 100 ky.

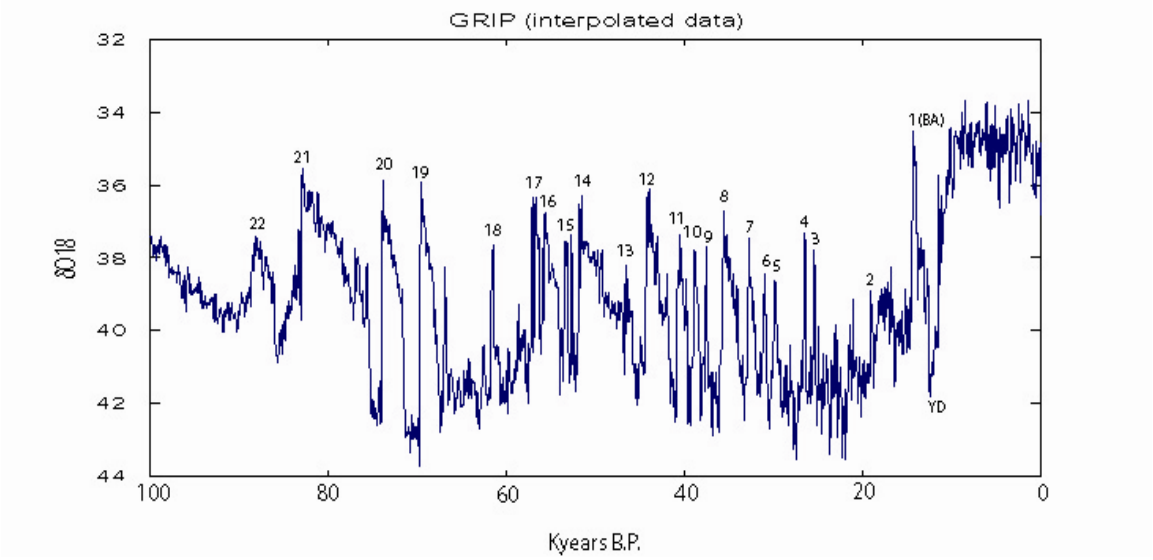

Figure 1. Record of $\delta^{18}O$ from the GRIP (Greenland Ice Core Project) core, a proxy for atmospheric temperature over Greenland, during the last 100,000 years. It shows numbered interstadials (the Dansgaard-Oeschger events), and the Bolling-Allerod (BA) and Younger Dryas (YD) events.

I.1.2 A review of Existing Hypotheses

The DO events are believed to be the result of instabilities, threshold crossings, and other types of nonlinear behavior of the climate system, but neither the physical mechanisms involved nor the nature of the nonlinearities is well understood (Dansgaard et al., 1993; Clark et al., 2002; Rial et al., 2004). During the past few decades, many important attempts to explain the DO oscillations and abrupt climate changes have been made, many of them involving the Atlantic thermohaline circulation (THC). The THC transports large amounts of heat northward to the high latitudes in the Atlantic Ocean and thus appears as a major factor in the climatic history of the Arctic and surrounding areas (Rahmstorf, 2002). (A detailed discussion of the THC will be presented later.) Since this study presents a new view of the THC and its connection with the DO, it is useful to briefly review the relevant literature. This follows the review paper by Rahmstorf (2002), who has divided the existing hypotheses into three categories.

The first category includes the concept of THC bistability (Broecker et al., 1985), which relates the DO events to a switch between two stable modes of the THC: during the warm interstadial mode, North Atlantic Deep Water (NADW) formation is active; whereas it is completely off during the cold stadial periods (see also Wang and Mysak, 2006). Some unknown outside trigger mechanism causes the transition between these two stable modes. Though this idea can be traced back to the bistability model in Stommel's classic paper (Stommel 1961), it is now somewhat contradicted by recent data from sediment cores showing that NADW formation is still on operation during the stadial phases and it shuts down only during or after Heinrich events (Sarnthein et al., 1994; Elliot et al., 2002).

The second category of hypotheses suggests the possibility of latitude shifts of convection between the Nordic Seas and the mid-latitude open Atlantic Ocean whereby the cold mode of the THC with NADW formation occurring south of Iceland is stable, while the warm circulation mode with NADW formation in the Nordic seas is only marginally stable, so that temporary transitions to this warm mode can be triggered (Ganopolski and Rahmstorf, 2001). The rapid warming thus results from a northward intrusion of warm and salty Atlantic water from the low latitudes into the Nordic Seas. Some external trigger is required to start the event, but as in the first category of hypotheses, the exact nature of the trigger remains unknown. Ganopolski and Rahmstorf (2002) have proposed that stochastic resonance can explain the timing of the DO (Alley et al., 2001), requiring a weak 1,500-year periodic signal amplified by random climatic variability. However, there is actually only small localized power at 1.5 ky in the DO as recorded in GRIP (Muller and MacDonald, 2002); just a few pulses with a period of ~1.5 ky and shorter exist in the time interval between 30 and 50ky BP. As shown in the spectrogram of the high-pass filtered GRIP time series (Figure 2), the high frequency power of the record is indeed concentrated at periods around 4ky.

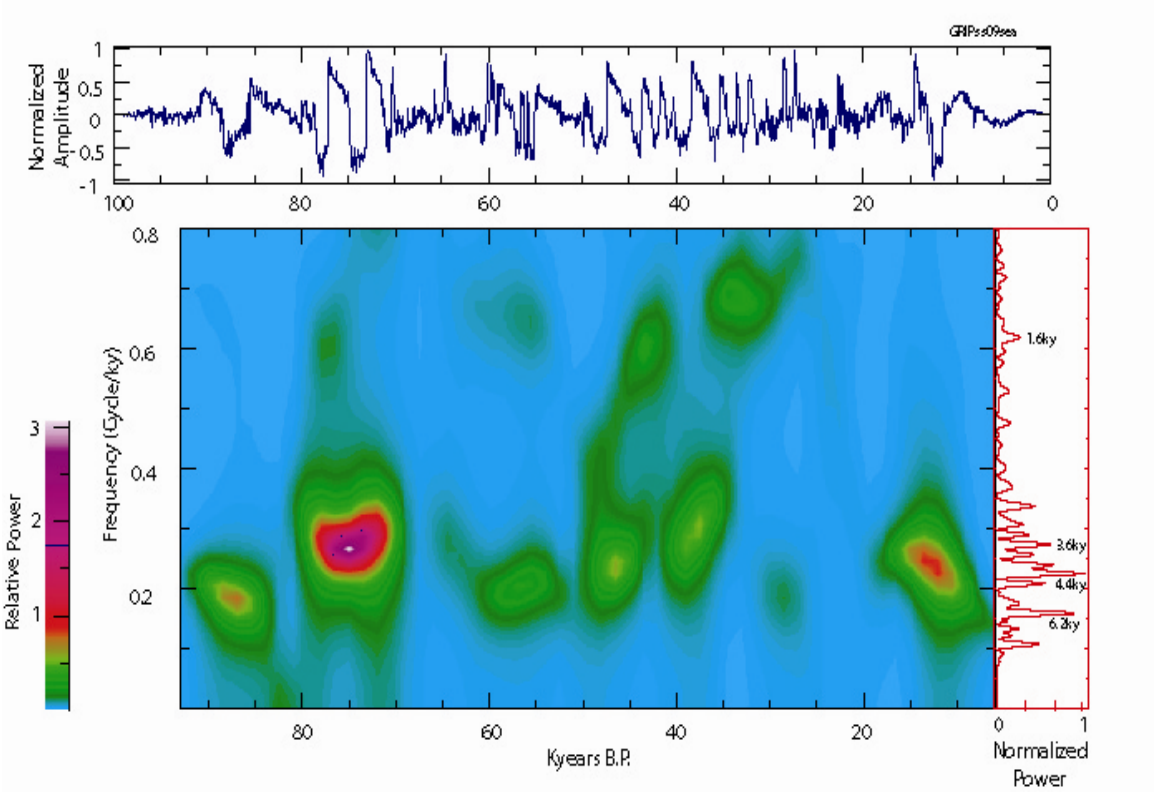

Figure 2. High-pass filtered normalized time series and spectrogram of the GRIP ice core climate proxy (age model ss09sea). The characteristic saw-tooth shaped DO oscillations are clearly displayed. Most of the power in the signal is centered around 0.25 cycles/ky.

Unlike the previous two, a third category of hypotheses attributes the DO events to internal oscillations of the THC, without invoking external triggers. One example is the salt oscillator (Broecker et al., 1990). This hypothesis is based on the notion that the Atlantic THC balances the net atmospheric freshwater export from the Atlantic basin. Several types of internal oscillations of the THC have been simulated in various ocean-alone models (e.g., Marotzke, 1990; Wright and Stocker, 1991; Weaver and Sarachik, 1991; Winton and Sarachik, 1993; Sakai and Peltier, 1996) with mixed boundary conditions (i.e., a restoring condition on sea surface temperature and flux condition on sea surface salinity). However, Zhang et al. (1993) and Power and Kleeman (1994) raised

serious doubts regarding the relevance of mixed boundary conditions for the dynamics of the coupled climate system. They argued that the occurrence of the internal oscillations of the THC is an artifact of mixed boundary conditions. Confronting this problem Winton (1997) and Sakai and Peltier (1997) were able to simulate millennial time scale oscillations, which they related to the observed DO cycles, by using a 2D ocean model coupled to an atmosphere energy balance model. Finally, Haarsma et al. (2001) reported for the first time the free oscillation of the THC under constant forcing in a realistic coupled ocean-atmosphere model. However, in their model the most significant mode of the internal oscillations happens in the Southern Hemisphere, and with a period more than 10ky, which makes it hard to relate to the DO oscillations that are primarily a millennial scale, North Atlantic phenomenon.

I.1.3 A Brief Overview

Two independent climate models have been used to understand the DO better. The primary one is a 3D coupled global climate model of intermediate complexity, ECBilt-Clio (Opsteegh et al., 1998; Goosse et al., 1999). The model simulations show that under constant glacial boundary conditions self-sustained nonlinear oscillations of the THC are excited by energy imbalance between the advection of cold water and the diffusion of heat by vertical and lateral turbulent mixing in the high latitude deep ocean. The differential heat flux alters the seawater temperature, which in turn adjusts the water density gradient in the deep ocean. As a result, a transition occurs every time the stability of the water column is destroyed or restored; this is a threshold-dependent, nonlinear, and

probably chaotic process (Yang and Rial, 2006). Moreover, the abruptness of the transition is exaggerated by the fast response time of sea ice and associated positive feedbacks. Unlike the results obtained by Haarsma et al. (2001), the free oscillation of the THC modeled here mainly happens in the northern North Atlantic at time scales comparable to those of the DO oscillations. Furthermore, accompanying the reorganization of the ocean circulation, the modeled atmosphere also experiences abrupt changes. This resembles many observed features of the DO events, such as the three-phase time evolution (fast warming, gradual cooling, and fast cooling), spatial pattern, and bipolar seesaw (Rahmstorf, 2002).

In order to investigate the variability of the THC throughout the last ice age, the model is forced by the theoretical solar insolation variation for the last 100 ky (Berger and Loutre, 1991). The resulting forced oscillation of air temperature in the North Atlantic shows similarities to the GRIP data shown before (Figure 1). This result suggests that the insolation forcing produces a modulation effect on the original signal that ends up looking like the GRIP data. This conclusion is further supported by an independent conceptual, simplified model consisting of a system of nonlinear differential equations called the SVO (Saltzman-van der Pol Oscillator). When forced by the theoretical solar insolation, the SVO model produces a signal which highly resembles the forced ECBilt-Clio simulation results as well as the observed GRIP proxy data. Therefore, this concludes that the observed train of DO pulses is the result of entrainment of the THC free oscillation by the astronomical changes in insolation during the last ice age. Since astronomical forcing is theoretically calculable, it is argued that it is possible to anticipate long-term large amplitude abrupt climate changes in the future (Rial and Yang, 2006).

I.2 The Climate Models

I.2.1 ECBilt-Clio

ECBilt-Clio version 3 is a global coupled atmosphere-ocean-sea-ice earth system model of intermediate complexity (EMIC). The atmosphere component, ECBilt, is a spectral, global, quasi-geostrophic model with simple parameterization for the diabatic heating due to radiative fluxes, the release of latent heat and the exchange of sensible heat with the surface (Opsteegh et al., 1998). The ocean component, Clio, is a free-surface ocean general circulation model (Deleersnijder and Campin, 1995; Campin and Goosse, 1999) coupled to a thermodynamic-dynamic sea ice model (Fichefet and Morales Maqueda, 1997). The following model description is summarized from the user manuals of ECBilt-Clio. (The model and the manuals are available at the website http://www.knmi.nl/ onderzk/CKO/ecbilt.html.)

I.2.1.1 The Atmosphere Component, ECBilt

The dynamical component of the atmospheric model, ECBilt, was developed by Marshall and Molteni (1993). The dynamical behavior is governed by the quasi-geostrophic equations, which are derived from the primitive equations under the assumption of small Rossby number $R_l = \frac{U}{fL} < 1$, where U and L are the characteristic velocity and length scales of the motion, respectively, and f is the Coriolis parameter. The basic equations written in isobaric coordinates are given below. For a detailed derivation the reader is referred to Holton (1979) and Pedlosky (1979).

The adiabatic core of the model is based on the following vorticity equation,

$$\frac{\partial \zeta}{\partial t} + \vec{V}_\varphi \cdot \nabla(\zeta + f) + f_0 D + k_d \nabla^8 \zeta = -F_\zeta \qquad \text{(I.2.1)}$$

where $\zeta = \nabla^2 \varphi$ is the vertical component of the vorticity vector, φ the stream-function, $\vec{V}_\varphi$ the rotational component of the horizontal wind velocity, D the divergence of the horizontal wind, f the Coriolis parameters, f_0 is f at 45^o north and south, $k_d \nabla^8 \zeta$ represents a highly scale selective diffusion, and F_ζ denotes the parameterized ageostrophic terms in the vorticity equation. F_ζ is expressed as

$$F_\zeta = \vec{V}_\chi \bullet \nabla(\zeta + f) + \zeta D + \omega \frac{\partial \zeta}{\partial p} + \vec{k} \bullet \nabla \omega \times \frac{\partial \vec{V}_\varphi}{\partial p} \qquad \text{(I.2.2)}$$

where $\vec{V}_x$ is the divergent component of the horizontal wind velocity, ω is the vertical velocity in isobaric coordinates. Estimates of F_ζ are used to represent the effect of the ageostrophic circulation on the tendency of the geostrophic vorticity.

The diabatic part of the model is based on the equation of the first law of thermodynamics, which reads,

$$\frac{\partial}{\partial t}(\frac{\partial \varphi}{\partial p}) + \vec{V}_\varphi \bullet \nabla(\frac{\partial \varphi}{\partial p}) + \frac{\sigma}{f_0}\omega + k_d \nabla^8(\frac{\partial \varphi}{\partial p}) + k_R(\frac{\partial \varphi}{\partial p}) = -\frac{RQ}{f_0 p c_p} - F_T \qquad \text{(I.2.3)}$$

where $\sigma = -\frac{\alpha}{\theta}\frac{\partial\theta}{\partial p}$ is the static stability, α is specific volume, θ is the potential temperature, k_R is a Rayleigh damping coefficient, R is the gas constant, p is pressure, c_p is the specific heat for a constant pressure, Q is the diabatic heating and F_T is the advection of temperature by the ageostrophic wind, which is expressed in terms of,

$$F_T = \vec{V}_\chi \bullet \nabla \frac{\partial \varphi}{\partial p} \tag{I.2.4}$$

In addition, the continuity equation reads,

$$D + \frac{\partial \varphi}{\partial p} = 0 \tag{I.2.5}$$

Equation (I.2.1), (I.2.3) and (I.2.5) can be combined into one equation for the quasi-geostrophic potential vorticity q by eliminating ω and D. It becomes,

$$\frac{\partial q}{\partial t} + \vec{V}_\varphi \bullet \nabla q + k_d \nabla^8 (q - f) + k_R \frac{\partial}{\partial p}\left(\frac{f_0^2}{\sigma}\frac{\partial \varphi}{\partial p}\right) = -\frac{f_0 R}{c_p}\frac{\partial}{\partial p}\left(\frac{Q}{\sigma p}\right) - F_\zeta - \frac{\partial}{\partial p}\left(\frac{f_0 F_T}{\sigma}\right) \tag{I.2.6}$$

where q is defined as:

$$q = \zeta + f + f_0^2 \frac{\partial}{\partial p}\left(\sigma^{-1}\frac{\partial \varphi}{\partial p}\right) \tag{I.2.7}$$

The ECBilt model is spectral with horizontal truncation T21, which means an approximately 5.6^o horizontal resolution. The model has three vertical levels, at 800 hPa, 500 hPa and 200 hPa respectively, on which the potential vorticity equation (I.2.1) is applied. The temperature equation (I.2.3) is applied at the intermediate levels at 650 hPa and 350 hPa. At the top of the atmosphere the rigid lid condition $\omega = 0$ is used. The

lower boundary condition for ω is

$$\omega_s = -\rho_s g(\frac{C_D}{f_0}\zeta_s - \vec{V}_{\varphi s} \bullet \nabla h) \tag{I.2.8}$$

where ω_s is the vertical motion field and ζ_s the vorticity at the bottom boundary layer, for which the values at 800 hPa are chosen, C_D is the surface drag coefficient, ρ_s is the density at the surface, $\vec{V}_{\varphi s}$ is the rotational velocity at the surface, and h is the orography height.

ECBilt simulates the changes in the specific humidity by using a single equation for the total precipitable water content between the surface and 500 hPa,

$$\frac{\partial q_a}{\partial t} = -\nabla_z \cdot (\vec{V}_a q_a) + E - P \tag{I.2.9}$$

where q_a is the total precipitable water content between the surface and 500 hPa, $\vec{V}_a$ the transport velocity for q_a, E evaporation and P precipitation. Above 500 hPa the atmosphere is assumed to be completely dry, and moisture which is advected through this plane by the vertical velocity is removed by precipitation. Below 500 hPa precipitation occurs when $q_a > 0.8 q_{\max}$, where $q_{\max}$ is the vertically integrated saturation specific humidity below 500 hPa. Water is precipitated in case of undersaturation because the precipitation criterion applies for grid-box averaged values for which complete saturation never will occur.

Therefore, the amount of precipitation Δq_a is calculated as

$$\Delta q_a = \frac{q_a - 0.8 q_{\max}}{1 + \frac{r \rho_w L_c g}{c_p \Delta p} \bullet \frac{dq_{\max}}{dT}} \tag{I.2.10}$$

where L_c is the latent heat of condensation, $r = \frac{q_a}{q_{\max}}$ is the relative humidity, and ρ_w is the density of water. The second term in the denominator is a correction to account for the heating of the lower atmospheric layer by the condensation of water vapor.

The evaporation over sea is given by

$$E_{sat} = \rho_a C_D \left|\vec{V}_s\right| (q_s(p_0, T_s) - q(p_0, T_*)) \tag{I.2.11}$$

where ρ_a is the air density, T_* is the temperature just above the surface.

The soil moisture content W is determined by precipitation Δq_a and evaporation E_w and runoff. Horizontal and vertical transport of soil moisture is neglected. The land surface is assumed to have a uniform soil moisture capacity $W_{\max}$. The soil moisture evaporation is linearly dependent on the soil moisture content

$$E_w = \frac{W}{W_{\max}} E_{sat} \tag{I.2.12}$$

If W becomes larger than $W_{\max}$, W is reset to $W_{\max}$ and the difference added to the river runoff. Therefore, the hydrological cycle in this model is closed.

ECBilt uses simplified parameterizations for the diabatic heating due to radiative fluxes (Figure 3). The diabatic heating is computed from various diabatic processes such as shortwave (SW) and longwave (LW) radiation and latent and sensible heating.

The incoming solar radiation Q_0 is given by

$$Q_0 = S_C \cos(Z) \tag{I.2.12}$$

where S_C is the solar constant and Z the daily average zenith angle.

The absorption of SW at the surface is given by

$$SW_s = (1 - r_s)(1 - \tau)(1 - r_a)Q_0 \qquad \text{(I.2.13)}$$

where r_a is the reflection coefficient at the top of the atmosphere, τ is the absorption coefficients and r_s the surface albedo. The parameters r_a and τ are given as functions of latitude and time of the year. The parameter r_s is determined by the surface characteristics. The different types of surface are land, snow, ocean and sea ice. The albedo for each surface type is a function of latitude and time of the year.

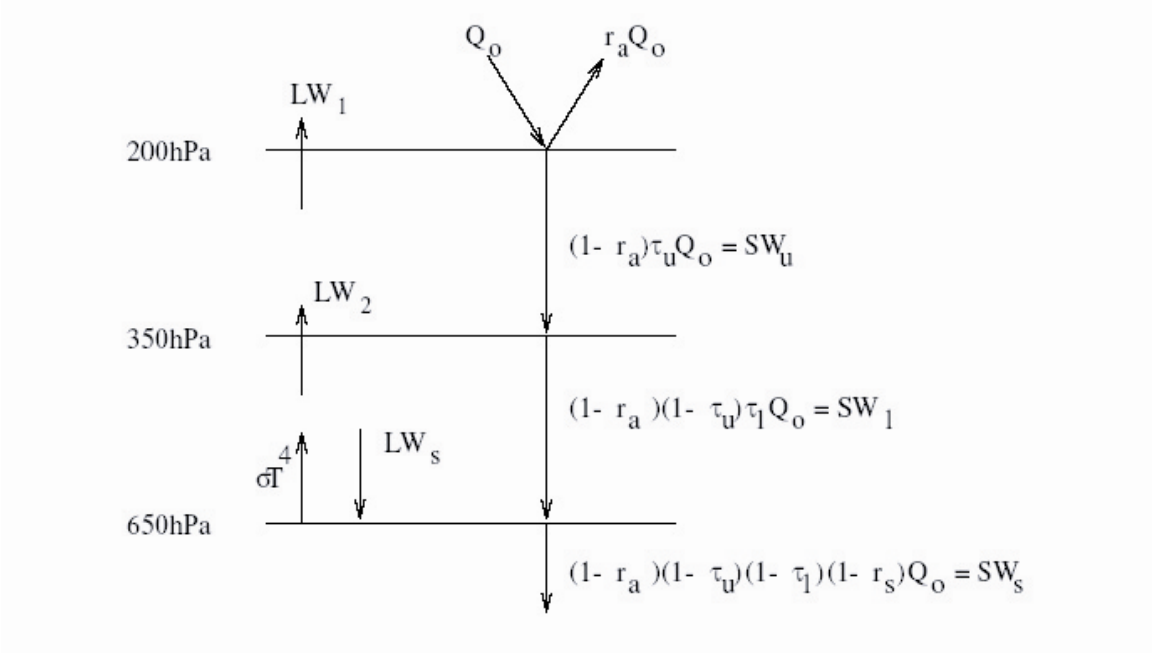

Figure 3. Radiation scheme of the atmospheric model (ECBilt). The subscripts u and l denote the upper and lower layer, and s the surface layer, respectively. Constant Q_0 is the incoming solar radiation, r_a is the planetary albedo and r_s is the surface albedo. Parameters τ_u and τ_l are the absorption coefficients in the upper and lower layers.

The LW radiation at the interface of the layers is computed according to the

parameterization of Held and Suarez (1978). The surface flux of sensible heat SH is expressed as

$$SH = \rho_a c_p C_d \left|\vec{V}\right|(T_s - T_*) \tag{I.2.14}$$

The release of latent heat due to precipitation is $L_c \Delta q_a$, while the cooling of the surface due to precipitation is $L_c E_w$.

The quasi-geostrophic equation (I.2.6) is solved using a fourth-order Runga-Kutta scheme. The physics is integrated using a forward scheme and is computed on grid-points at the Gaussian grid. The time step is 4 hours. As a result, synoptic variability associated with weather patterns is explicitly computed.

I.2.1.2 The Ocean-Sea Ice Component, Clio

The ocean component, Clio (Coupled Large-scale Ice Ocean), follows the work of Campin and Deleersnijder (Deleersnijder et al., 1993; Deleersnijder and Campin, 1995; Campin, 1997; Campin and Goosse, 1999), and Morales Maqueda and Fichefet (Morales Maqueda, 1995; Fichefet and Morales Maqueda, 1997). The equations governing large-scale geophysical flows are deduced from the Navier-Stokes equations written in rotating coordinates with some classical approximations (Gill, 1982; Cushman-Roisin, 1994; Campin, 1997):

- the Boussineq approximation, which states that the variation of the density ρ are small compared to its mean ρ_0;
- the depth of the ocean is assumed negligible compared to the Earth's radius; the vertical depth scale is supposed much shorter than the horizontal one;

- the hydrostatic approximation.

Those primitive equations, written for the horizontal velocity $\vec{u}$, the vertical velocity w, the potential temperature θ, and the salinity S, are:

the continuity equation:

$$\frac{\partial w}{\partial z} + \nabla_h \cdot \vec{u} = 0 \tag{I.2.15}$$

the horizontal momentum equation:

$$\frac{\partial \vec{u}}{\partial t} + \vec{u} \cdot \nabla_h \vec{u} + w\frac{\partial \vec{u}}{\partial z} + f\vec{e}_z \times \vec{u} = -\frac{1}{\rho_0}\nabla_h p + \vec{F}_{du} \tag{I.2.16}$$

the vertical momentum equation:

$$\frac{\partial p}{\partial z} = -\rho g \tag{I.2.17}$$

the equations for the evolution of θ and S:

$$\frac{\partial \theta}{\partial t} + \vec{u} \cdot \nabla_h \theta + w\frac{\partial \theta}{\partial z} = F_{d\theta} + F_{v\theta} \tag{I.2.18}$$

$$\frac{\partial S}{\partial t} + \vec{u} \cdot \nabla_h S + w\frac{\partial S}{\partial z} = F_{dS} \tag{I.2.19}$$

and the equation of state:

$$\rho = \rho(\theta, S, z) \tag{I.2.20}$$

where $F_{v\theta}$ is the volume source of temperature due to the absorption of solar radiation in the ocean interior. F_{du}, $F_{d\theta}$ and F_{dS} account for the effects of small-scale processes, not explicitly resolved by the model.

The parameterization of vertical mixing used in Clio follows Kantha and Clayson (1994) version of Mellor and Yamada's level 2.5 model (Mellor and Yamada, 1982). For a detailed discussion, the reader is referred to the paper by Goosse et al. (1999).

The grid resolution and the approximations used to simplify the equations (mainly the hydrostatic approximation) do not allow having explicit description of strong convection. This problem is generally tackled by introducing a convective adjustment scheme. The scheme applied in this model consists in increasing the vertical diffusivity whenever the density profile is statically unstable.

The most natural way to discretize equations on the Earth is to use spherical polar coordinates. However, in this normal grid, there is a singularity at the North Pole. The method used here to avoid this problem is use two spherical subgrids, for which the poles are not located in the oceanic domain covered by the grid (Figure 4). The first one is based on classical longitude-latitude coordinates. It covers the Southern Ocean, the Pacific Ocean, the Indian Ocean and the South Atlantic. The second spherical subgrid has its poles located at the equator, the "north pole" in the Pacific (111^{o}W) and the "south pole" in the Indian Ocean (69^{o}E). The North Atlantic and the Arctic are represented on

this “rotated” grid. The two subgrids are connected in the equatorial Atlantic where there is a correspondence between the meridians of the South Atlantic on one grid and the parallel of the other grid in the North Atlantic (Deleersnijder et al., 1993; Campin, 1997). The horizontal resolution is $3° \times 3°$. In the model, the two subgrids are considered as a single coordinate system using metric coefficients which are given by Deleersnijder et al. (1993) and Campin (1997).

The model has 20 vertical layers (Table 1) and the vertical discretization follows the simple so-called “z-coordinate” (Campin, 1997). This means that the depth of each level is fixed as well as the location of the interface between levels. It is necessary to have a relatively fine resolution close to the ocean surface to obtain a good representation of the strong gradients that occur there. The bottom of the ocean is considered as a succession of steps, at each point the number of active levels being chosen to have the best correspondence between the model depth and the real ocean depth. Therefore, the model has a realistic bathymetry.

Table1. Depth and thickness of the vertical layers in the ocean model Clio.

Level	Depth of the center (m)	Thickness of the level (m)	Location of the bottom interface (m)
20	5.00	10.00	10.00
19	15.98	11.96	21.96
18	29.17	14.42	36.38
17	45.20	17.64	54.02
16	64.96	21.88	75.90
15	89.75	27.70	103.64
14	121.52	35.86	139.44
13	163.28	47.68	187.12
12	219.86	65.48	252.60
11	299.26	93.38	345.98
10	415.07	138.18	484.16
9	588.88	209.44	693.60
8	850.19	313.18	1006.78
7	1225.11	436.66	1443.44
6	1717.90	548.92	1992.36
5	2307.36	630.00	2622.36
4	2963.25	581.78	3304.14
3	3661.11	713.94	4018.08
2	4385.22	734.28	4752.36
1	5126.18	747.64	5500.00

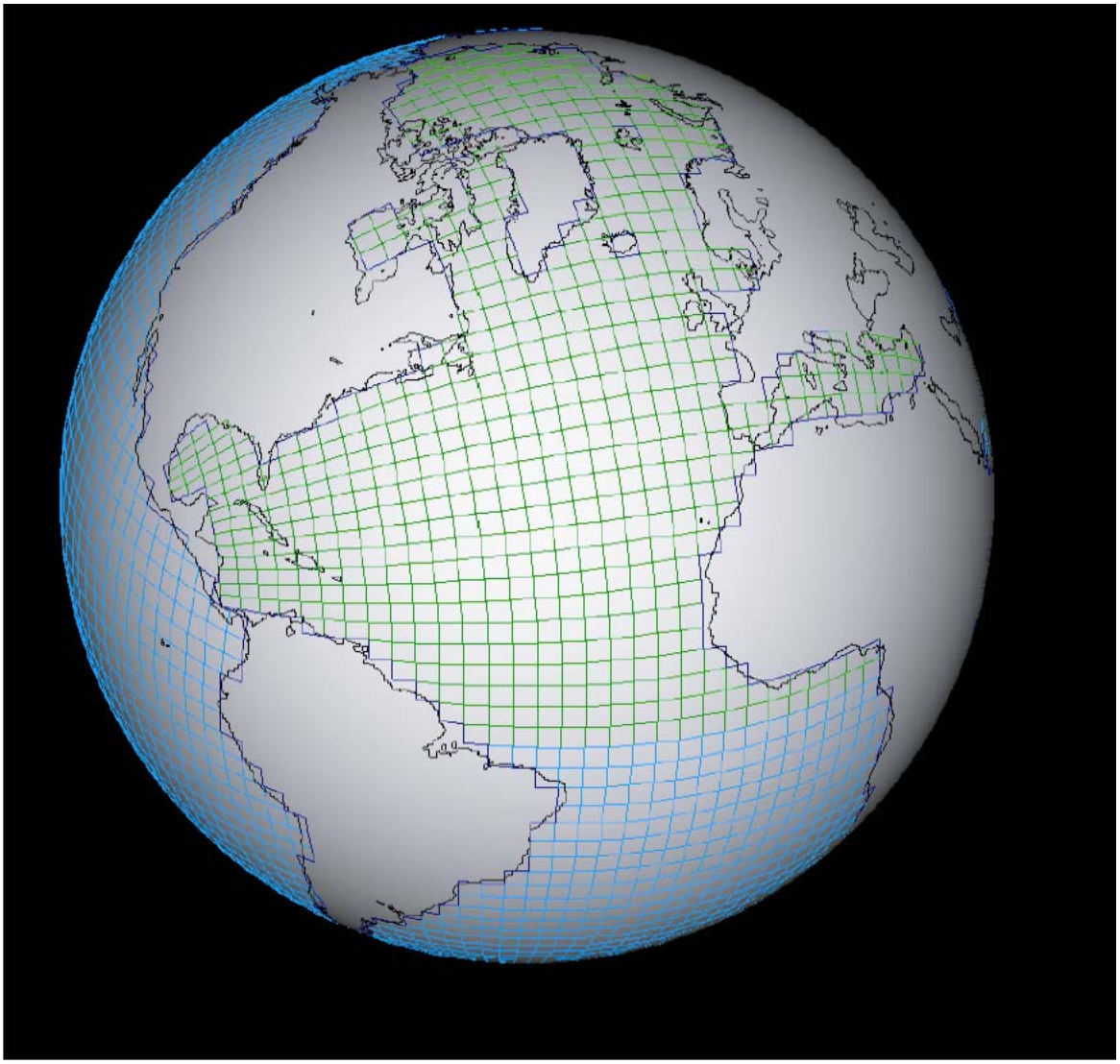

Figure 4. The horizontal grid. The view is centered on the Atlantic. The two spherical subgrids (the blue grid denotes the first one and the green grid the second) are connected in the Atlantic at the "geographical equator" (Campin, 1997).

The sea ice component is a 3-layer dynamic-thermodynamic model that simulates the changes of snow and ice thickness in response to surface and bottom heat fluxes. The thermodynamic part governs the thermodynamic growth or decay of the ice, which can be considered to depend only on the vertical response of the ice layer to the exchanges with the atmosphere and the ocean. Horizontal thermodynamic processes, such as horizontal

heat conduction through ice, can be safely neglected because of the much larger horizontal scales. On the other hand, ice dynamics and transport can be considered at large scales as horizontal processes. This distinction between thermodynamics and dynamics is purely formal since they are intrinsically coupled.

I.2.1.3 The Coupled Model

The individual atmosphere, ocean and sea ice components are coupled by exchanging momentum, freshwater and heat. The time step of the atmospheric model is 4 hours, whereas the ocean and sea ice model has a time step of 1 day, implying 6 atmosphere time steps for one ocean time step. During these 6 time steps the ocean surface is kept constant. The exchanges of momentum, freshwater and heat fluxes take place every model day. The coupled model configuration is illustrated in Figure 5.

The main advantage of ECBilt-Clio is its computational efficiency (this model runs on a 2.8GHz IBM Xeon processor, taking less than five days to complete a 1000 model year integration). It still provides a realistic representation of the large scale dynamics. Given the long time scales involved in this study, this model is among the most complex climate models available at present (Knutti et al., 2004).

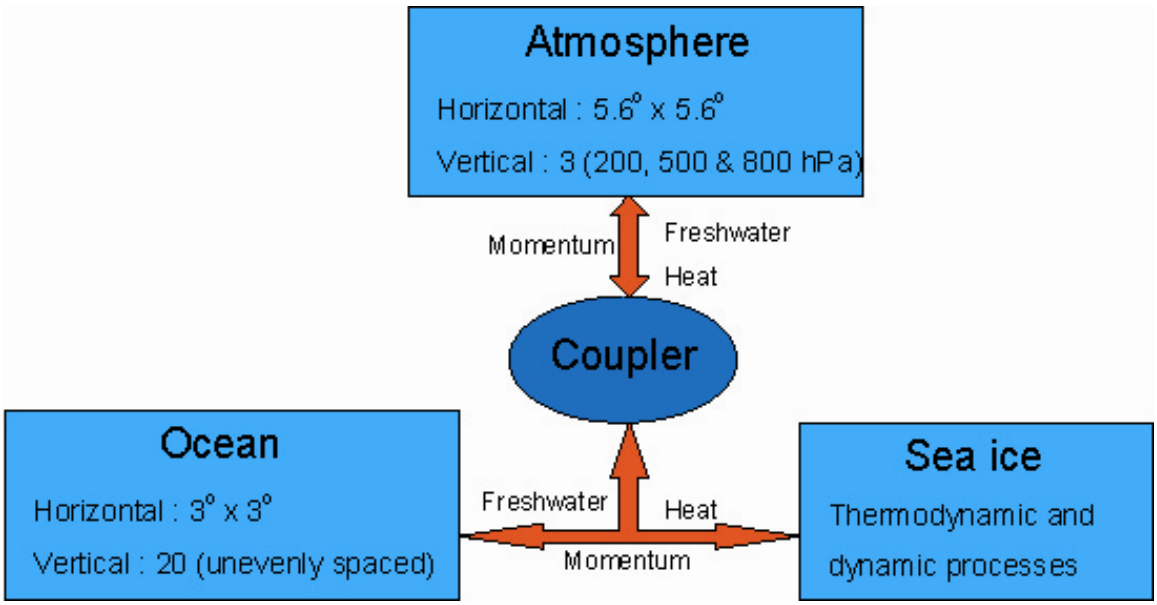

Figure 5. The ECBilt-Clio model configuration. The individual components are coupled by exchanging momentum, freshwater and heat fluxes every model day. The simulations are performed with weak fresh water flux correction.

I.2.1.4 Model Performance

In order to evaluate the performance of ECBilt-Clio model, Justino (2005) integrated the model for 10,000 years using early industrial atmospheric CO_2 concentration (289 ppm) and present-day orbital parameters, albedo and topography as the boundary conditions. The simulation results were compared to NCEP/NCAR Reanalysis data (NCEP 2002). This analysis revealed that although the atmospheric model is relatively simple, ECBilt-Clio is capable to reproduce the large scale dynamics of global climate satisfactorily. Therefore, it is appropriate to use this model to examine the sensitivity of a particular climatic process across a wide range of boundary conditions (Justino, 2005).

In fact, many authors have used ECBilt-Clio to study the variability and stability of the THC from decadal to millennial time scales under various conditions. For instance, Goosse et al. (2002) performed a multi-millennial integration under constant pre-industrial forcing to study the natural modes of the THC in the North Atlantic. They ascribe the simulated instabilities of THC as the cause of the well-documented abrupt cooling event observed during the early Holocene. Knutti et al. (2004) used the model to investigate the stability of the THC under varying external forcing. By imposing prescribed fresh water forcing into the North Atlantic basin, they closely reproduced the evolution of air temperature over Greenland between 60 to 25 ky BP.

I.2.2 The Saltzman-van der Pol Oscillator (SVO)

Theoretically, the interaction among ocean temperature, sea ice, and greenhouse gas (GHG) feedbacks in a glacial atmosphere creates a nonlinear, self-sustained thermal oscillator with millennial-scale period, as described in detail by Saltzman and Moritz (1980) and Saltzman (2002). When sea ice retreats (thawed by the slowly accumulating ocean's heat underneath), albedo decreases, heat is released from the ocean, and positive feedbacks of water vapor, carbon dioxide and methane (the latter from the ice-free land areas surrounding the Arctic Ocean) rapidly warm the atmosphere. Abrupt warming in turn triggers negative feedbacks that gradually drive the temperature back to near glacial levels, for instance, by increasing cloud formation seaward from the ice edge or increasing freshwater flux into the Arctic Ocean. When the temperature reaches a threshold where the ocean surface layer is cold enough for CO_2 uptake by the ocean to

resume and methane emissions to slow down or stop, sea ice will rapidly advance to close the lid on the ocean's heat supply. This sequence of events is consistent with the saw-tooth shape of the temperature proxies in the ice core time series.

SVO is derived from a coupled system of two nonlinear first order differential equations and the variables in the equations represent the displacements of the sea ice edge, a proxy for atmospheric surface temperature, and the mean ocean temperature (Rial and Yang, 2006). The interaction between them creates the nonlinear, self-sustained thermal oscillator with millennial scale period.

The equations for the sea ice thermal oscillator are written as follows:

$$\frac{d\theta}{dt} = -\psi_1\eta + \psi_2\theta - \psi_3\eta^2\theta \tag{I.2.21}$$

$$\frac{d\eta}{dt} = \phi_1\theta - \phi_2\eta \tag{I.2.22}$$

where η and θ are the *departures from the mean* (equilibrium) of sea ice extent and ocean temperature respectively. The variable η is the sine of the sea ice edge's latitude with respect to the mean. The constants ϕ_i and ψ_i are all positive and $\psi_2\phi_2 < \psi_1\phi_1$ so that the only real fixed point of the system is the origin. The first two terms on the RHS (right hand side) of the equation for η and the first term in the RHS of the equation for θ together model harmonic oscillations. These result from both the insulating and reflecting effects of the sea ice, e.g., as the ocean warms sea ice retreats (and albedo decreases), warming the ocean further, and as the ocean cools, sea ice advances (and albedo increases), making the still uncovered ocean cooler. On the other hand, as sea ice covers

the ocean, it insulates the heat loss from ocean to atmosphere, the ocean warms; and when sea ice retreats it releases heat and cools. The combination of these positive and negative feedbacks results in a harmonic oscillation with frequency $(1/2\pi)\,(\phi_1\psi_1)^{1/2}$, while the term $\phi_2\eta$ adds physically realistic (small) damping to the harmonic oscillations. The destabilizing effect of the term $\psi_2\theta$ accounts for heat flux from the ocean and GHG positive feedbacks, e.g., a warm, suddenly uncovered ocean releases heat and promotes higher GHG concentrations (water and CO_2) that warm the atmosphere, possibly triggering methane release from ice-free land, which warms the atmosphere further, and so on.

The $-\eta^2\theta$ term accounts for the nonlinear contribution of vertical heat flux at the surface (the linear part is the term $-\psi_1\eta$). This nonlinear restoring mechanism (negative feedback) dominates when η is large and of either sign. (It prevents the ice advance from reaching the equator, or from disappearing completely when it retreats towards the pole.) With the adopted parameters the maximum and minimum latitudes reached by the sea ice edge are 85°N and 45°N respectively. Equations (I.2.21) and (I.2.22) lead to a Liénard-type equation, which has a unique periodic solution with stable limit cycle when the damping coefficient ϕ_2 is small or zero. A stable limit cycle is the most physically reasonable solution because it has a measurable period and is stable under perturbation. With small damping, equations (I.2.21) and (I.2.22) reduce to a homogeneous van der Pol equation with $\xi = (\psi_3/\psi_2)^{1/2}\,\eta$. This variable can be used as a proxy for surface temperature. The astronomically forced equation can be written

$$\frac{d^2\xi}{dt^2} - \psi_2[1-\xi^2]\frac{d\xi}{dt} + \Omega^2\xi = AM(t) \qquad \text{(I.2.23)}$$

where $A = a\phi_1(\psi_3/\psi_2)^{1/2}$, a is the amplitude of the insolation forcing function *M(t)*. Equation (I.2.23) is the SVO model. The van der Pol equation represents relaxation oscillations such as found in many nonlinear systems in physics, engineering and biology. In the present case the climate system begins to relax back to the glacial state after the sea ice cover is melted by the ocean's heat. The equation exhibits two distinct and characteristic phases or states: one in which energy is being slowly stored and one in which energy is discharged suddenly when a threshold is crossed.

Abruptness in SVO is directly related to coefficient ψ_2, which controls the nonlinearity of the van der Pol equation (Figure 6) and represents (albeit crudely) GHGs and ice-albedo positive feedbacks. As shown in the figure, increasing ψ_2 creates increasingly sharper temperature changes that resemble the abrupt events at the beginning and end of individual DO pulses. Figure 7 illustrates the phase space of η and θ.

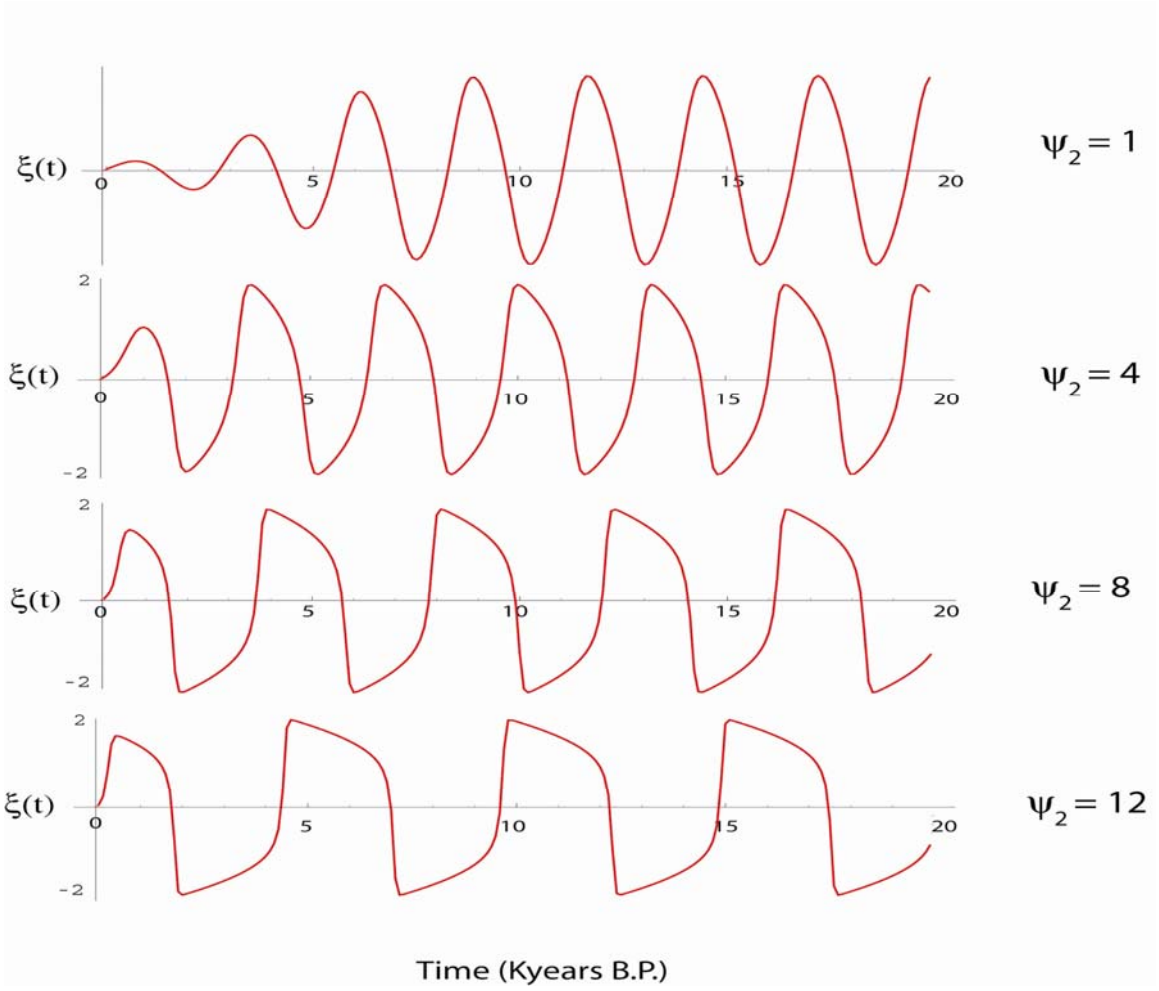

Figure 6. Increasing the coefficient ψ_2 increases the nonlinearity of the van der Pol equation, which results in an increase of the abruptness and of the period of the simulated DO pulses, as shown in the Figure 1.

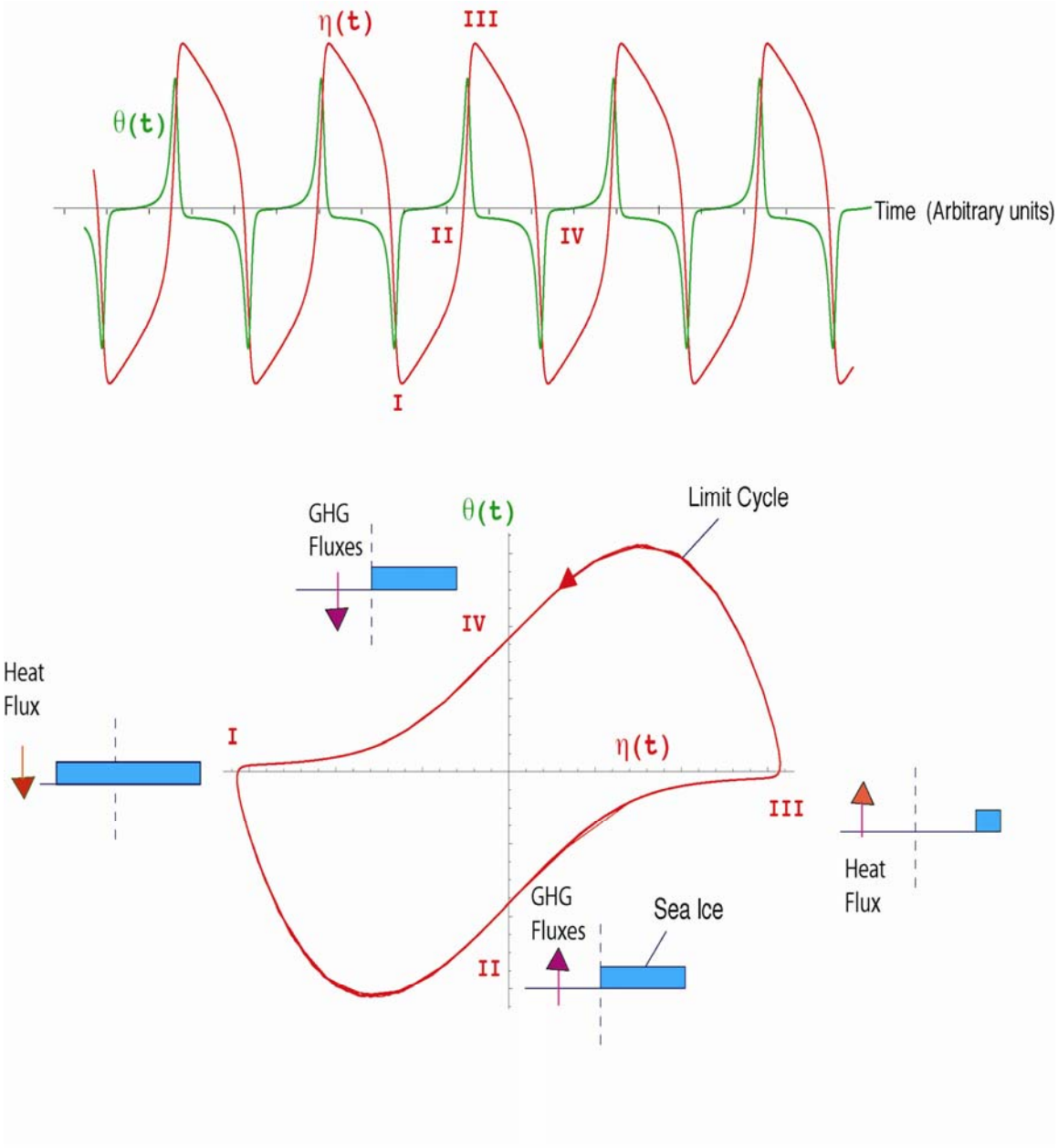

Figure 7. The $\eta-\theta$ phase space representation of equations (2.21) consists of a limit cycle to which all initial conditions (inside or outside the cycle) are attracted after a perturbation. The shape of the limit cycle (and thus the shape of the time series) is controlled by the nonlinearity coefficient ψ_2, as shown in the previous figure. Main stages of the sea ice extent are labeled I-IV and shown in the time series. As ψ_2 increases (GHG fluxes and feedback intensity increase) the limit cycle trajectory develops horizontal straight segments (vertical jumps in the time series) that represent the abrupt advance or retreat of the sea ice edge. Note that time runs from left to right.

I.3 Modeling the Abrupt Climate Change

I.3.1 Experimental Design

To study the variability of the THC within diverse climate states, three basic numerical experiments were designed. The first one is a PI (pre-industrial) simulation. With the default boundary conditions, the model produces results consistent with the interglacial climate before 1850 (pre-industrial) (Justino, 2005). The simulated climate in this experiment acts as a control climate for the other simulations.

The second experiment is an LGM (Last Glacial Maximum) simulation. In order to simulate the LGM climate the Paleoclimate Modeling Intercomparison Project (Joussaume and Taylor, 1995) recommends modifying four major boundary conditions in ECBilt-Clio: orbital parameters, greenhouse gas (GHG) concentration, surface albedo, and topography. Based on previous experience from coupled LGM simulations, the effect of sea level change due to the existence of continent ice sheets is neglected here (Justino, 2005). Furthermore, due to the large uncertainties in the ice sheet mass balance during the last glacial period (Marshall and Clark, 1999), ablation processes and changes of the ice sheet runoff are also disregarded.

Changes of the orbital parameters (eccentricity, obliquity and precession) adjust the amount of solar radiation that reach the top of the atmosphere, and thus have a direct impact on the global climate system (Table 2). We will address this issue in detail later.

Paleo proxy data reveal that during the LGM the atmospheric CO_2 concentration is lower than its pre-industrial value (Table 2). The other two prominent changes referring to land albedo and topography mainly due to the extensive continental ice sheet.

In this study, the land albedo is derived from a reconstructed LGM vegetation (Crowley, 1995) where the deforested soils and plant cover are replaced by their respective albedos (Figure 8). Although land cover in the LGM is uncertain, Adam and Fauré (1997) suggest that the rainforest may have had one third or less of its coverage today. The difference is also observed over Eurasia where the actual forest has changed to desert, semi-desert and tundra. Furthermore, as a result of the changes from present-day sand desert and barren land to desert during the LGM, northern African and southern Australian albedo have been reduced (Justino, 2005).

The LGM ice sheet topography is based on the ICE-5G model calculated by Peltier (2004). Figure 9 reveals the comparison of topography in pre-industrial and LGM. Note that in order to implement the albedo and topography data files into the model, they have to be interpolated to T21 resolution.

The inclusion of the continent ice sheet in North America and Europe increases the land surface albedo by more than 60% in those areas. Moreover, the ice caps create topographic barriers to atmospheric flow of about 2000 m. As discovered by Justino (2005), they will have a large impact on the atmospheric circulation. Later, we will also see that the topography also plays an important role on the variability of climate in the North Atlantic.

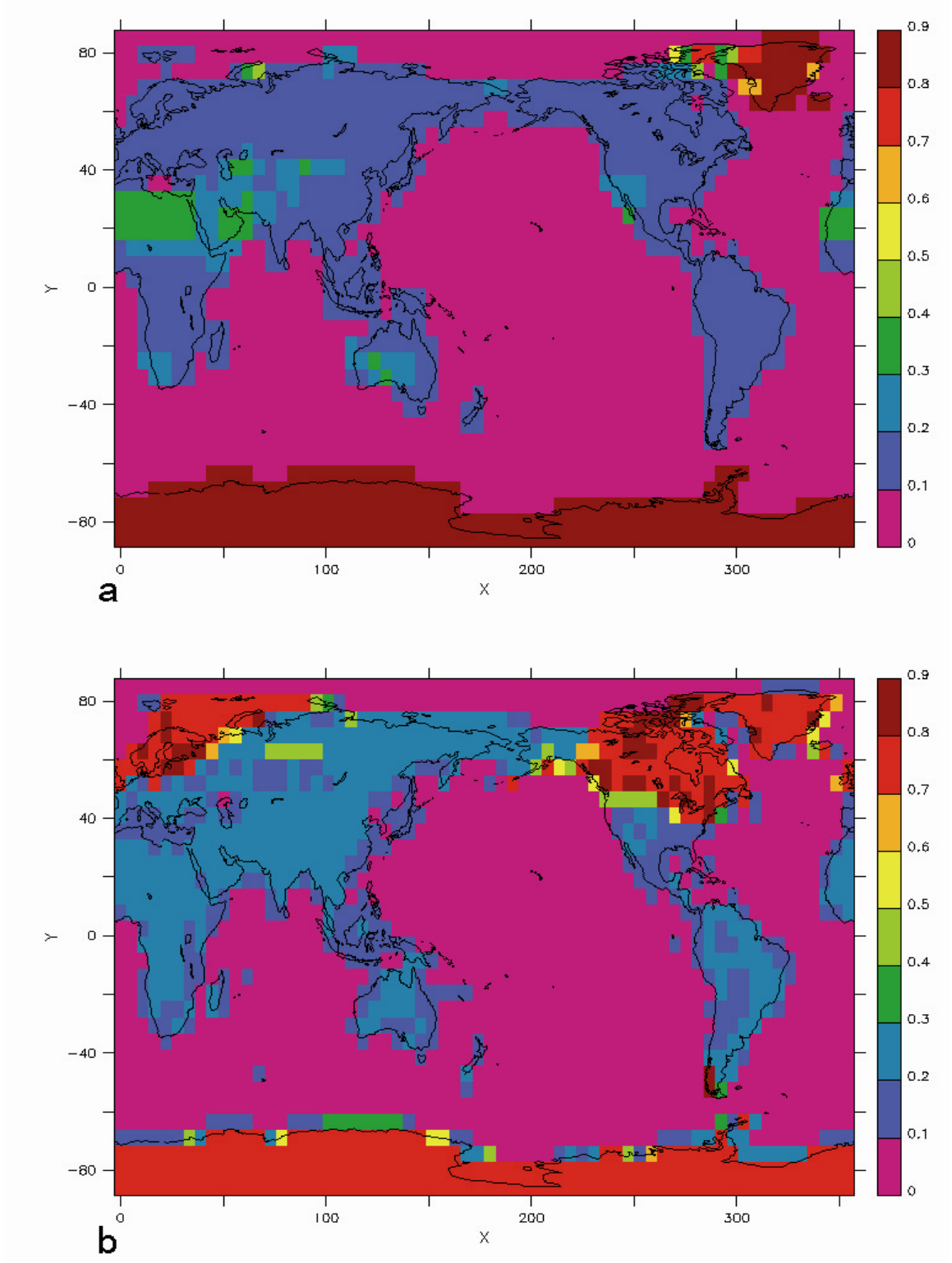

Figure 8. The global distribution of land surface albedo a) at pre-industrial (PI); b) at Last Glacial Maximum (LGM).

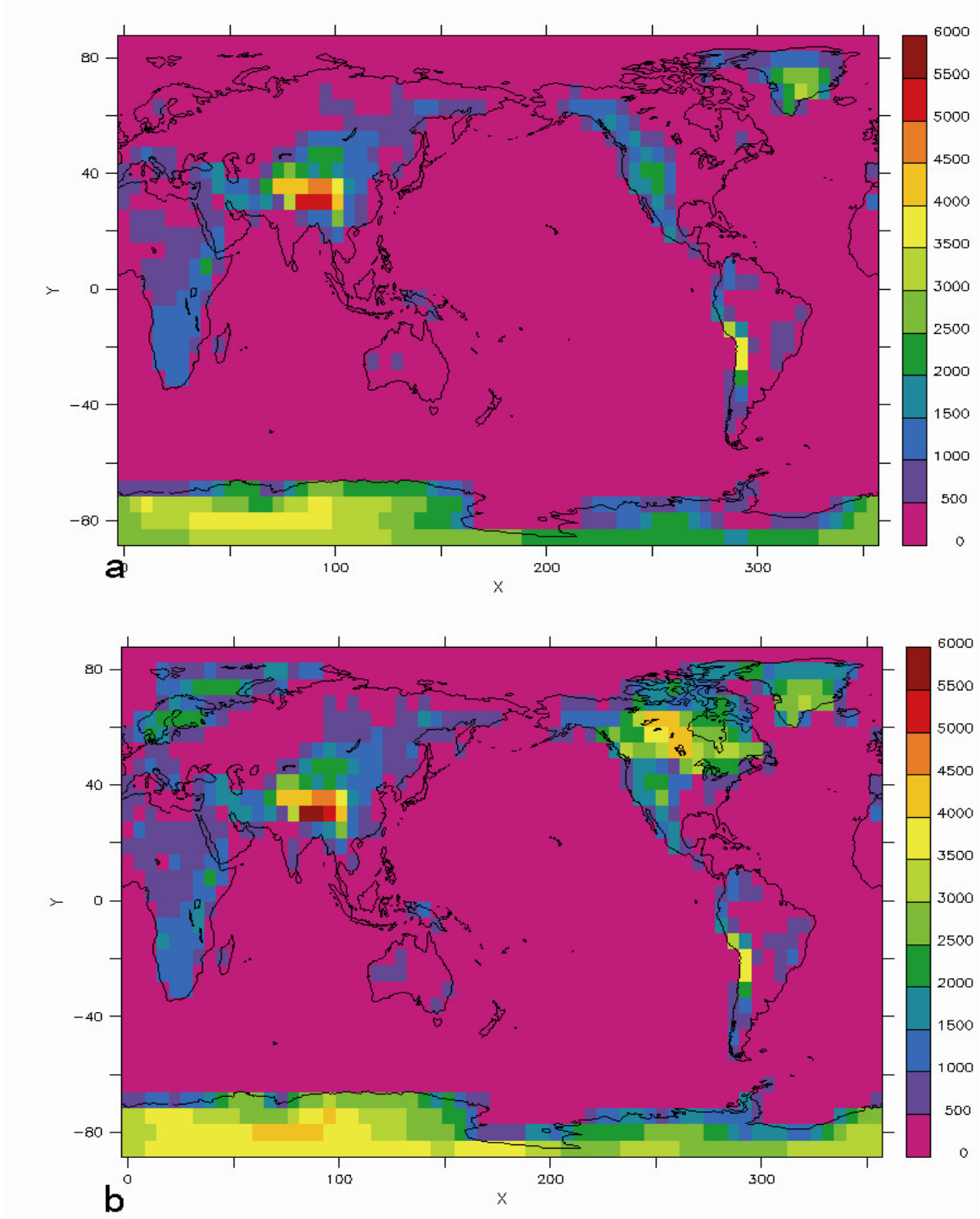

Figure 9. The global land surface topography a) at PI; b) at LGM.

Table 2. Comparison of orbital parameters and atmospheric CO_2 concentration at LGM and pre-industrial.

	LGM	pre-industrial
ECC	0.018994	0.016724
OBL	22.949	23.446
PRE	294.42	282.04
CO_2	200	289

The third experiment (ICE) aims to simulate the climate at intermediate glacial stage. In order to do so, I use a set of hybrid boundary conditions, that is, the LGM surface albedo but pre-industrial orbital parameters, GHG concentration and topography.

All three simulations have been integrated for more than 10,000 model years. The simulated climates are discussed in the next section.

I.3.2 Simulation Results and Abrupt Climate Changes

The simulated time series of annual air temperature from the three experiments, averaged over the North Atlantic region, are illustrated in Figure 10. The simulated climate in the PI experiment reaches equilibrium after a 2000 model year spin-up period. The overall mean air temperature at 2 meters above the surface is about 4.5°C and the standard deviation rarely exceeds 1°C. The simulated LGM climate in the North Atlantic also becomes quasi-stationary after the initial transition. The equilibrated mean air temperature reaches -4°C with a 1°C standard deviation.

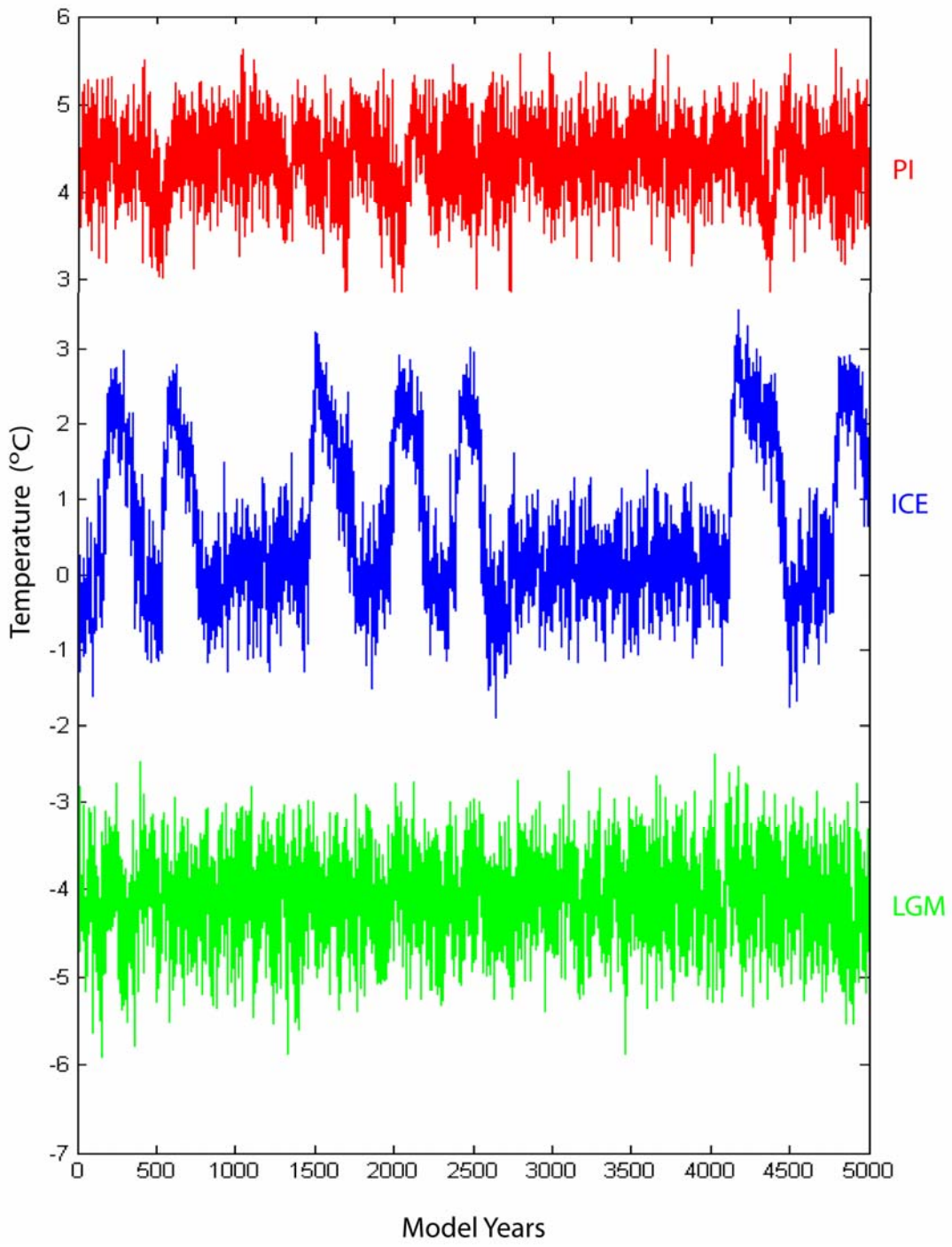

Figure 10. The air temperature at 2 meters above the surface, averaged over the northern North Atlantic region (60°W-40°E, 45°-80°N), in the PI, ICE and LGM simulations. Compared to PI and LGM, the simulated ICE climate is oscillating between cold and warm intervals.

The intermediate ice age (ICE) experiment results show significant differences compared to the previous two. The air temperature in the North Atlantic exhibits large amplitude millennial scale oscillations with abrupt back and forth switching between cold and warm regimes (Figure 10). The cold regimes have mean surface air temperature around -0.5°C Throughout the 5000 year integration the ice age cold regime is interrupted by episodes of warm climate, which initiate as a rapid warming, followed by slow cooling lasting 200 to 500 years, and ending up in rapid cooling. These variations create saw-tooth shaped, pulse-like events, much like the DO oscillations. In contrast, neither the LGM nor the PI results display large scale millennial scale oscillations. This is consistent with the actual GRIP records from the last glacial maximum and from the Holocene.

Figure 11 illustrates the global distribution of the air temperature anomaly between the warm and cold periods in the ICE simulation. The maximum warming spot is located north of the Scandinavian Peninsula in the Nordic Seas. The warming in that area is more than 10°C and occurs within a few decades. There is a secondary warming area near the Labrador Sea. The fact that both warming spots are close to the modeled deep oceanic convection sites suggests that these abrupt climate events are associated with a sudden change of the THC in the North Atlantic. This is illustrated by the overturning stream function contour maps in the Atlantic Ocean (Figure 12), which shows that during the cold periods (weak THC mode), the THC reaches only the mid-latitude Atlantic Ocean, and the NADW formation only takes place in the Labrador Sea. In contrast, during the warm periods (strong THC mode) the THC reaches north of 65°N in the Nordic Seas. This phenomenon is also illustrated by the changing convective layer

depth between these two modes in North Atlantic (Figure 13), which reveals that the deepest convective layer moves northward from the weak mode to the strong mode.

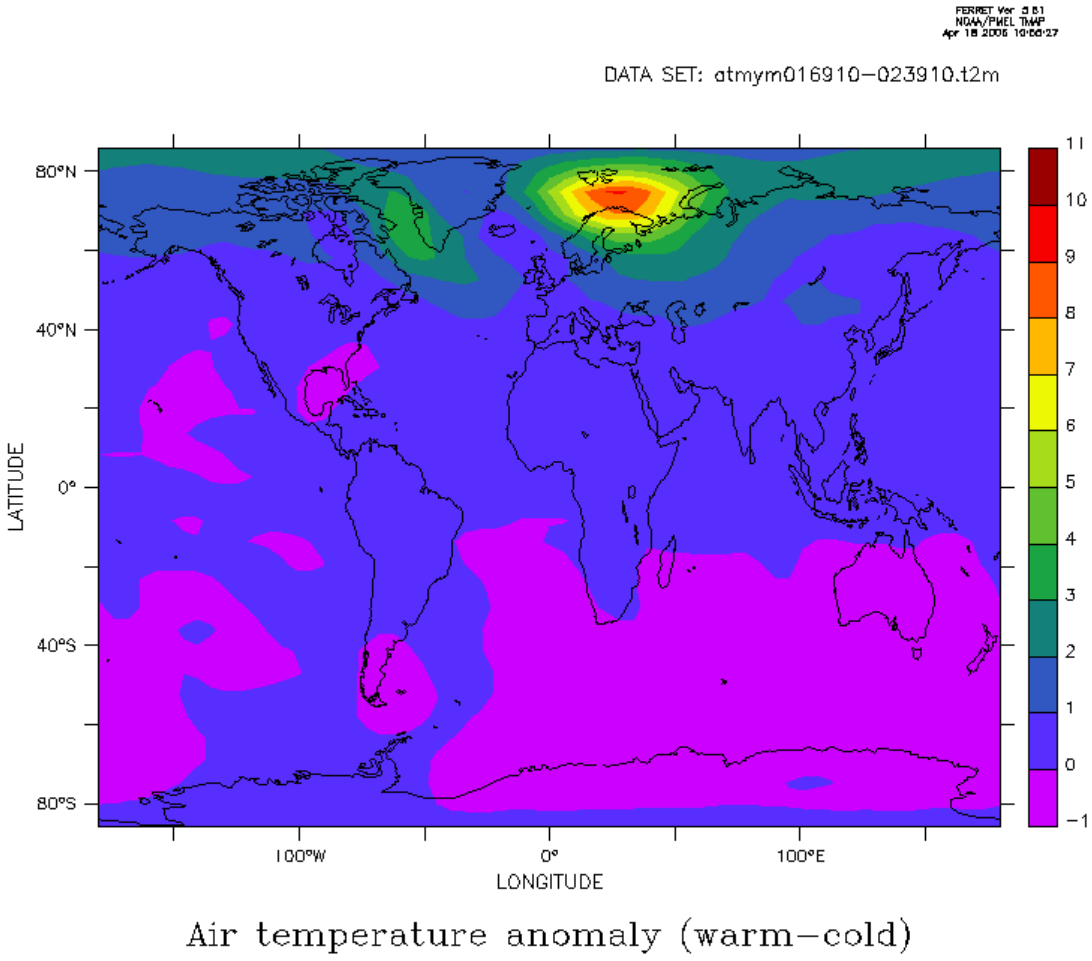

Figure 11. The global distribution of the anomalous air temperature between the warm and cold modes at 2 meters above the surface in the ICE simulation.

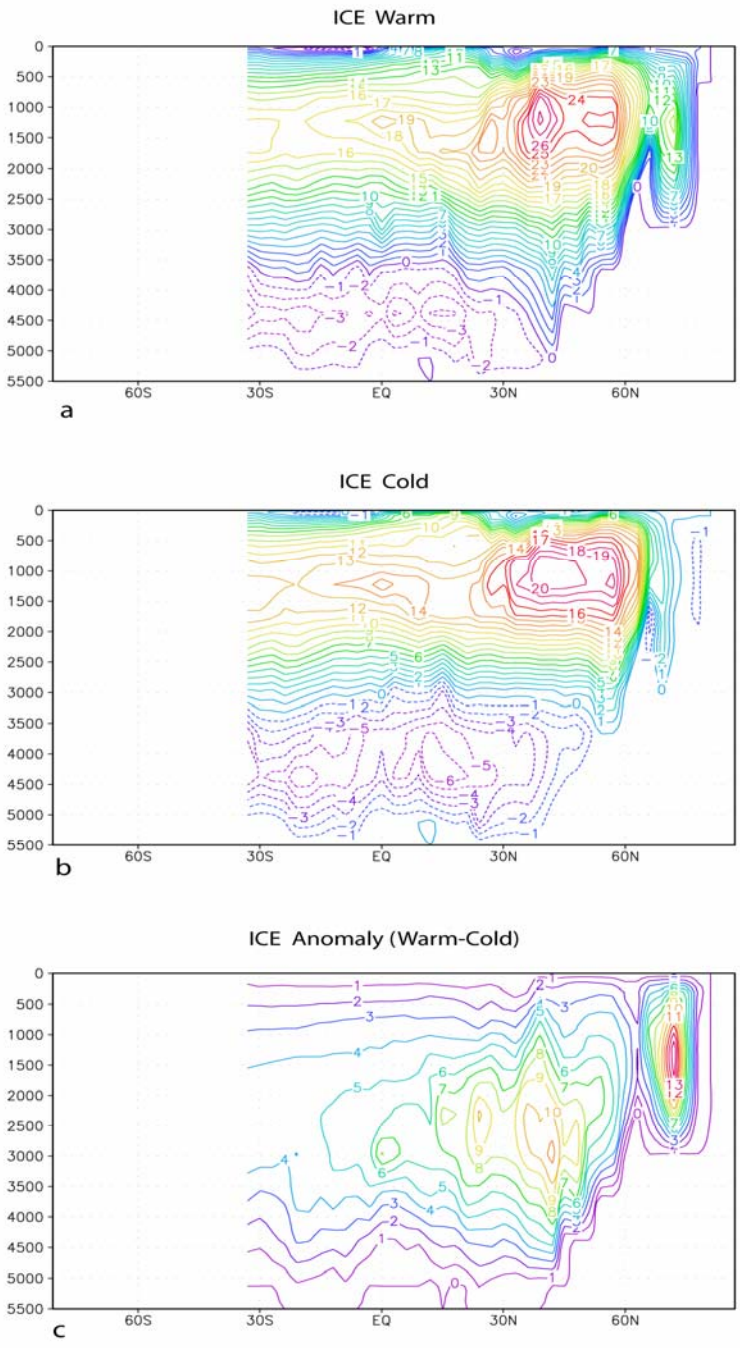

Figure 12. The overturning stream function contours in the Atlantic Ocean. a) during the warm mode; b) during the cold mode; and c) the anomalous stream function between these two modes. The absence of the sinking cell north of 65°N during the weak mode indicates that deep water formation stops in the Nordic Seas at that time. (1 Sv = 10^6 m^3/s).

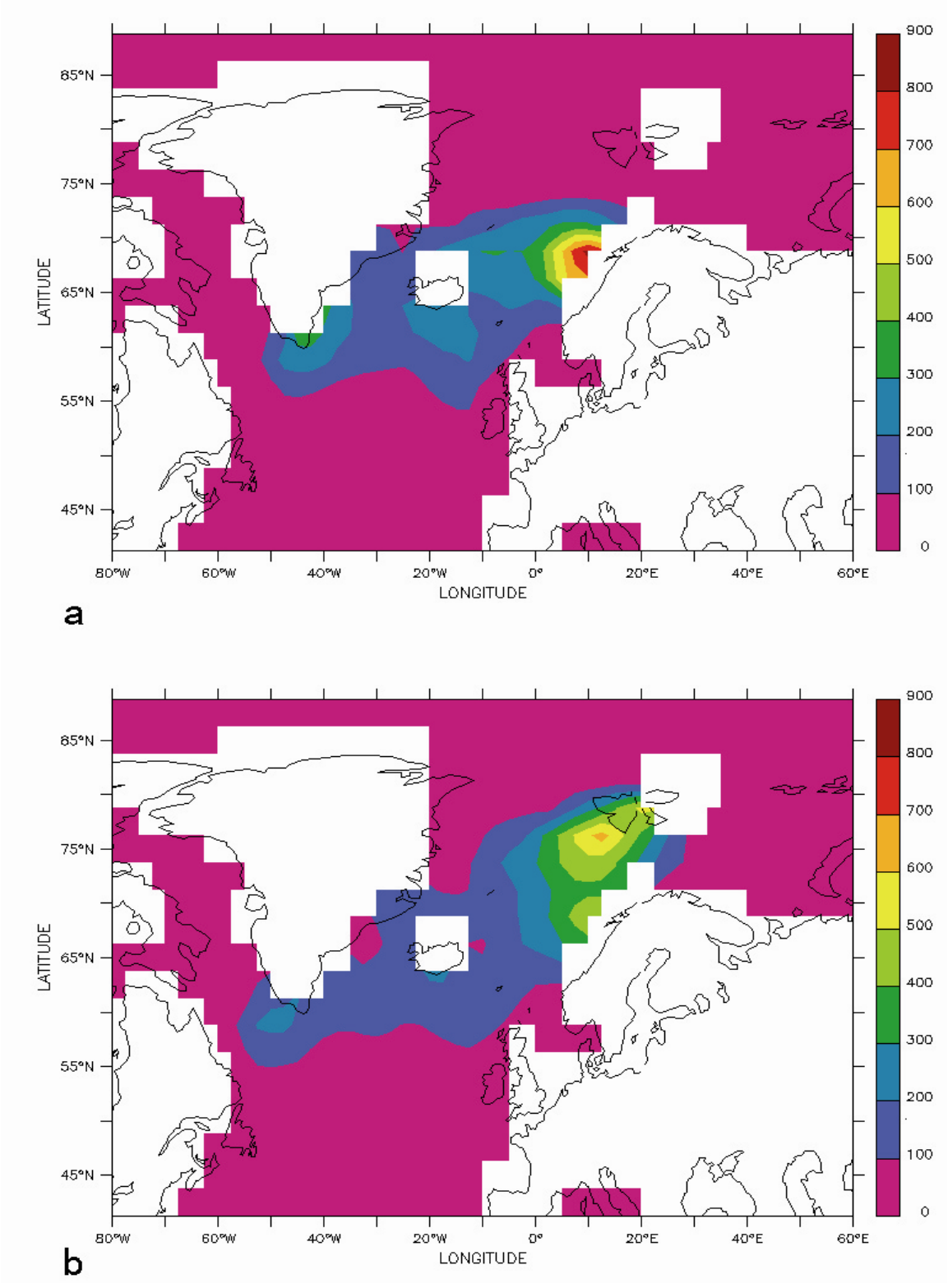

Figure 13. The thickness (meters) of convective layer in the northern North Atlantic a) during the cold mode; b) during the warm mode.

For completeness' sake Figure 14 shows the evolution of various variables related to the THC, and how simultaneous abrupt changes happen in all of them. Consistent with what we saw in Figure 12, the maximum of the overturning stream function (the most frequently used measure of the strength of the THC) in the Nordic Seas (ADGIN) fluctuates between "on" and "off" states.

The enhanced THC in the Atlantic during the strong mode implies more northward meridional heat transport by the Atlantic. For example, at 30°S the transported heat increases from 0.25 PW (1 PW = 10^{15} Watt) to 0.45 PW (illustrated by variable Fc30A in Figure 14). As a consequence, the Southern Hemisphere experiences cold climate during the warm periods in the North Atlantic, and vice versa (Figure 15), resulting in what appears to be a bipolar thermal see-saw.

Figure 14 also shows that the variation of sea ice extent in the Northern Hemisphere (AIEFN) is anti-correlated with the strength of the THC. The sea ice thickness maps in the warm and cold modes (Figure 16) indicate that the most significant changes in sea ice coverage happen in the Nordic Seas, which is almost sea ice free during the warm period. Besides the variables shown before, abrupt changes also take place in other parts of the climate system, including the wind stress pattern, evaporation, precipitation and surface pressure.

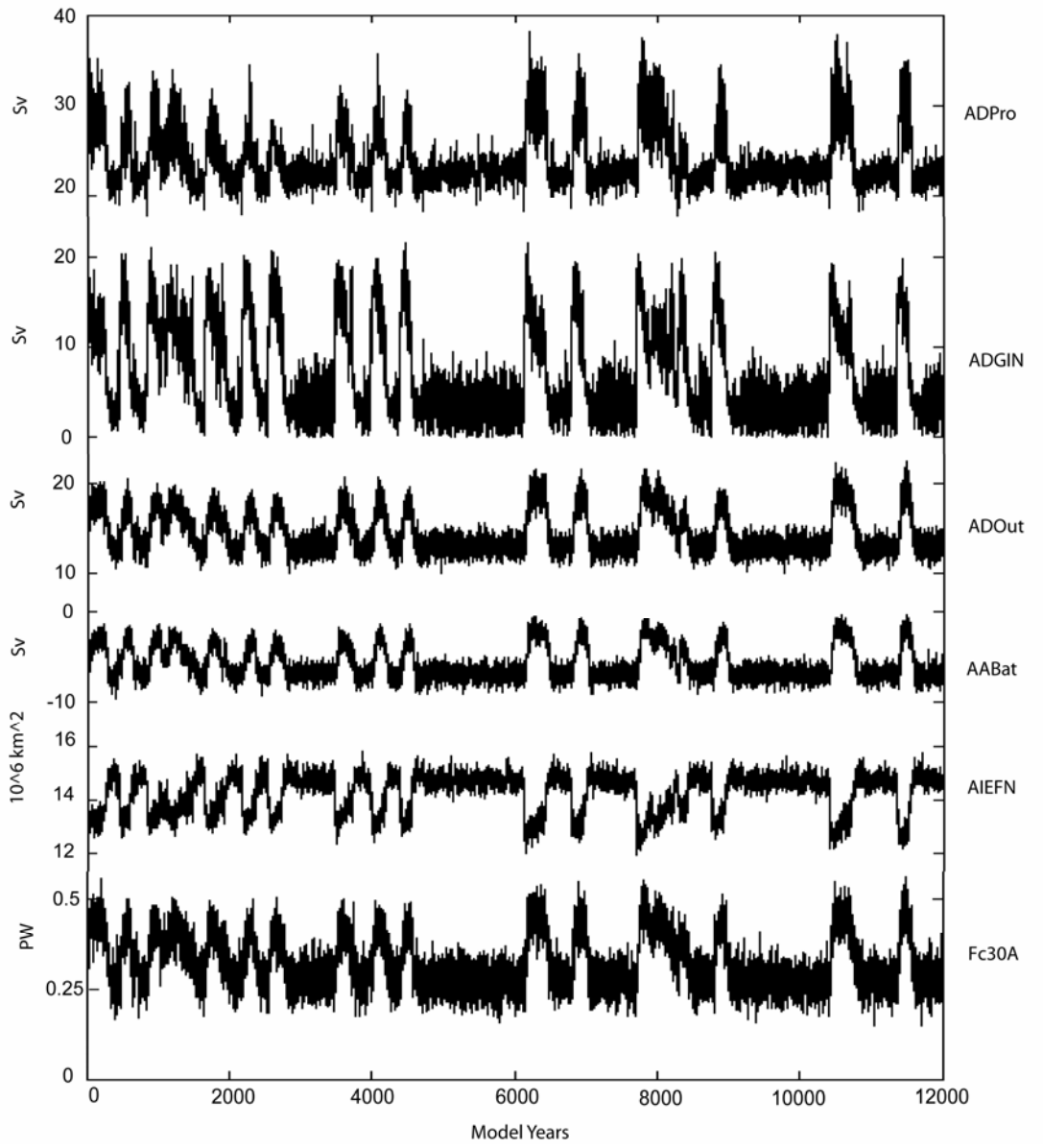

Figure 14. The quantities characterizing the strength of the THC: ADPro (maximum overturn stream function in the North Atlantic), ADGIN (maximum overturn stream function in the Nordic Seas), ADOut (NADW exported southward in the Atlantic at 20°S), AABat (Antarctic bottom water exported northward in the Atlantic at 20°S), AIEFN (sea ice extent in the North Hemisphere), Fc30A (meridional heat flux in the ocean at 30°S)

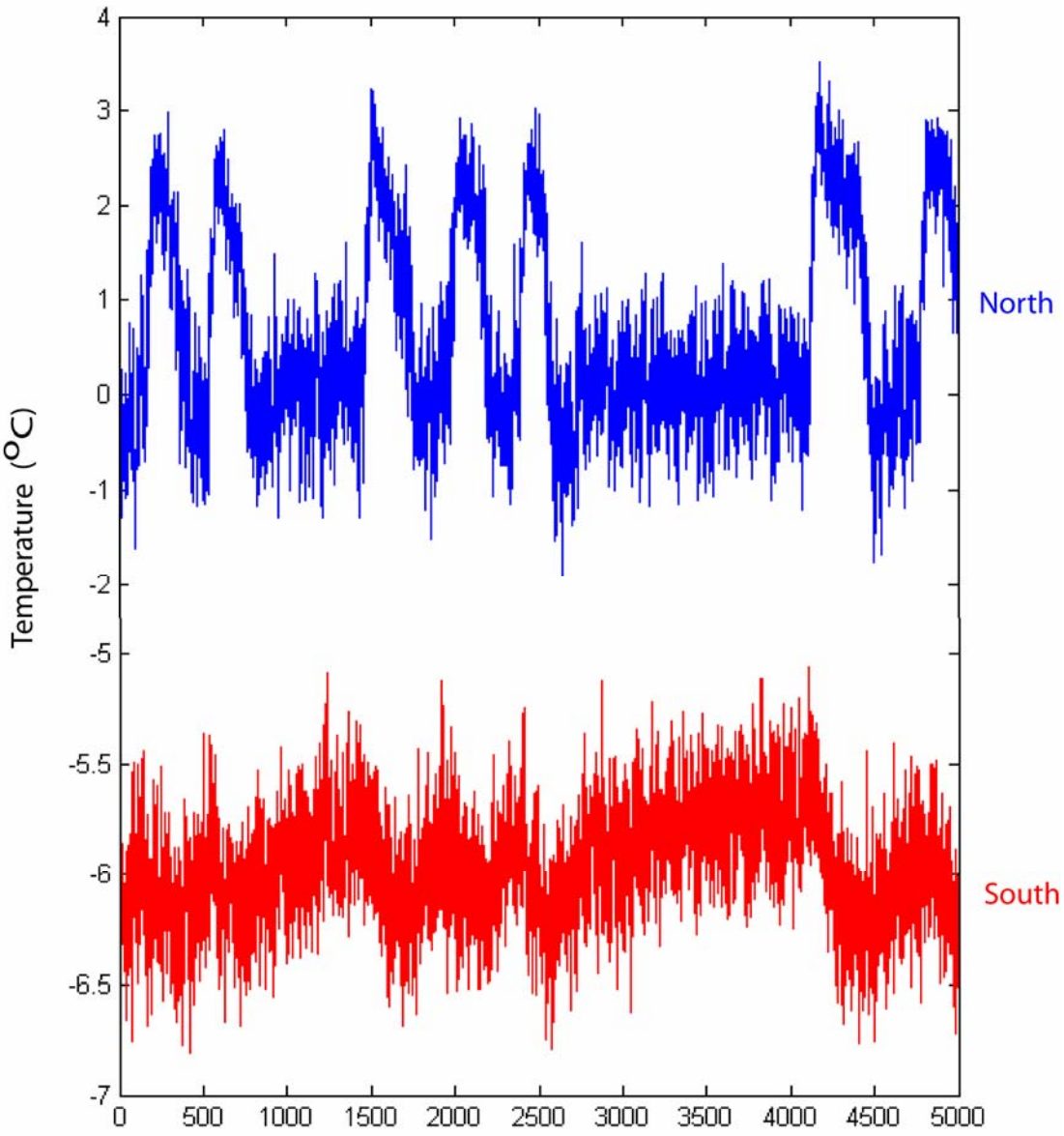

Figure 15. The air temperature in the North Atlantic (60°W-40°E, 45°-80°N) and in the South Hemisphere (0°-360°, 45°-90°S) in the ICE simulation. Bipolar thermal see-saw is evident, that is, when North Atlantic experiences warm climate, the temperature in Antarctica decreases, and vice versa.

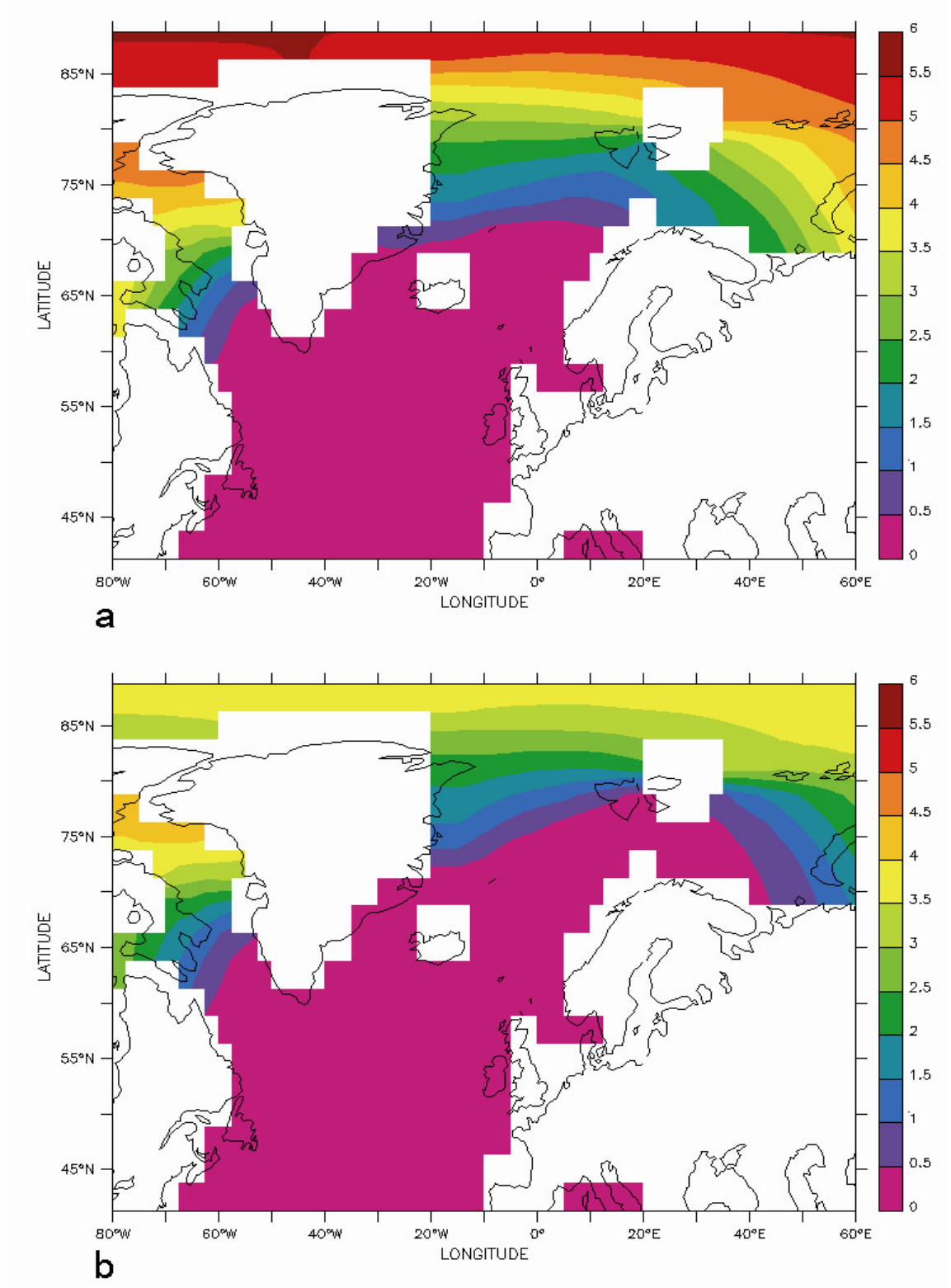

Figure 16. The thickness (meters) of sea ice in northern North Atlantic a) during the cold mode; b) during the warm mode.

I.3.3 The Thermohaline Circulation

As opposed to wind-driven currents and tides, the THC is that part of the ocean circulation which is driven by fluxes of heat and freshwater across the sea surface and subsequent interior mixing of heat and salt – hence the name thermo-haline. Since the THC transports and redistributes a large amount of heat globally, it plays a very important role in the global climate. Furthermore, its nonlinear and potentially abrupt response to external forcing has been invoked to explain abrupt climate changes (Rahmstorf, 2006).

Important features of the THC include deep water formation, spreading of deep waters partly through deep boundary currents, upwelling and near surface currents. Together these lead to a large-scale deep overturning motion of the oceans. Here we follow the description from Rahmstorf (2006).

- Deep water formation: the sinking of water masses, closely associated with convection, which is a vertical mixing process. Deep water formation takes place only in a few areas where the density of surface sea water reaches its maximum.
- Spreading of deep waters: the deep water masses from the North Atlantic and the Antarctic travel mainly as deep western boundary currents.
- Upwelling of deep waters: this is not as localized as convection and is difficult to observe. It is thought to take place mainly in the Antarctic Circumpolar Current region, possibly aided by the wind.
- Near-surface currents: these play a role in closing the circulation loop. In the Atlantic, the surface currents compensating the outflow of NADW

range from the Benguela Current off South Africa, the Gulf Stream, and the North Atlantic Current, as it reaches into the Nordic Seas off Scandinavia.

Figure 17 show a schematic of the pathways of the global THC (sometimes called the " the ocean conveyor").

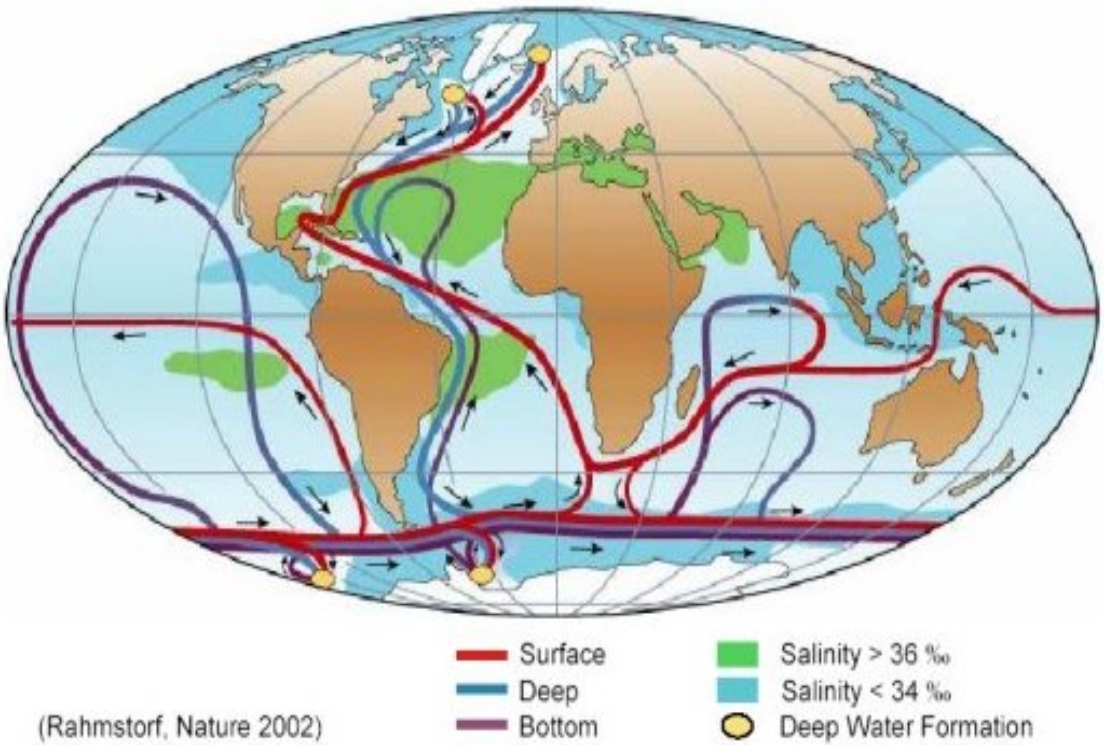

Figure 17 A highly simplified cartoon of the global THC (Rahmstorf, 2002).

At present, hydrographic section data estimate that the volume transport of the THC at 24°N in the Atlantic is 17 Sv (1 Sv = 10^6 m^3/s) (Roemmich and Wunsch, 1985). Its associated heat transport is about 1.2 PW. More recently, Ganachaud and Wunsch

(2000) used an inverse model to yield 15 ± 2 Sv of NADW overturning in the high latitudes, while Talley et al. (2003) estimated the strength of the NADW formation to be 18 ± 5 Sv. Less information is available about the deep water formation region in the Southern Ocean around Antarctica. Tracer data suggest another ~15 Sv of deep water sinking there, bringing the global total to over 30 Sv (Rahmstorf, 2006).

I.3.4 An Explanation: the Free THC Oscillations

It is generally believed that the oceanic THC is driven by high latitude surface cooling, as the intense heat loss to the atmosphere causes ocean surface water to reach its highest densities at some places in the high latitudes. This cold dense water then sinks into the deep ocean, flows, spreads out along the ocean bottom, and finally returns to the surface by uniform upwelling through the interior ocean (Wunsch, 2000). Were this the only driving force the ocean basins would eventually be filled with cold dense water, the sinking of surface water would stop, and the circulation would come to a halt. Many authors (e.g., Sandstrom, 1908; Wunsch, 2002; Rahmstorf, 2006) point out that vertical turbulent mixing also plays an essential role in maintaining the THC, mainly by transporting heat downwards and warming the deep ocean, lowering deep water density, and keeping surface water in the high latitudes denser than the water in the deep ocean. Therefore, a steady-state of the THC can be established if and only if the classic advection-diffusion balance is achieved: at any given point in the deep ocean, the advection of cold water from the poles is equal to the diffusion of heat by turbulent mixing (Rahmstorf, 2006). This is the case for the present-day THC.

Since deep water formation is caused by convection (a highly nonlinear, threshold-dependent process), while vertical mixing is linear, it is quite possible that under appropriate boundary conditions the warming due to vertical turbulent mixing and the cooling caused by deep water formation never exactly balance each other, in which case an oscillation in the strength of the THC might develop. This oscillation may or may not be periodic, and could possibly be chaotic, since ultimately it is the result of nonlinear processes. Further, as no varying external forcings (e.g., time-varying perturbations on the fresh water balance, time-varying insolation forcing) have been used, the oscillations simulated in the ICE experiment (Figures 10, 14) must be self-sustained, induced by the internal dynamics of the climate system.

This speculation is supported by the ICE experiment. In Figure 18, results of the ICE simulation (Figure 18a) are used to construct a diagram of stages (Figure 18b) that describes how the THC free oscillation may work. Beginning at stage 1, the THC is off in the Nordic Seas and the sea surface there is cold and is covered by sea ice. However, the deep ocean is still warmed by turbulent mixing, which increases the deep ocean temperature and lowers the water density. Such decreases of water density in the deep ocean tend to weaken the stability of the oceanic layering. Eventually, at stage 2, a threshold is crossed. The water column becomes top-heavy unstable, triggering a rapid flush of deep water formation in that area by convection, and the convection transports massive amounts of cold surface water to the deep ocean. As a result, at stage 3, the deep ocean starts to cool. While on the surface, THC brings warm and salty water to the high latitudes, resulting in surface warming and maintaining the deep water formation. As the temperature of the deep ocean keeps decreasing, eventually another threshold is crossed,

as the stable stratification of ocean layers is restored. The process goes to stage 4; the THC in the Nordic Seas is shut off; the sea surface temperature drops and sea ice rapidly advances by positive feedback. Slowly, the deep water begins to warm by mixing again; the loop goes back to stage 1. Another cycle begins. In this way a free oscillation of the THC can be sustained.

Figure 19 illustrates the time series of deep ocean temperature and water density in the deep ocean in Nordic Seas from the ICE simulation. The time evolution of the water density is highly anti-correlated with that of the water temperature, demonstrating that the density variation is thermally driven and salinity only plays a minor role in the deep ocean, consistent with the hypothesized process discussed before.

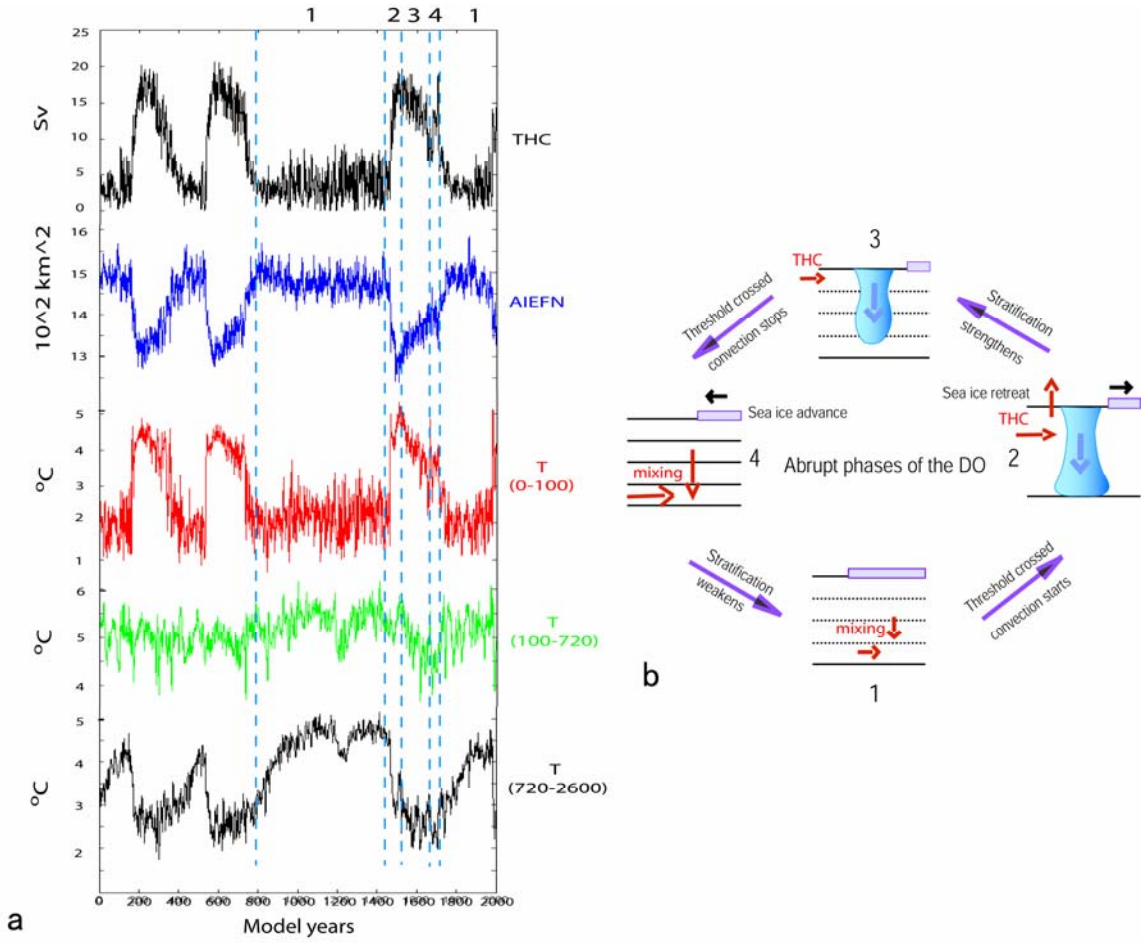

Figure 18. (a) A cross-section through the water column in the maximum warming spot in the temperature anomaly map (Figure 11). It illustrates the relationship between the THC, sea ice extent (AIEFN), and the oceanic temperature at various depths. (Water depth intervals through which the variables have been averaged are given in parenthesis). (b) A schematic diagram of the proposed stages of the THC's free oscillation. The number 1-4 here correspond to those in (a). Red arrows indicate direction of heat flux; longer arrows meaning stronger heat flux.

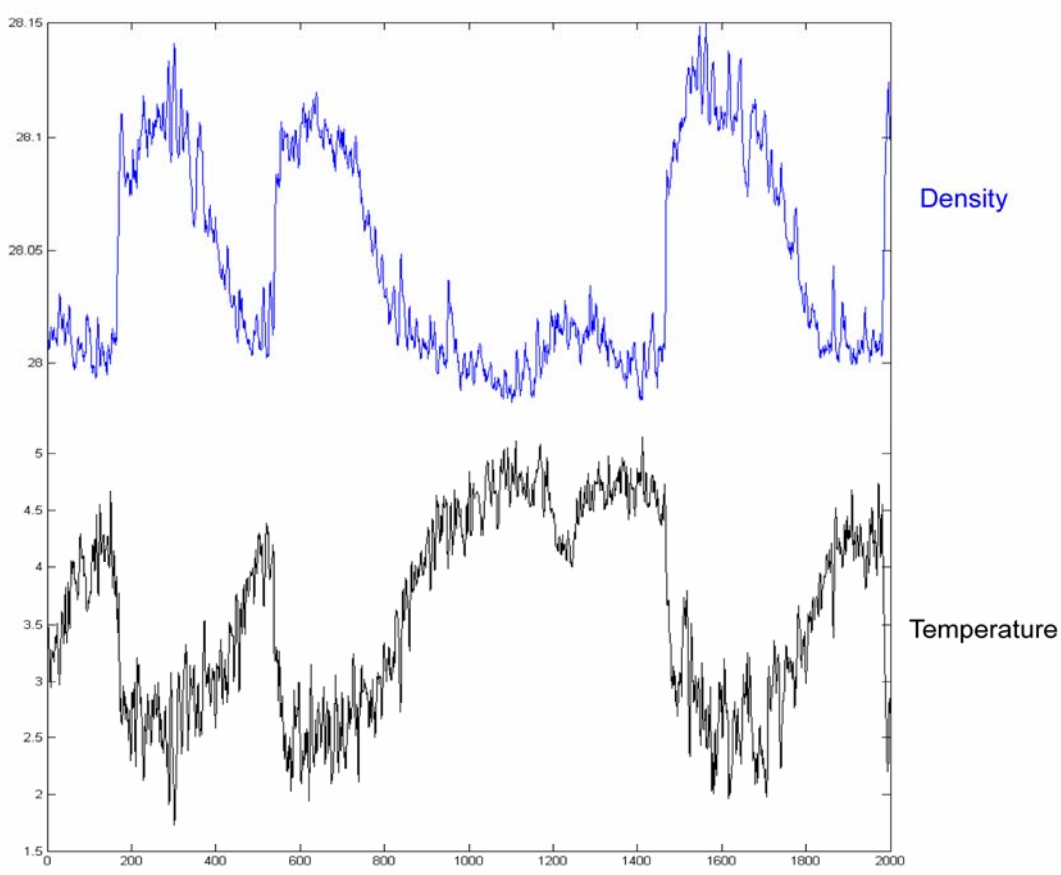

Figure 19. Time variations of water density and temperature in the deep ocean in the Nordic Seas from the ICE simulation.

I.3.5 Absence of the Free THC Oscillations during LGM and PI

Another question one might ask is why the free THC oscillations disappear under the LGM or PI conditions. In order to answer this question, we simplified the process described by the stage diagram in Figure 18a, as illustrated by Figure 20a. Here we are assuming the convection is a highly nonlinear process. Whether it is "on" or "off" depends only on two critical temperatures in the deep ocean, which determine the stability of ocean layers in the high latitudes. T_{low} is the threshold temperature when the deep ocean is cold enough so that the sinking of surface water stops while T_{high} is the

other threshold temperature when water in the deep ocean is warm enough so that the ocean layer becomes top-heavy unstable. We also assume turbulent mixing is a linear process, the heat diffused by mixing decreases with increasing deep ocean temperature.

Similarly to the process described before, at stage 1 when the THC is off in the Nordic Seas, the heat gain by mixing is larger than the heat loss by convection, so that the deep ocean starts to gain heat and the temperature keeps increasing. As soon as the temperature reaches T_{high}, convection is triggered; this is stage 2. From now on the heat loss due to deep water formation overwhelms heat gain by mixing so that the deep ocean starts to cool, this is stage 3. The temperature of the deep ocean will keep decreasing until it reaches the other threshold T_{low}. Now the water in the deep ocean is dense enough to prevent the sinking of cold surface water. The deep water formation in the Nordic Seas is turned off. This is stage 4. The deep ocean starts to accumulate heat by mixing again. The process goes back to stage 1. It continues as a loop.

But during the pre-industrial period, the surface ocean is much warmer, which means at the same temperature in the deep ocean, more heat is diffused by mixing, so that heat gain by mixing and heat loss by convection are able to balance each other between the two threshold temperatures (Figure 21b). Under the LGM conditions, since surface water is colder and denser, the threshold temperature T_{low} should be lower. As a result, an equilibrium temperature between mixing and convection is also achieved between T_{low} and T_{high} (Figure 21c). In both conditions, the THC will reach a steady-state with advection of cold water (or convection) and diffusion of heat balancing each other. This is why the THC free oscillation is not observed in these two simulations.

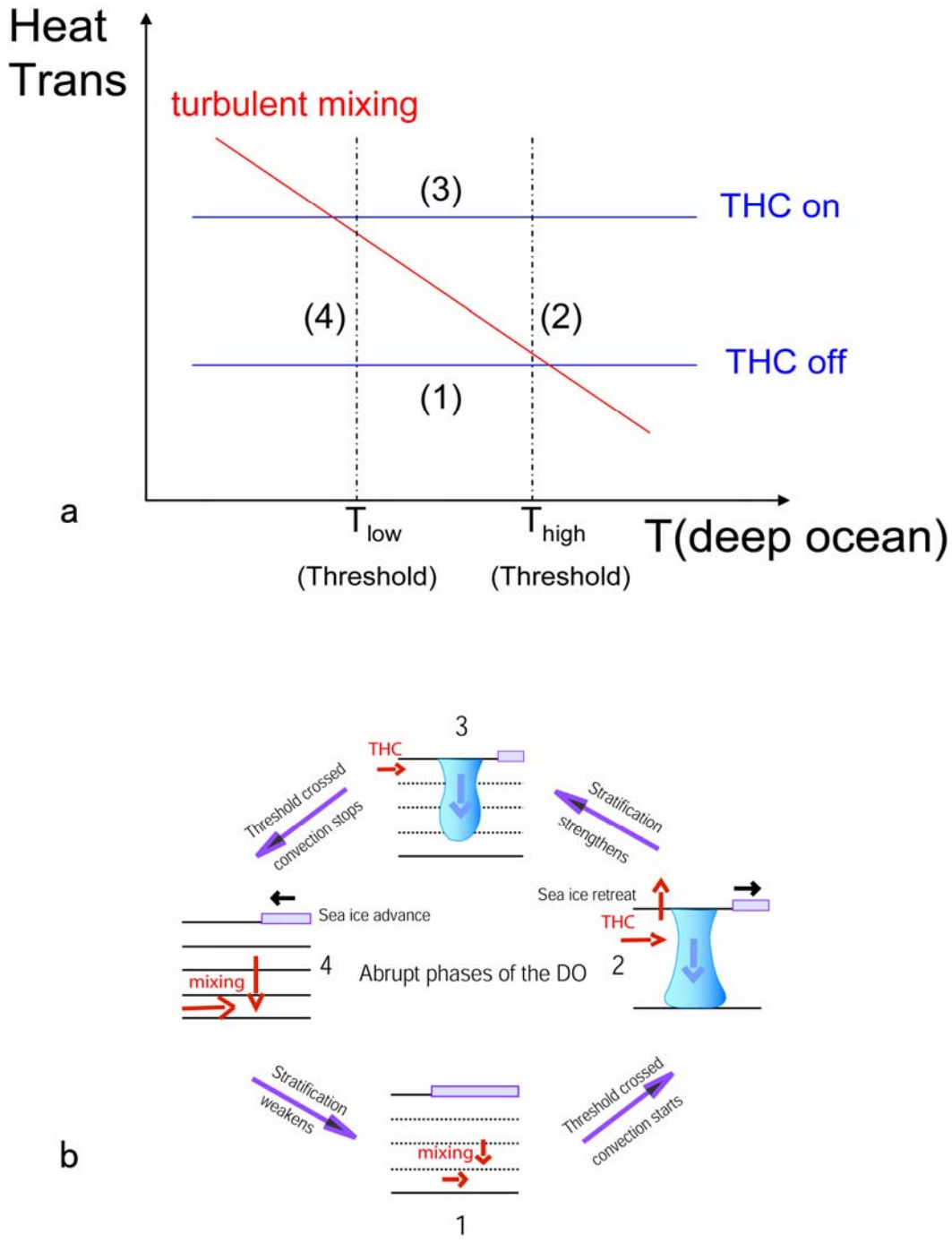

Figure 20. (a) Another way to illuminate the process described by Figure 18a. The x-axis is the temperature of the deep ocean, and the y-axis is the heat transport by convection, the blue lines, or by mixing, the red line. (b) The same as Figure 18a.

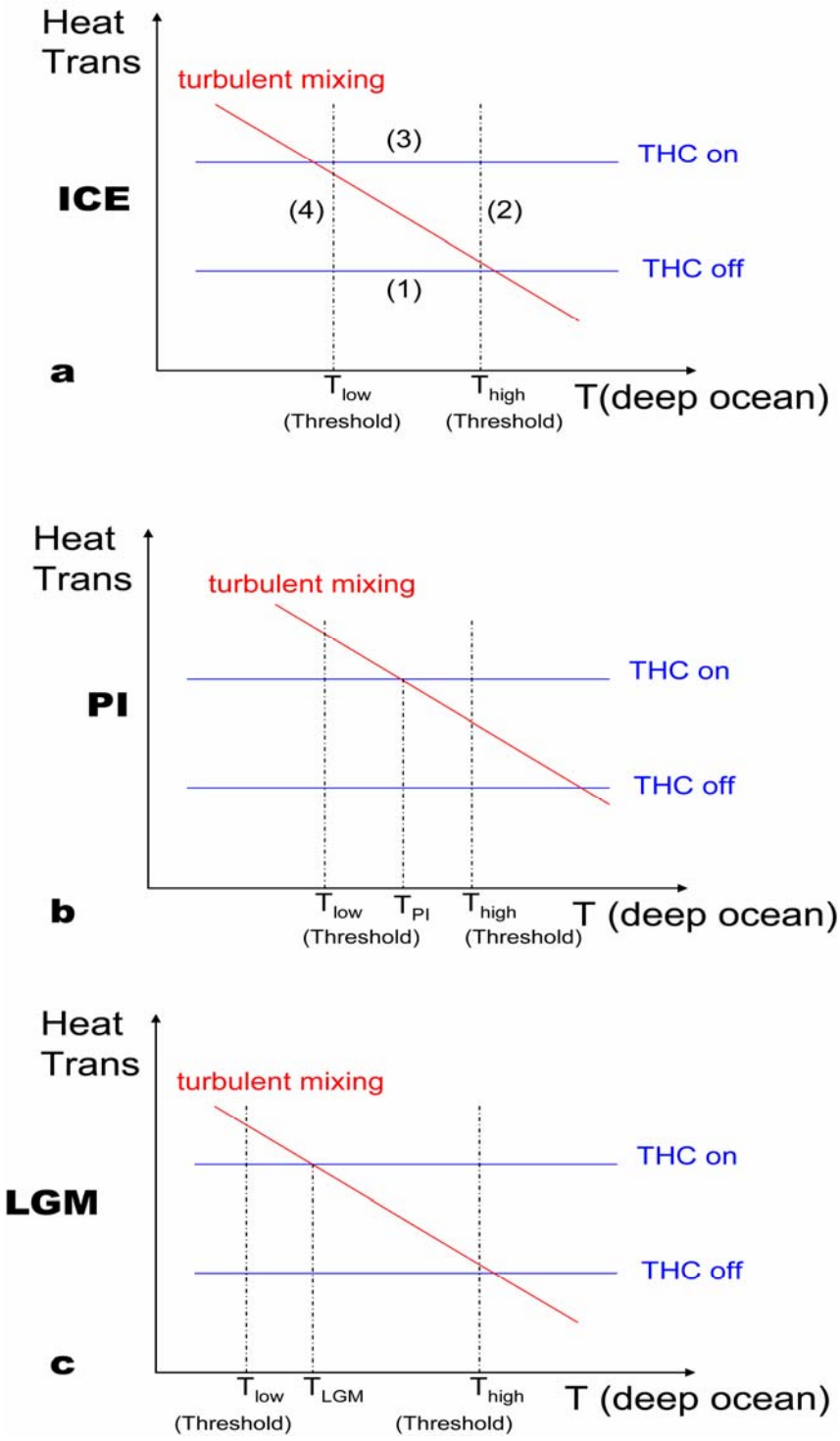

Figure 21. (a) The same as Figure 20a. (b) The balance between convection and turbulent mixing during pre-industrial. (c) The balance between convection and turbulent mixing during Last Glacial Maximum.

I.3.6 The Fast Response of Sea Ice

The role of sea ice in the whole process is very important, and thus deserves a separate discussion. Sea ice mediates the exchange of radiation, sensible heat and momentum between the atmosphere and the ocean (Kaspi et al., 2004; Wang and Misak, 2006). It also acts as an effective ocean insulator, whose removal releases ocean heat, and potentially triggers highly energetic GHG feedbacks that further contribute to warm the atmosphere and accelerate sea ice retreat. Conversely, sea ice advance, induced by a THC slow down, quickly stops heat and gas exchanges between the ocean and the atmosphere, allowing the full glacial climate to return. Sea ice thus plays a partial role in accelerating the warming (or the cooling) of the atmosphere. This is consistent with Figure 16, which show that the maximum warming spot in the Nordic Seas is normally covered by sea ice all year long during the cold regime, and that as the deep water starts to form, the upward heat flux from the ocean increases, sea ice melts away and triggers an ice-albedo feedback that swiftly causes large areas of the ocean to become ice free. The uncovered ocean in turn releases heat and water vapor (and other greenhouse gases) into the atmosphere, triggering more positive feedbacks that will further amplify the magnitude and abruptness of the warming. ECBilt results show that the surface air temperature jumps from cold to warm regimes (and vice versa) in as short a time as two years. I speculate (ECBilt does not have a carbon cycle) that greenhouse gases, carbon dioxide and especially methane, will help intensify the magnitude and therefore the duration of the warming event. A warm open ocean will readily release CO_2, intensifying water vapor feedbacks, and from the surrounding land, ice free tundra will readily release methane as the surface temperature increases.

I.3.7 The DO Oscillations Following the THC

Our experiments show that the variability of the THC and associated abrupt climate changes are present under the intermediate ice age boundary conditions, while the THC is stable (no millennial oscillations) under both LGM and PI (pre-industrial) conditions. This result is in line with the fact that in the real world the abrupt climate changes, the DO events, are most prominent when temperatures in the ice age are relatively mild and suppressed during the cold LGM and the warm interglacial (McManus et al., 1999). As illustrated before, the main characteristics of the DO oscillations—the three-phase time evolution of the air temperature that forms the distinctive saw-tooth shape of the DO events (Rahmstorf, 2002), the spatial pattern of anomalous temperature (Figure 11) and the bipolar thermal seesaw (Blunier and Brook, 2001)—are intrinsically associated with the free oscillation of the THC. Indeed, the changes of oceanic circulation pattern in the ICE simulation are in good agreement with the proxy data and other model simulations of the DO events. Recent geochemical data (Veum et al., 1992) suggest that the THC must have switched between different modes with different sites of deep convection during the last ice age. Ganopolski and Rahmstorf (2001) use an improved version of the CLIMBER-2 model to show that the DO events are caused by latitude shifts of convection between the Nordic Seas and the mid-latitude open Atlantic Ocean. These studies are qualitatively consistent with our results as well. As shown before (Figure 12 and variable ADGIN in Figure 14), during the weak mode of the Atlantic THC, the deep convection occurs dominantly in the Labrador Sea; in contrast, during the strong mode, the deep water formation sites move northward with surface water sinking not only in the Labrador Sea but also in the Nordic Seas.

In summary, the resemblance between the observed DO events and the simulated millennial scale climate changes enable us to speculate that DO events might have been caused, at least partially, by the same mechanism that drives the oscillations in the model.

Furthermore, evidence was found from Nd isotope ratios (a proxy of the balance between North Atlantic Deep Water (NADW) formation and southern-source waters) that suggests that there is increased strength in the NAWD during the Bølling warming, a decline during the Allerød cooling and an increase again at the YD termination (Piotrowski et al., 2005), fully consistent with the THC model proposed before. Moreover, and as shown in Figure 22, this close correlation is not limited to the BA-YD events but occurs over the entire length of the last ice age, with the THC strength in close synchrony with the DO pulses and the warming of sea surface temperature (SST). An obvious question is why such independent proxies would show strong correlation over a sequence of seemingly random events. One possible answer, of course, is that a random process drives all three, which would make predictability impossible. An alternative we favor is that the same deterministic forcing drives all three, and the randomness of the events is only apparent. Our modeling results in fact suggest that the reason that the proxies show such similar (yet apparently random) timing is because all three are entrained by Milankovitch forcing, as shown next.

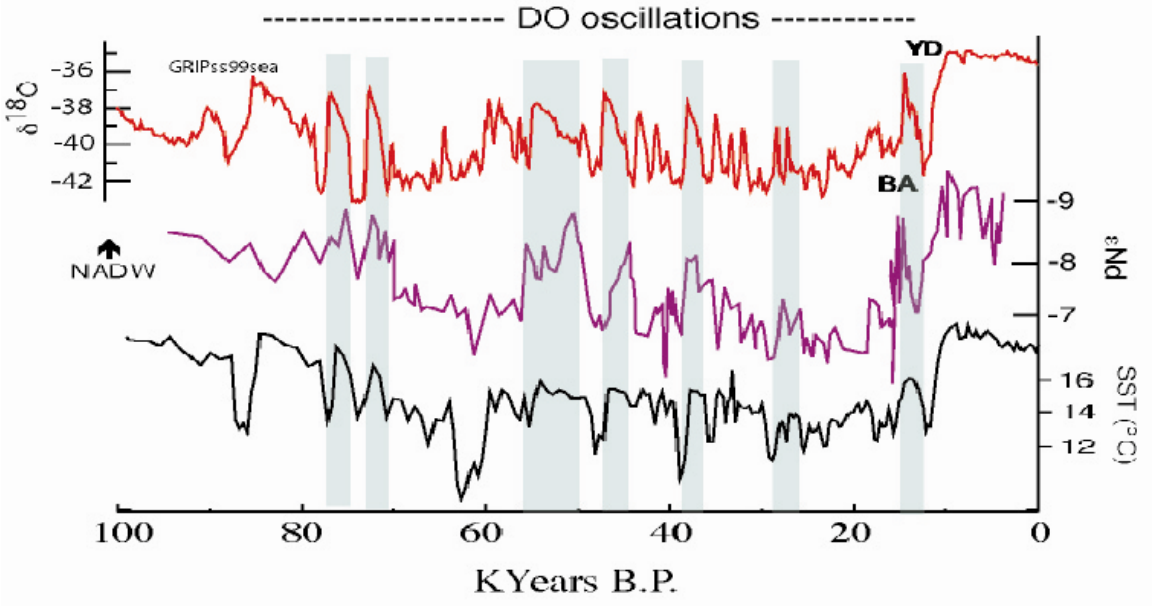

Figure 22. The Dansgaard-Oeschger (DO) oscillations as recorded by oxygen isotope ratios in the GRIP record (top), compared to Nd isotope ratio, a proxy for the balance between North Atlantic Deep Water (NADW) formation and southern-sourced waters in the South Atlantic (Piotrowski et al, 2005), and a North Atlantic sea surface temperature (SST) record (Bard, 2003). In almost all occasions times of strong NAWD production correlate with GRIP interstadials and warm ocean surface. The chronology is based on the GRIPss99sea age model. BA and YD mark the Bølling Allerød and the Younger Dryas events respectively.

I.4 Orbital Modulation and the Timing of the DO Oscillations

I.4.1 Milankovitch Cycles

The Milankovitch cycles refer to the cyclical changes in the Earth's orbit around the Sun. They are characterized by variations of three Earth's orbital parameters, i.e., eccentricity, obliquity (axial tilt), and precession. The Milankovitch cycles change the seasonal and latitudinal distribution of solar insolation reaching Earth's surface in the time scale of more than 10,000 years. These periodic alterations in solar radiation directly influence the global climate system and account for the glacial/interglacial cycles for the last 1000,000 years.

Eccentricity describes the shape of the Earth's orbit around the Sun. It is a measure of the departure of this ellipse from circularity. The Earth's orbital shape fluctuates between more and less elliptical (approximately eccentricity ranges between 0 and 0.05) on a periodicity of about 100,000 years (Figure 23a). The eccentricity cycle changes the amount of radiation received at the Earth's surface in the whole year and is directly related to the glacial/interglacial cycles.

Obliquity is the tilt of Earth's rotation axis with respect to the plane of orbit around the Sun. Variations of Earth's axial tilt is roughly periodic, with a periodicity of about 41,000 years (Figure 23b). The Obliquity mainly accounts for the seasonal difference in the global climate. At present, obliquity is in the middle of its range of 23.5^{o}.

The third Milankovitch cycle is Earth's precession cycle. Precession is the change in the direction of the Earth's axis of rotation relative to the Sun at the time of perihelion

and aphelion in a periodicity of 23,000 years (Figure 23c). At present, the Earth is at perihelion very close to the winter solstice.

Figure 24 shows the variation of these three orbital parameters in the past glacial/interglacial cycles and the resulting solar insolation received in June at 65°N (Berger and Loutre 1991). In the next section, I will demonstrate that the variations of solar insolation due to the Milankovitch cycles play a crucial role in the timing of the DO oscillations.

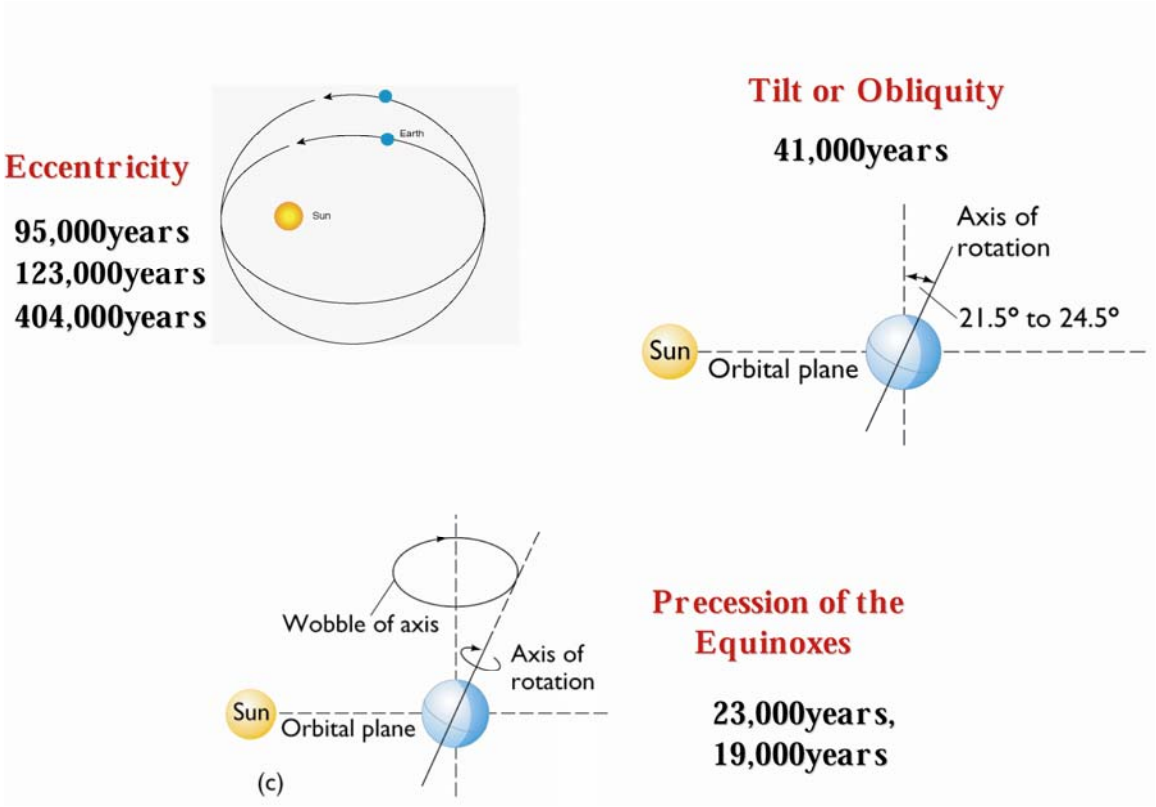

Figure 23. The cartoons illustrate the variation of orbital parameter a) eccentricity; b) obliquity; and c) precession.

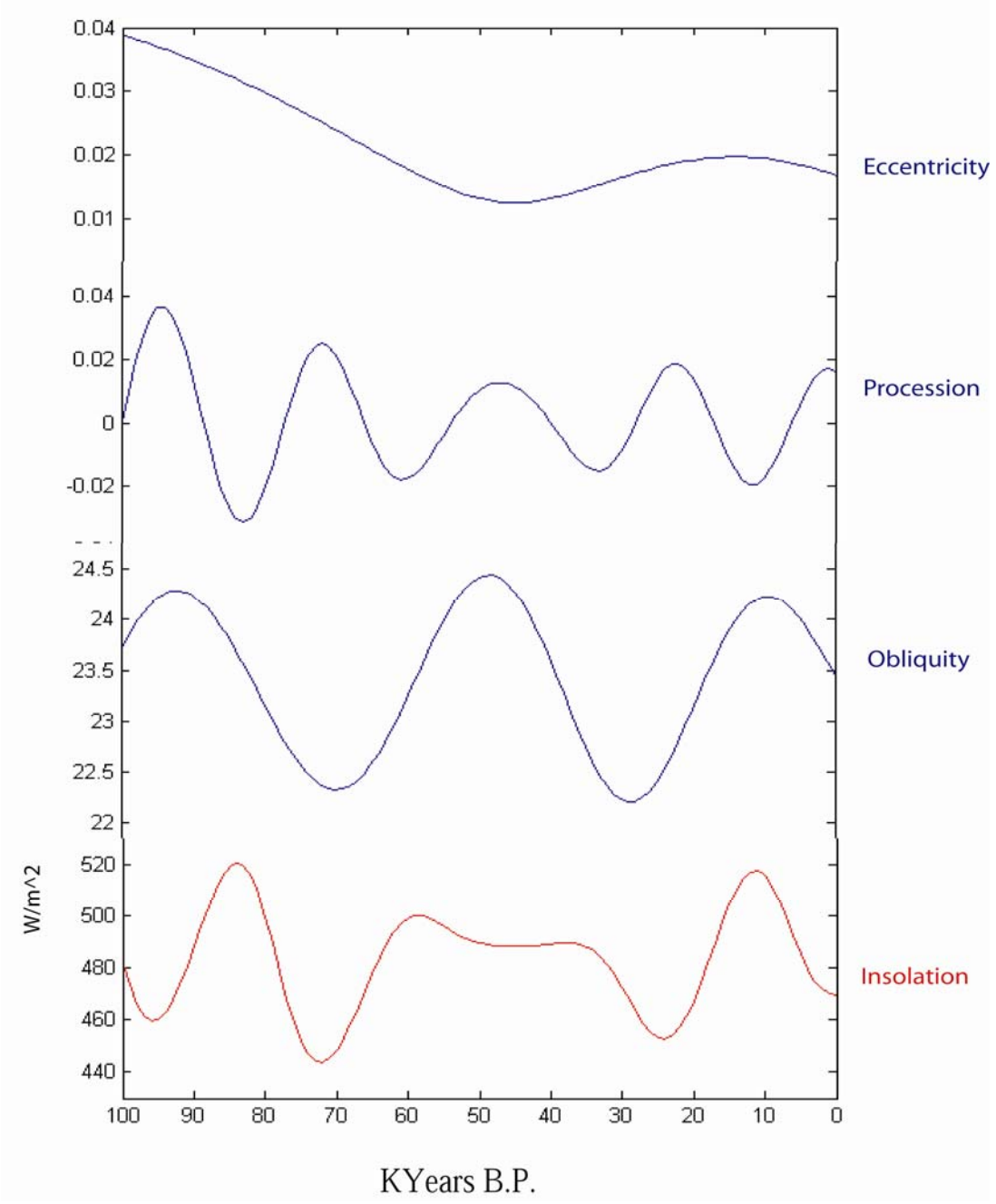

Figure 24. Calculated evolution of orbital parameters (eccentricity, precession and obliquity) and the resulted solar insolation received in June at 65°N during the last 100,000 years (Berger and Loutre, 1991)

I.4.2 Frequency Modulation

The frequency modulation (FM) is similar to the electronic modulation of a high-frequency carrier by a low-frequency modulating signal, as used in radio and television broadcasting. The FM is a nonlinear phase- and frequency-locking process that transfers energy from one frequency band into another, and can create new frequencies as combination tones of the carrier and the modulating frequencies (Rial, 1999; Rial and Anaclerio, 2000). An FM signal may be expressed as

$$x(t) = \sin[\omega_0 t + \varphi_0 + \beta \sin(\omega_m t + \varphi_m)] \tag{I.4.1}$$

where ω_0 is the carrier frequency and $\varphi_0 + \beta \sin(2\pi\omega_m t + \varphi_m)$ is the modulating phase. Hence, we may decompose the instantaneous phase as the carrier and modulating phase. Figure 25 illustrate the time series of a FM signal and its power spectrum.

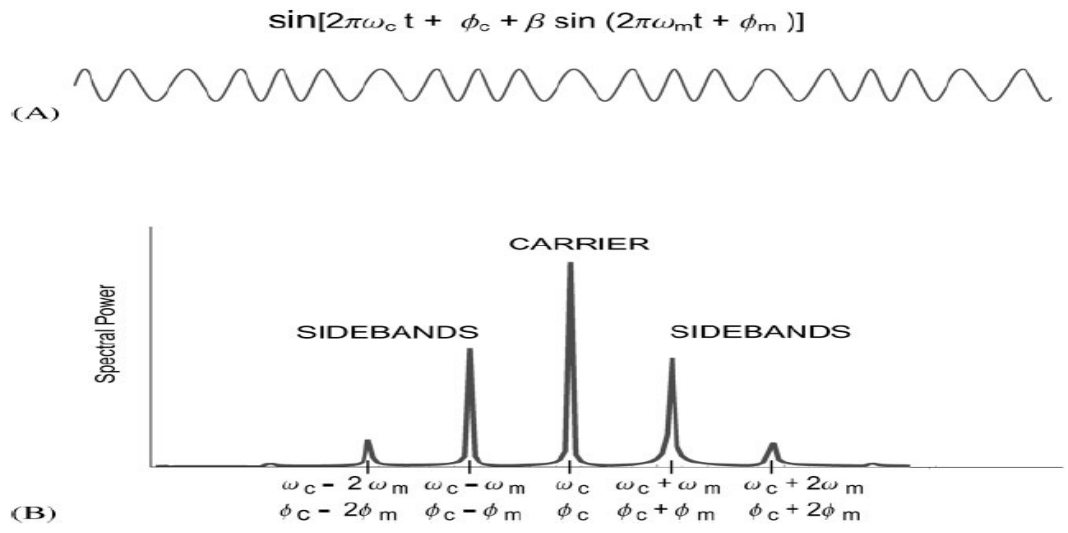

Figure 25. General analytic form of a frequency-modulated signal (A) and its power spectrum (B). ω_c is the carrier frequency and ω_m is the modulating frequency. ϕ_c and ϕ_m are the phases of the carrier and modulator, respectively (Rial and Anaclerio, 2000).

I.4.3 Orbital modulation

In the ICE experiment, the simulated DO-like oscillations are seemingly random, probably aperiodic or chaotic (as shown by Figure 14). This is not surprising given the dynamic complexity of the global ocean. The duration of the warming intervals in our model rarely exceeds 500 years, while the recorded warming intervals of the DO events, especially in the early ice age, can last for several millennia. Though this would appear to be an undesirable feature of our simulation we have to keep in mind that in the ICE experiment we assume fixed orbital parameters, GHG concentrations, surface albedo and topography while in reality these conditions changed substantially and constantly during the last 100ky, as illustrated in Figure 26. Consequently, the mean or average climate progressed from the relatively warm early glacial climate to the coldest last glacial maximum, and then recovered to the present interglacial. During the glacial-interglacial cycles, the mean climate is mainly determined by latitudinal and seasonal distribution of the solar insolation, which evolves with varying orbital parameters between the earth and the sun (the Milankovitch cycles). As Clark et al. (2002) stated, "The stability properties of the THC depend fundamentally on the mean climate state". This argument is supported by our numerical experiments, which show that the THC is unstable (and chaotically oscillating) in the ICE simulation while it is stable (over time scales longer than hundred years) in the PI and LGM simulations.

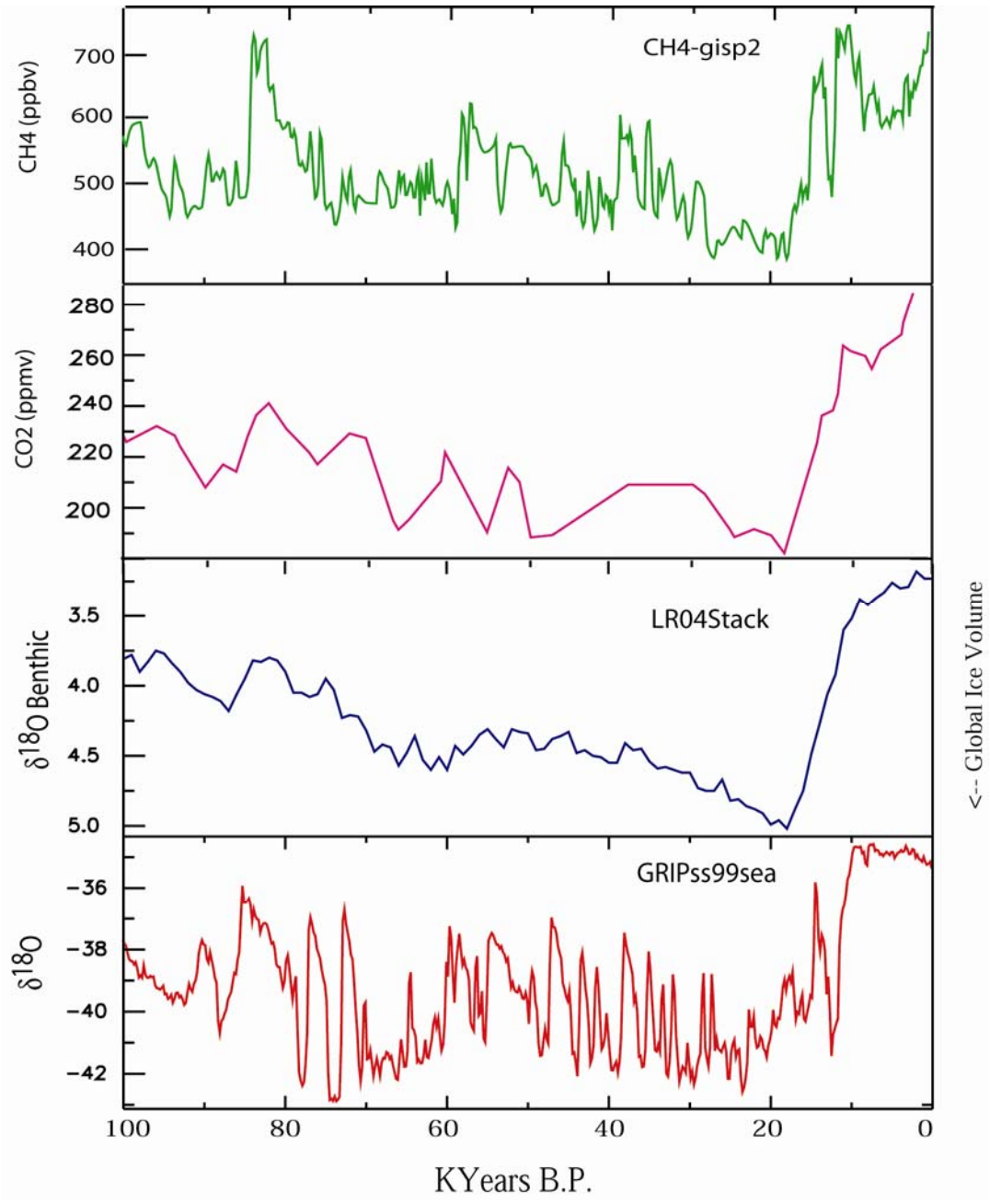

Figure 26. The evolution of climatic variables during the last 100ky: CH_4, CO_2, $\delta^{18}O$ benthic from Raymo et al. (1998) (proxy for the global ice volume) and $\delta^{18}O$ (proxy for the regional air temperature) in the GRIP ice core.

To investigate the variability of the THC under continuously varying boundary conditions, I performed a fourth experiment (ORB) in which the climate is forced by the theoretical solar insolation for the last 100ky (Berger and Loutre 1991, Figure 24). Here one faces a problem of scale, since integrating a 3-D coupled model such as ECBilt-Clio for 100,000 model years requires at least 18 months of continuous CPU time. Hence, in order to attain at least some degree of understanding of the effect of astronomical forcing in a workable amount of time, I opted for simulating the climate variation with a 20ky run (which can be completed in slightly less than four months). For this purpose I used a scaled-down insolation function of identical shape but with frequencies five times higher than the actual. The resulting forced oscillation of air temperature is shown in Figure 27. Keeping in mind that the ECBilt-Clio result is not in the "real" time scale, it is nevertheless clear that the insolation forcing produces an effect on the original signal that ends up looking like the GRIP data (assuming time scale invariance (Rial, 2003)). The implication is that the low-frequency solar forcing frequency modulates the free oscillation, and entrains the otherwise chaotically distributed oscillations. More specifically, in the model the orbitally-induced insolation is a sort of organizing force, through which the durations of warming and cooling events are grouped together or spread apart according to the insolation's amplitude.

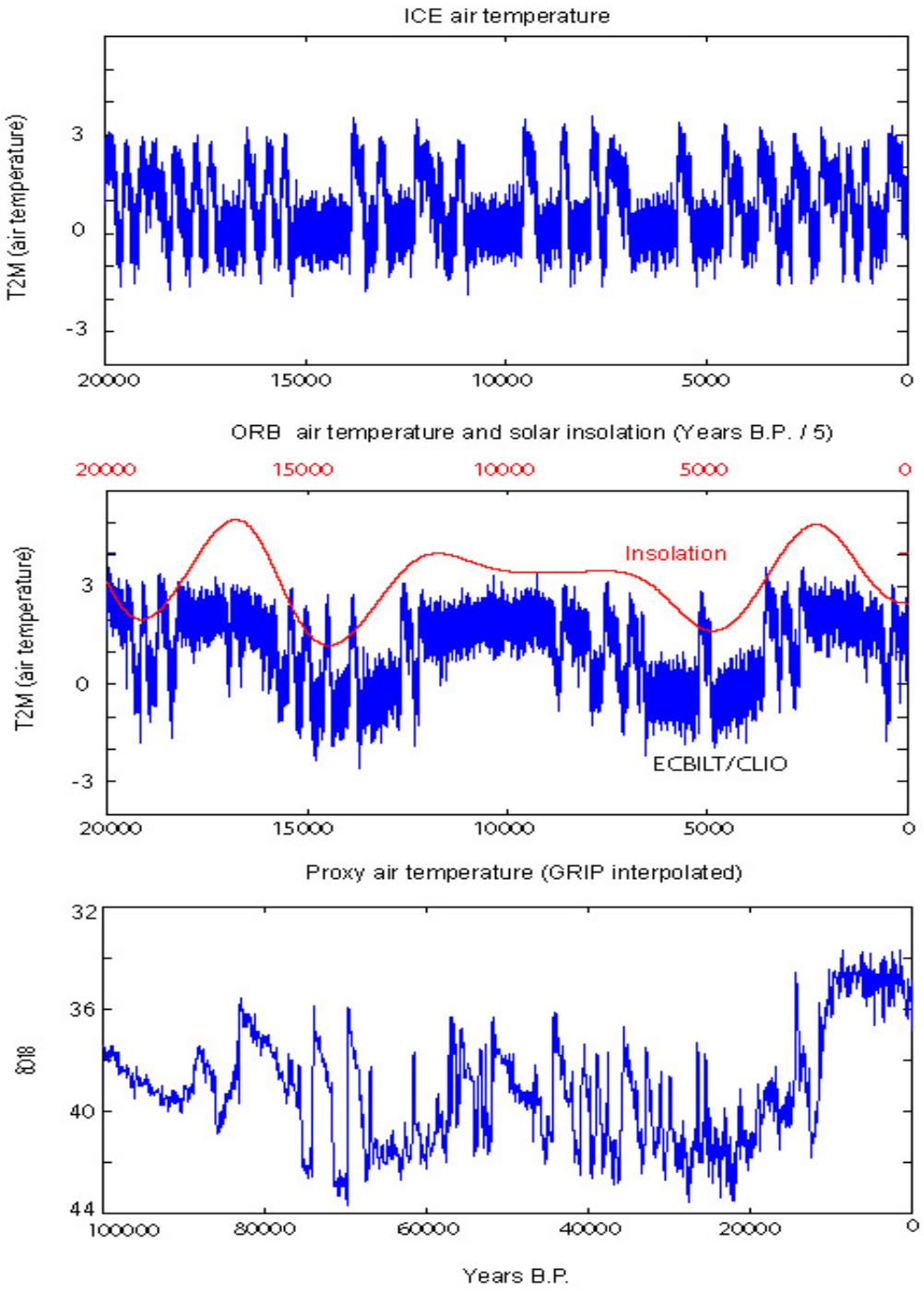

Figure 27. (top) The 20,000 year ICE simulation without varying solar forcing. (middle) A 20,000 year run representing the 100ky last ice age. The free oscillation is forced with the scaled-down insolation. (bottom) The recorded GRIP proxy data for air temperature over the Greenland. Note the change in time scales.

This conclusion is also supported by the results of the SVO model. As discussed before, this model is derived from a system of two nonlinearly coupled first order differential equations that represent the interaction among mean ocean temperature (sustained by a constant supply of heat), sea ice, and greenhouse gases in a glacial atmosphere. Such interaction creates a nonlinear, self-sustained thermal oscillator with millennial-scale periodicity, as described by Saltzman and Moritz (1980). Without the insolation forcing SVO would produce a simple periodic (albeit abrupt) temperature signal. In contrast, when forced by the theoretical solar insolation variation, SVO recreates the GRIP proxy data qualitatively (Figure 28), and not surprisingly, the SVO also produces a signal very similar to the ORB experiment output (Figure 29).

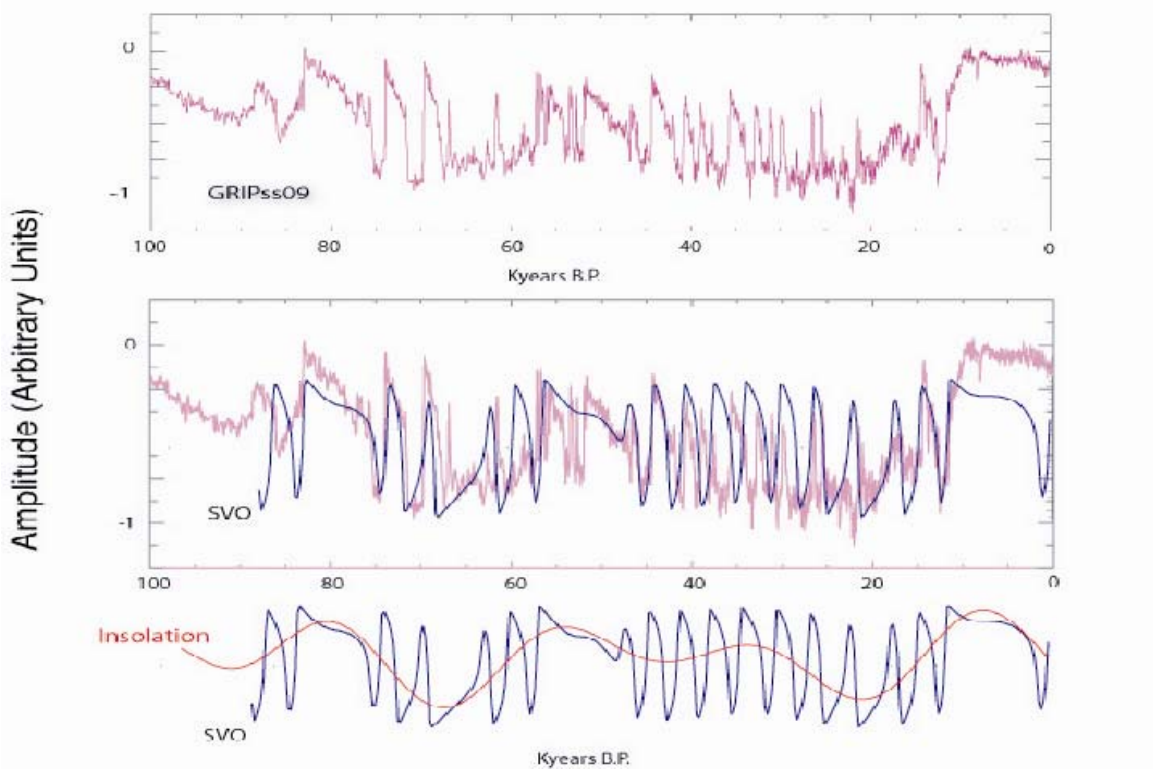

Figure 28. The ice core isotope record from Greenland (GRIP ss09) simulated with SVO; the relaxation oscillator of the van der Pol type forced by the insolation. SVO reproduces the DO oscillations with remarkable fidelity for a model that is just a second order nonlinear differential equation with external forcing. The figure shows that the peculiar distribution of pulse-like warming events in GRIP may be caused by frequency modulation of the thermal oscillator's natural frequency, which in this case is the solution to a homogeneous van der Pol equation. The model predicts a general warming during the Holocene (last 10ky) but with lower amplitude than observed because SVO does not include the melting of the ice sheets and consequent warming leading to the present interglacial. The forcing is the North Hemisphere summer insolation (65°N) function from Berger and Loutre (1991). GRIP data is from GRIP project members (1993).

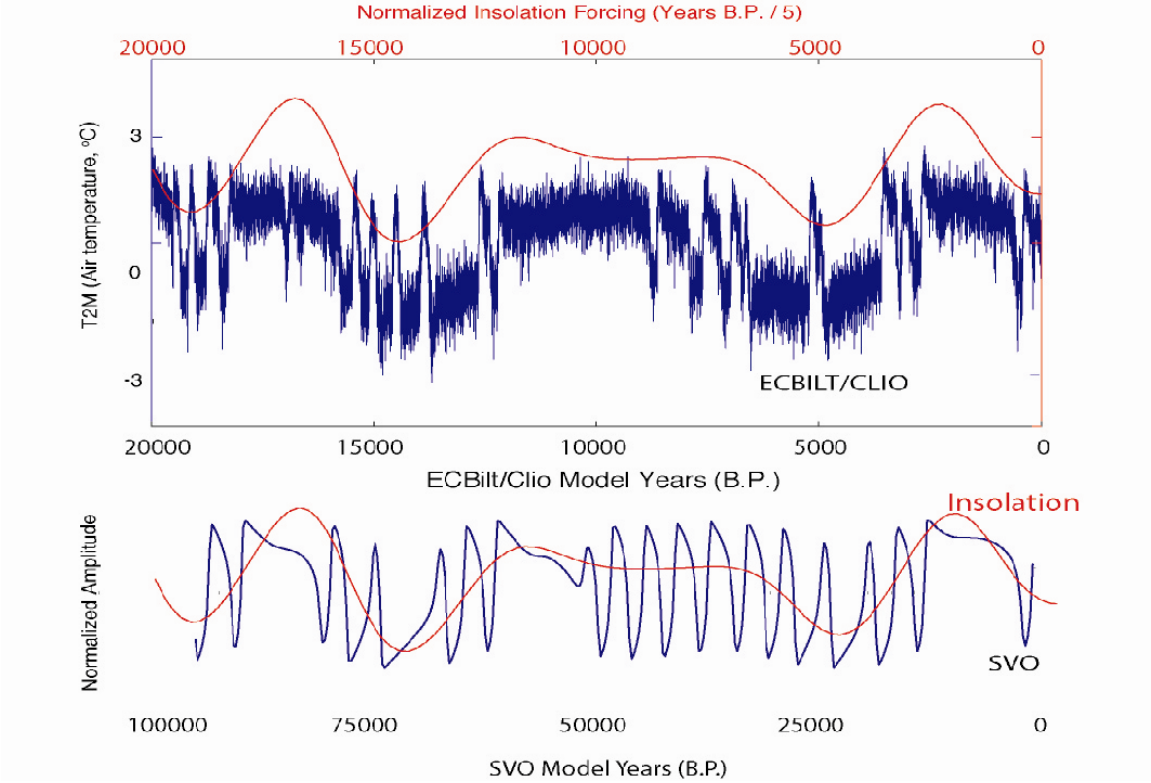

Figure 29. A 20ky run in ECBilt-Clio simulating the 100ky last ice age (assuming time scale invariance). The free oscillation of the THC is forced with the scaled-down insolation. The resulting frequency modulation produces a time series consistent with what the simpler model SVO indicates; i.e., the time distribution of the DO warming pulses is controlled by the Milankovitch insolation.

The physics implied in this hypothesis is easy to understand. Times of high insolation create long intervals of warm temperatures and the added heat increases evaporation and thus surface water salinity, which keeps the THC on and prevents sea ice advance. As a consequence, the duration of individual warming pulses lengthens (warm climate prevents sea ice advance). But in times of low insolation (e.g., around 65ka, 20ka) sea ice is more likely to advance as the THC weakens, resulting in fewer and shorter lived warm intervals and more frequent returns to "normal" glacial conditions (cold climate makes sea ice retreat rare and brief). Thus, the nonlinearity of the climate model

causes the dependence of the oscillation frequency on the insolation, which is distinctly different from a commonly held linear view of astronomical forcing, which considers that insolation paces temperature change proportionally, as if (linear) amplitude modulation were the only effect of insolation on the climate system. This nonlinear process is akin to frequency modulation. In fact, some particularly puzzling characteristics of the much longer period, orbital-scale paleoclimate records have been explained by frequency modulation, whereby the period of some internal oscillation of the climate system is modified in proportion to the varying insolation amplitude (Rial 1999). A mechanistic description of how this can occur in physical systems that respond nonlinearly to external forcing has been explained in detail elsewhere (Rial 2004).

I.4.4 Are Abrupt Climate Changes Predictable?

Using the insolation as external forcing it is possible to speculate whether the models used may provide some advance knowledge of future climate change, at least in the long term. A remarkable fit obtained with SVO of the last 25ky (1ky = 1000 years) is illustrated in Figure 30, a detail of Figure 28. To obtain the fit in Figure 30 we added the temperature increase caused by the melting of the ice sheets, which is not included in the original equations. Besides the fact that SVO thus modified produces a better fit of the GRIP data than that in Figure 28, the result suggests that because the THC oscillation strength is modulated by the insolation, millennial scale abrupt climate change events may in fact be predictable. Note for example how the long warm episode from 11ka to ~5ka corresponds to relatively high insolation, while the strong downward oscillation

starting at ~2ka is a consequence of the rapid decrease in insolation currently underway. The modeled time series in the last 2ky interval is qualitatively consistent with reconstructed long-period cooling trends (e.g., Morberg et al. 2005) and predicts a sharp warming trend for the next century quickly followed by a return to glacial temperatures in about two millennia. Clearly, however, the amplitude of the down swing during the little ice age is far too large compared to the latest reconstructions. Of course, SVO is too incomplete to be a reliable source of prediction, but the simulation with ECBilt-Clio points equally to the insolation, and specifically, to those intervals when it is rapidly changing, as the underlying force that makes DO oscillations emerge from long interglacial periods. I argue that the suggestion of predictability is probably compelling enough to justify testing on more complete climate models than ECBilt-Clio.

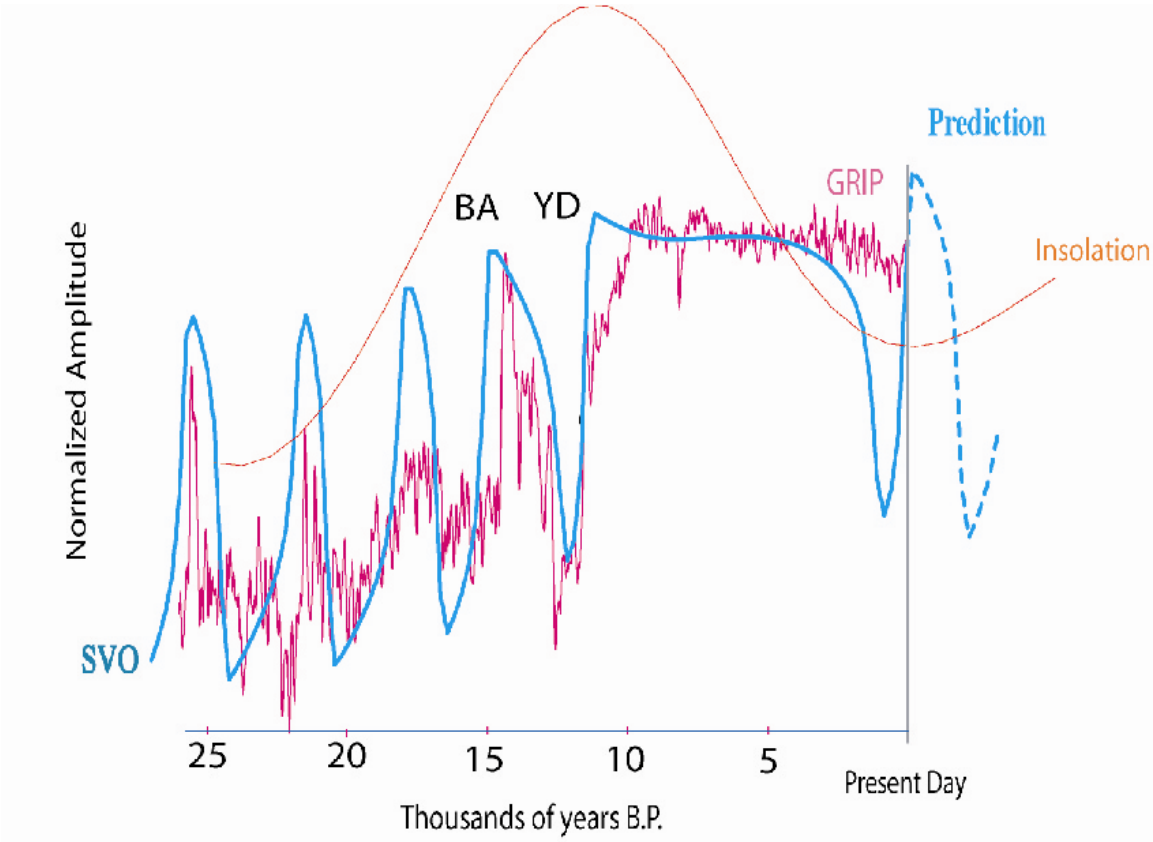

Figure 30. Detail of the last 25ky where a temperature rise simulating the melting of the ice caps has been added to the output from SVO. BA and YD are the Bølling-Allerød and Younger Dryas events respectively. The "predicted" climate swings for the next millennium include the reappearance of the downswing of the free oscillation because of the low insolation over the last and next millennia. Though the modeled amplitudes for the BA-YD sequence are close to the actual, the little ice age is greatly exaggerated.

SVO is robust to small changes in its parameters, namely, the degree of nonlinearity (which represents the strength of the sea ice-albedo and GHG feedbacks, as shown in the Appendix), the natural period of the system (estimated to be ~4ky from spectra analysis, as shown in YR), and the strength or amplitude of the forcing. Since the

natural period is obtained empirically, the simplest working model actually depends on only two adjustable parameters.

I am fully aware that abrupt climate change has been modeled with general circulation, comprehensive models as well as with low order, low dimensionality models (see for instance Stocker 2001, for many relevant references). However, as stated in Clark et al. (2002) referring in particular to the DO, "at present there exists no self-consistent model that simulates, *without prescribed forcing*, changes that resemble the palaeoclimatic record" (italics added). SVO is probably one of the simplest models able to closely simulate the DO without using any forcing other than the actual insolation forcing.

I.4.5 The role of Greenhouse Gases

ECBilt-Clio does not include an accurate representation of the carbon cycle, and adding one to it is beyond the scope of this study. However, SVO is simple enough and simulates the data closely enough that adding a simplified carbon cycle is a plausible alternative that may in fact help interpret GHG data from records such as those in Figure 31. The expectation is to be able to model the intriguing difference in response of the greenhouse gases to temperature change. As it is well known the response of methane closely parallels temperature change in Greenland (GRIP) while the response of carbon dioxide parallels the temperature in Antarctica. Nitrous oxide parallels methane but shows a slower response. These differences extend over most of the last ice age.

One possible explanation of these observations is related to the fact that large amounts of methane and nitrous oxide may be emitted from (or stored in) the tundra of the ice-free lands surrounding the Arctic, reflecting temperature and precipitation increase (or decrease) and activity (or inactivity) of microorganisms in the soils. Carbon dioxide instead follows the Antarctic temperature reflecting the dominance of the oceans as sources (Joos and Prentice 2004).

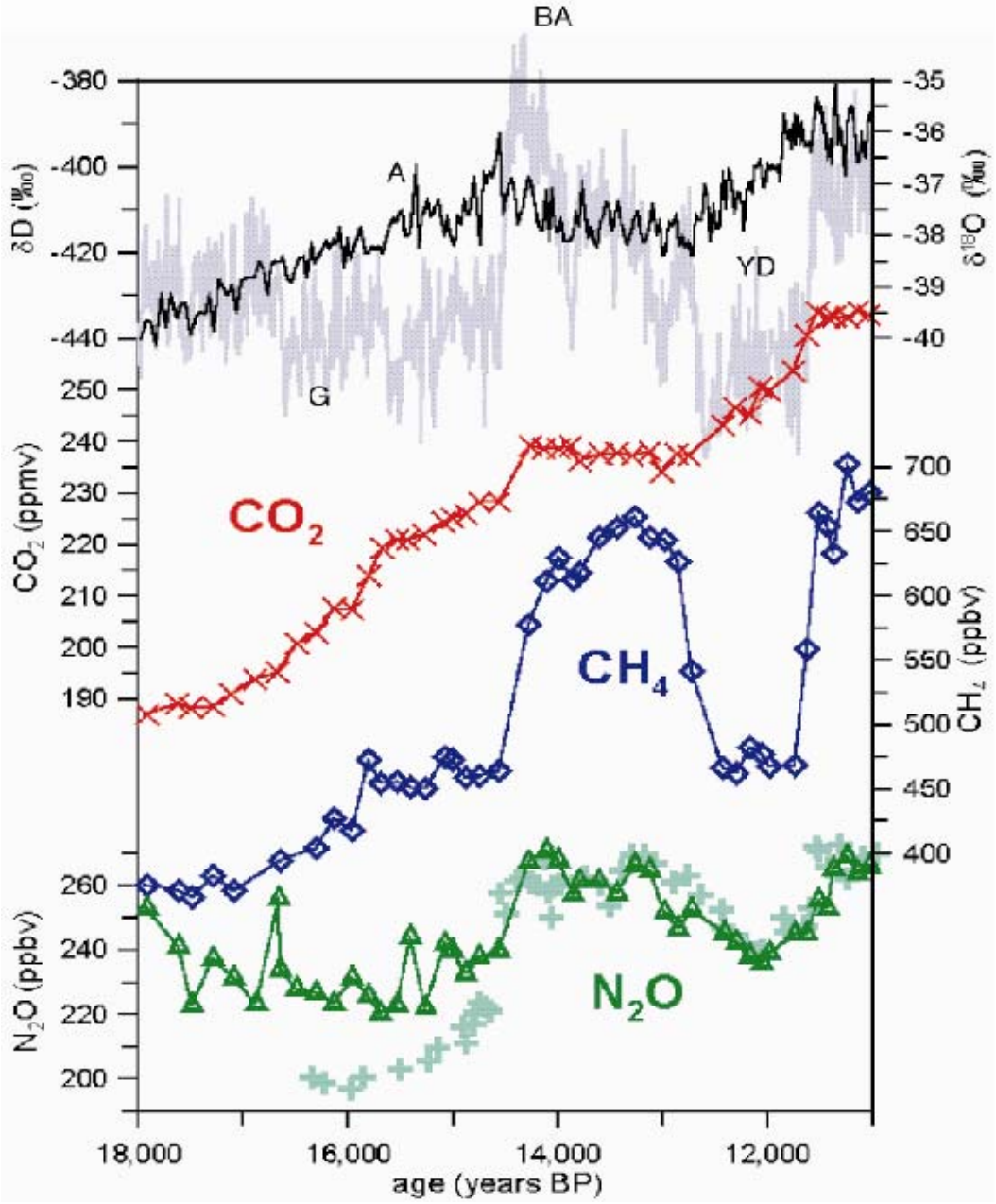

Figure 31. Greenhouse gas response to increasing temperature during the transition from the ice age to the present interglacial. BA marks the Bøllin-Allerød sequence and YD the Younger Dryas. A is the deuterium record (proxy for temperature) from Antarctica Dome C and G is the oxygen isotope record from GRIP. The CO_2 and CH_4 records are from Dome C, the N_2O records are from GRIP (crosses) and Dome C (modified from Stauffer et al., 2002).

An approach simulating these data with SVO requires that we introduce a new variable *C* in the place of the "feedback" constant coefficient ψ_2 in the van der Pol system (I.2.21) and (I.2.22) along with a third differential equation for *C*, such that the original system becomes

$$\frac{d\eta}{dt} = \phi_1\theta - \phi_2\eta \tag{I.4.2}$$

$$\frac{d\theta}{dt} = -\psi_1\eta + \psi_2 C\theta - \psi_3\eta^2\theta \tag{I.4.3}$$

$$\frac{dC}{dt} = \psi_4(C - C_0) + \phi_3\eta \tag{I.4.4}$$

Equations (I.4.2) and (I.4.3) are equations (I.2.21) and (I.2.22) in Chapter 2. Equation (I.4.4) is one of several possible forms proposed by Saltzman (2002). The new variable *C* represents the amount of undifferentiated greenhouse gas concentration in the atmosphere. The first term on the RHS of (I.4.4) represents the positive feedback that increases or decreases the amount of greenhouse gas depending on how much of it is already there compared to a reference value C_0. The second term on the RHS of the equation is proportional to temperature deviation that in turn is proportional to the time rate of change of sea ice extent. ϕ_3 and ψ_4 are positive constants.

Preliminary experiments where the magnitude of each term on the RHS of equation (I.4.4) is greatly increased independently reveal differences similar to those depicted in Figure 31. When the first term in the RHS of equation (I.4.4) is greatest, the resulting *C(t)* time series parallels the DO, correlating with the observed methane concentration and its abrupt events. When the second term is greatest, the *C(t)* time series is much less abrupt, and correlates with the CO_2 concentration. This work is still in

progress. I expect to be able to follow this and similar strategies with the expectation of closely modeling the observed difference and thus gain insight into the carbon cycle's hemispheric differences.

I.5 Conclusions

It is reasonable that to understand the DO oscillations, whose predominant periods are in the sub-Milankovitch, millennial scale, one should focus on processes internal to the climate system, and discard any inherence of orbitally induced forcing. One internal process undergoing intense scrutiny through climate modeling is the forcing of the North Atlantic with melt-water pulses (MWP) from the melting ice sheets, a process known to provoke the switching of the THC across stable states and to evolve in time scales of centuries to millennia (e.g., Knutti et al. 2004).

Many researchers in fact subscribe to the idea that the rapid cooling at the start of the Younger Dryas (YD) episode (Figure 1) was caused by the sudden collapse of the THC (e.g., Clark et al. 2002), although the recent literature reflects little agreement as to what may have triggered the collapse, whether a catastrophic flooding of the North Atlantic caused by a large MWP, or shifts in the wind patterns over the North Atlantic, due to tropical temperature anomalies of uncertain origin (Lowell et al. 2005).

No consensus appears to exist either as to what caused the abrupt warming that ended the YD around ~11ka (1ka =1000 years ago). This transition happened probably in less than 50 years, and may have been driven by a re-establishment of the THC (Taylor et al., 1997), but it is not clear what may have triggered it. The cause of the abrupt warming at the start of the Bølling-Allerød (BA) event is also an open question. The BA started with a temperature jump of over 10°C that must have occurred in a few decades or even few years (Alley 2000), some 4,000 years before the end of the YD.

Apparently, large MWPs (as revealed by the coral record from Barbados

(Fairbanks, 1989)), occurred too early (MWP-1a ~14.4ka) or too late (MWP-1b ~11.3ka) to be responsible for the initiation of the YD. Tarasov and Peltier (2005) reason however that what matters to make the THC collapse is not the amount of fresh water delivered to the oceanic basin, but its regional distribution, and propose that an Arctic discharge of fresh water through the Fram Strait, which started around 13ka, would have triggered the YD. No explanations for the equally abrupt end of the YD and beginning of the BA are given, however. More recently, the fresh water pulse mechanism (as being responsible for abrupt climate change), after a short period of widespread popularity, has come under severe criticism (e.g., Kerr, 2005).

This brief account of recent views on the subject suggests that the origin of the YD (and consequently of abrupt climate change) is quite elusive, and it may well be that we have been looking in the wrong direction. W. Broecker, after a thoughtful analysis of current evidence, concedes, "*Of course, the Younger Dryas may not have been triggered by a catastrophic freshening of the North Atlantic surface waters at all*", which has best exemplified the problem (Broecker, 2006).

In this vein, I look for alternative explanations. As simulated by the ECBilt-Clio model, the THC fluctuates between weak and strong modes. The weak mode corresponds to the cold stadial state in the last ice age and the deep water formation takes place only in the Labrador Sea. In the strong mode, the THC reaches the Nordic Seas and the northward intrusion of warm Atlantic waters generates the warm interstadial climate. This result is consistent with the idea that DO events are caused by latitude shifts of convection between Nordic Seas and the Labrador Sea, which is originally based on

sediment data (Veum et al., 1992) and is strongly supported by other model simulations (Ganopolski and Rahmstorf, 2001).

However, the main difference with Ganopolski and Rahmstorf's study is that in our experiments the latitude shifts of convection are caused by the internal dynamics of the system, while they argue that the shifts have to be started by some outside trigger, such as freshwater perturbation. However, the simulations in this study show that comparable abrupt climate changes can be induced without resorting to *ad hoc* pulses of freshwater input. (The global temperature anomaly in the first plot of Figure 4 in the Knutti et al. paper is very similar to our Figure 11). The implication is that the freshwater perturbation is not a necessary condition for the abrupt climate events to occur, as the internal dynamics of the ocean itself can trigger and sustain such changes.

The stability of the modeled THC depends on the mean climate state, which is ultimately determined by the prescribed boundary conditions. As illustrated by our experiments, the DO-like oscillation exists in the intermediate glacial boundary conditions (ICE) but is inhibited during the warm pre-industrial (PI) and cold glacial maximum (LGM) climates. Parameter sensitivity experiments with intermediate BCs between the two extremes of LGM and pre-industrial conditions show that free oscillations, similar to the ones we obtain in the ICE experiment, exist under a wide range of BCs. For example, the DO-like oscillations are also observed with boundary conditions of LGM surface albedo, GHG concentration and orbital parameters, and pre-industrial topography, indicating that the free mode of oscillations in millennial time scales is a robust feature of the model. Nonetheless, the amplitude of the oscillations is strongly dependent on the height of the continental ice sheets, implying that surface

topography has a huge impact on the stability of the THC. This might be caused by the disruption of the atmospheric circulation, such as the jet stream, in the North Atlantic by the elevated topography (Manabe and Broccoli, 1985). In fact, this result is consistent with the study by McManus et al. (1999). After investigating the marine sediment records throughout the last 0.5 million years, they argued that the variability of the climate in millennial scale might be diminished with the presence of sufficiently large ice sheets.

Since the variability of the THC is controlled by the mean climate state, a varying external thermal forcing, such as the incoming solar insolation controlled by the Milankovitch cycles, might modulate the duration and timing of the free oscillations, which are otherwise chaotic. This idea is supported by the ORB experiment. Within the scaled-down 20 ky simulation, the irregular free oscillations are organized and entrained by the external solar forcing, and the sequence of the recorded DO events is better simulated. Similar results are also obtained by using an independent conceptual model SVO. As suggested by Rial and Yang (2006), this frequency and amplitude modulation appears then to be a possible explanation for the origin of the puzzling characteristic time distribution of the DO pulses. If this proves to be correct, and since astronomical forcing is readily predictable, naturally induced abrupt climate change events might eventually be anticipated by the best climate models available.

CHAPTER II

MODELING SUBSURFACE FRATURE SYSTEMS

II.1 Summary

Shear-wave splitting polarization (p) and delay time (Δt) observations are used to invert for fracture orientation and intensity of fracturing, simultaneously. By addressing the different levels of uncertainty involved in measurements of these two parameters, as well as their dissimilar relationships to fracture configuration, I developed an inversion algorithm which reduces the primary double-response inversion to two connected single-response ones. I show that its inherent nonlinearity complicates this problem, which therefore requires a more sophisticated attack than conventional inversion schemes. It will be shown that the construction of residue function contours in the model plane and the generation of surrogate data by simulation process are essential to this approach. I illustrate the capabilities of this technique by inverting shear-wave splitting data from The Geysers geothermal reservoir in California. In principle the method should be useful to characterize fractured reservoirs, whether geothermal or hydrocarbon.

II.2 Introduction

Shear wave splitting observations obtained by dense arrays of seismic stations have been used to characterize fracture or crack systems beneath the surface of seismically active regions, as well as the distribution of the local stress fields (Crampin et.al., 1996; Zatsepin and Crampin, 1997; Lou and Rial, 1997). The polarization of the fast split shear wave is generally a robust parameter and used to deduce the direction of fractures. The delay time data are less stable since they include higher observational errors and contributions other than shear-wave splitting. The problem of scatter in delay time observations has been addressed by Crampin et al. (2002), who argue that every small earthquake changes the stress field around the fault plane and causes variations in the length of the raypath portion which contains high-pressure fluids. Such rapid variations are expected to produce important scatter in observed delay times (Crampin et al., 2004). Nevertheless, delay times can detect the presence of faulting or highly cracked rock, and can be successfully used as complementary to polarizations in detecting the crack structure as well as an indicator or index of the medium's anisotropy (Elkibbi and Rial, 2004).

Traditional techniques use polarization and delay time observations independently or nearly independently, and make inferences about crack geometry from polarizations, and about crack density from delay times (Rial and Lou, 1996; Lou et. al., 1997; Erten and Rial, 1999; Vlahovic et al., 2002). In this study however, I recognize that both polarization and delay time behaviors are controlled by the overall subsurface fracture configuration, and thus I employ both of them simultaneously to model the fracture

system. This premise defines a double-response regression problem (Draper and Smith, 1998).

Here I discuss in detail a novel inversion strategy to tackle the complexities raised by the double-response inversion. In Section II.3 I specify the main assumptions. The stiffness matrix models for the anisotropic cracked media and the equations governing the behavior of the shear waves propagating through an anisotropic medium are also described. These facts provide the theoretical basis for the inversion strategy that is introduced in Section II.4. I demonstrate that the primary double-response problem can be divided into two connected single-response regressions. For a given crack density, the residue functions of crack strike and dip are defined, calculated and contoured on the model plane. I also construct a simulation process to generate error-free or error-contaminated surrogate data. In Section II.5, the power of the inversion scheme is shown by applying it to the observational data obtained from The Geysers geothermal field in California (Elkibbi and Rial, 2003). I illustrate how the reliability of the inversion results can be evaluated by comparing the residue function contours' topographies of the real and surrogate data. Although the majority of the estimated crack models are consistent with previous studies, several exceptions are found. Section A6 shows how to make use of the residue function contours and surrogate data to treat these discrepancies. In the final section I discuss key points of the approach.

II.3 Main Assumptions and Wave Theory

II.3.1 Assumptions

In this study it is assumed that the seismic anisotropy is mainly induced by open cracks, microcracks and preferentially oriented pore spaces. It is also assumed that all the fractures in the vicinity of the recording station have the same orientation, and are approximately uniformly distributed.

Hudson, in a series of papers (Hudson 1980, 1981, 1986, 1988, 1990; Peacock and Hudson, 1990), derived the effective elastic constants in the distributions of aligned cracks, either dry or wet. Hudson assumed that the average effect of an irregular-shaped crack can be approximated by that of a flat ellipsoid, whose dimension is negligible compared to the wavelength of the seismic waves, and aspect ratio (minor axis over major axis) is much smaller than unity. All these assumptions are retained in this study.

II.3.2 Elastic Stiffness of Anisotropic Medium

For isotopic and homogenous elastic medium, the stiffness matrix is well defined and expressed as

$$\overline{\overline{C}}_O = \begin{bmatrix} \lambda+2\mu & \lambda & \lambda & 0 & 0 & 0 \\ \lambda & \lambda+2\mu & \lambda & 0 & 0 & 0 \\ \lambda & \lambda & \lambda+2\mu & 0 & 0 & 0 \\ 0 & 0 & 0 & \mu & 0 & 0 \\ 0 & 0 & 0 & 0 & \mu & 0 \\ 0 & 0 & 0 & 0 & 0 & \mu \end{bmatrix} \qquad \text{(II.3.1)}$$

A small concentration of cracks or thin pores in the otherwise isotropic matrix generally weakens the rock, and hence reduces the overall elastic stiffness by an amount

proportional to the crack porosity ϕ_c. For instance, the stiffness matrix of the HTI (horizontal transverse isotropy) cracked medium is

$$\overline{\overline{C}}_A = \overline{\overline{C}}_O - \phi_c \times \begin{bmatrix} (\lambda+2\mu)b_n & \lambda b_n & \lambda b_n & 0 & 0 & 0 \\ \lambda b_n & (\lambda+2\mu)\zeta^2 b_n & \lambda\zeta b_n & 0 & 0 & 0 \\ \lambda b_n & \lambda\zeta b_n & (\lambda+2\mu)\zeta^2 b_n & 0 & 0 & 0 \\ 0 & 0 & 0 & 0 & 0 & 0 \\ 0 & 0 & 0 & 0 & \mu b_t & 0 \\ 0 & 0 & 0 & 0 & 0 & \mu b_t \end{bmatrix} \tag{II.3.2}$$

The porosity ϕ_c is defined by

$$\phi_c = \frac{4\pi\alpha e}{3} \tag{II.3.3}$$

where α denotes the aspect ratio and e the crack density. And

$$\zeta = \frac{\lambda}{\lambda+2\mu} \tag{II.3.4}$$

The boundary conditions index b_n depends on the nature of the cracks and their fill,

$$b_n^{gas} = \frac{1}{\pi\alpha\eta(1-\eta)} \tag{II.3.5}$$

$$b_n^{liq} = \frac{b_n^{gas}}{1+\eta_n b_n^{gas}} \tag{II.3.6}$$

And b_t is common to both gas- and liquid-filled cracks and given by

$$b_t = \frac{4}{\pi\alpha(3-2\eta)} \tag{II.3.7}$$

with $\eta = \frac{\mu}{\lambda+2\mu}$, and $\eta_n = \frac{\mu^{liq}}{\lambda+2\mu}$. And μ^{liq} is the shear modulus of the liquid in the cracks (MacBeth, 1999).

The elastic stiffness with cracks of other orientations can be calculated by transformation of $\overline{\overline{C}}_A$. This model can simulate any one of a variety of crack, pore or fracture styles, ranging from a volume distribution of intergranular or intragranular cracks to the surface distributions of large-scale shear fractures (Macbeth, 1999).

II.3.3 Kelvin-Christoffel Equation

Wave propagation in elastic media is described by the equation of elastic motion,

$$\nabla \cdot \overline{\overline{\sigma}} + \vec{f} = \rho \frac{\partial^2 \vec{u}}{\partial t^2} \tag{II.3.8}$$

where $\overline{\overline{\sigma}}$ is the stress tensor, $\vec{f}$ denotes the body density force vector in the media; $\vec{u}$ represents the elastic displacement vector and ρ is the mass density. Hooke's Law relates $\overline{\overline{\sigma}}$ to the strain tensor $\overline{\overline{\varepsilon}}$ by the fourth-order elastic constant tensor $\overline{\overline{C}}$ through

$$\overline{\overline{\sigma}} = \overline{\overline{C}} : \overline{\overline{\varepsilon}} \tag{II.3.9}$$

For the required anisotropic medium, $\overline{\overline{C}}$ is reduced to a 6×6 stiffness matrix, i.e. $\overline{\overline{C}}_A$ (in Equation II.3.2), by using the symmetries of Equation II.3.2.

Assuming $\overline{\overline{C}}_A$ does not depend on time or wave frequency, the displacement is expressed by the plane wave

$$\vec{u} = \vec{u}^0 \exp(i(\omega t - \vec{k} \cdot \vec{x}) \tag{II.3.10}$$

where $\vec{u}^0$ is the vector describing the direction of propagation and amplitude of the wave, ω, $\vec{k}$ and $\vec{x}$ denotes the wave frequency, wave vector and position vector, respectively.

Defining

$$\overline{\overline{L}} = \frac{1}{\left\| \vec{k} \right\|} \begin{bmatrix} k_1 & 0 & 0 & 0 & k_3 & k_2 \\ 0 & k_2 & 0 & k_3 & 0 & k_1 \\ 0 & 0 & k_3 & k_2 & k_1 & 0 \end{bmatrix} \tag{II.3.11}$$

with $\vec{k} = (k_1, k_2, k_3)$ and substituting (II.3.9) - (II.3.11) into (II.3.8), yields

$$(\overline{\overline{\Gamma}} - \rho v^2) \cdot \vec{u} = 0 \tag{II.3.12}$$

with $\overline{\overline{\Gamma}} = \overline{\overline{L}} \cdot \overline{\overline{C}}_A \cdot \overline{\overline{L}}^T$ and v is the wave speed. This equation is the Kelvin-Christoffel equation (Carcione 2001), and has the form of an "eigenequation" with eigenvalues ρv_j^2 $(j = 1,2,3)$ (magnitudes in descending order) and the corresponding eigenvectors $\overrightarrow{v_j}$.

By definition, the polarization direction p is the angle from north to the horizontal projection of the second eigenvector $\overrightarrow{v_2}$ and is calculated by

$$p = \tan^{-1}\left(\frac{\overrightarrow{v_{2x}}}{\overrightarrow{v_{2y}}}\right) \tag{II.3.13}$$

and the delay time Δt, normalized by the length of the ray, depends only on the magnitudes of shear wave velocities v_2 and v_3, and has the form of

$$\Delta t = \frac{1}{\sqrt{v_2}} - \frac{1}{\sqrt{v_3}} \tag{II.3.14}$$

Figure 32 illustrates synthetic results for polarizations and delay times computed by the foregoing theory for a given crack model.

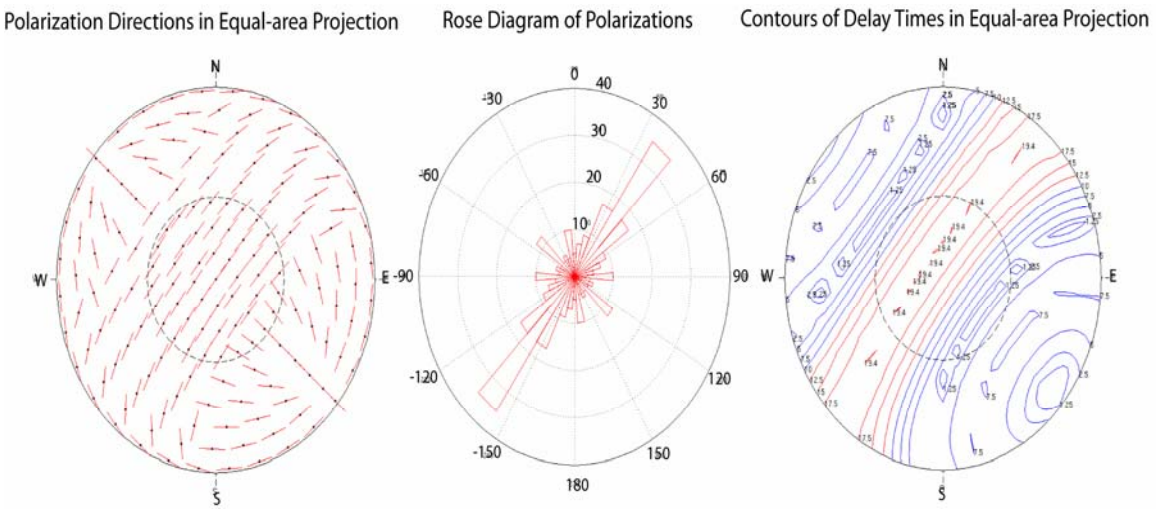

Figure 32. Theoretical polarizations (left), rose diagram (center), and time delay contours (right) for a synthetic crack system with strike 40° (crack strike is measured clockwise from North), dip 80° (crack dip is measured from the horizontal plane with downward south positive), and average crack density 0.05. The small circle encloses the shear wave window (~35°), inside which the shear-wave splitting observations are free of interference from the surface and used in this study.

II.4. Inverse Modeling

II.4.1 A double-response Inverse Problem

As shown by (II.3.13) and (II.3.14), both the polarization p and delay time Δt are functions of wave vector $\vec{k}$ (described by the incident angle I and back azimuth B) as well as crack strike φ, crack dip θ and crack density e. Suppose now we have n observations p_i and Δt_i $(i = 1,2,\ldots,n)$, equations (II.3.13) and (II.3.14) can be rewritten as

$$p_i = p(I_i, B_i; \varphi, \theta, e) \tag{II.4.1}$$

$$\Delta t_i = \Delta t(I_i, B_i; \varphi, \theta, e) \tag{II.4.2}$$

Since the measurement errors are unavoidable, the observations p_i and Δt_i are better represented by

$$p_i = p(I_i, B_i; \varphi, \theta, e) + \varepsilon_{1i} \tag{II.4.3}$$

$$\Delta t_i = \Delta t(I_i, B_i; \varphi, \theta, e) + \varepsilon_{2i} \tag{II.4.4}$$

where ε_{1i} and ε_{2i} are randomly distributed noises.

Hence, this is a double-response regression problem, which means, both polarization p and delay time Δt are used simultaneously to invert for the fracture attributes φ, θ and e.

One important characteristic makes this problem unique: According to Macbeth's stiffness matrix and the Kelvin-Christoffel equation, polarizations are basically insensitive to variation in crack density, while delay times are approximately linearly proportional to it. This makes it possible to simplify the original problem by two connected single-response inversion processes, as discussed in detail in the next section.

II.4.2 Nonlinear Inversion and Numerical Procedure

In this approach, I model the crack parameters based on the nonlinear least squares rule. For a given crack density e^*, (II.4.3) becomes

$$p_i = p(I_i, B_i; \varphi, \theta, e^*) + \varepsilon_{1i} \tag{II.4.5}$$

and the corresponding root mean squares (RMS) of the residues is calculated by

$$s_1(\varphi, \theta) = \sqrt{\frac{\sum_{i=1}^{n} [p_i - p(I_i, B_i; \varphi, \theta, e^*)]^2}{n-2}} \tag{II.4.6}$$

Therefore, the crack strike and dip are approached as $s_1(\varphi, \theta)$ reaches its minimum. Since polarizations are roughly irrelevant to the crack density, this regression provides an estimate of the real crack strike and dip to the first order of approximation.

Substituting the estimated crack strike φ^* and dip θ^* to (II.4.4), we have

$$\Delta t_i = \Delta t(I_i, B_i; \varphi^*, \theta^*, e) + \varepsilon_{2i} \tag{II.4.7}$$

The crack density estimate is then obtained by minimizing the RMS of the residue for delay times

$$s_2(e) = \sqrt{\frac{\sum_{i=1}^{n} [\Delta t_i - \Delta t(I_i, B_i; \varphi^*, \theta^*, e)]^2}{n-1}} \tag{II.4.8}$$

Next, the regressed crack density is applied back to (II.4.4) and the same procedure as mentioned above is followed. The numerical loop is terminated and the final estimate $(\hat{\varphi}, \hat{\theta}, \hat{e})$ is reached as certain predefined tolerance is satisfied. The detailed flow chart of the numerical procedure is depicted by Figure 33.

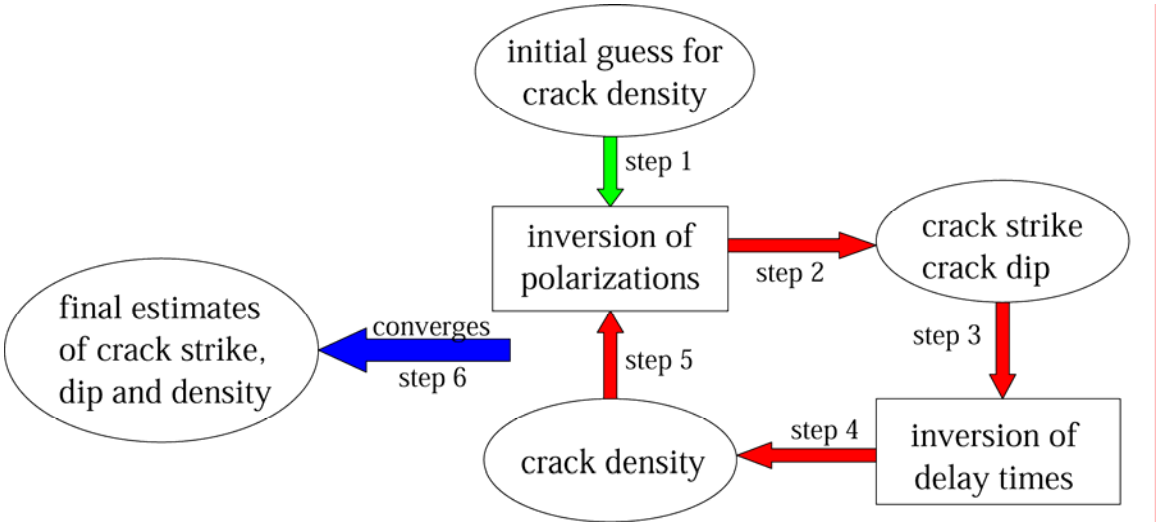

Figure 33. Flow chart of the inversion algorithm. The inversion is initialized by a guess of crack density (step 1). We then estimate the crack strike and dip from polarization data by assuming the crack density to be constant (step 2). Next, we assume the estimated crack strike and dip to be constant crack properties (step 3), and invert for the crack density under this circumstance (step 4). Then, we use the newly estimated crack density to replace the previous value (step 5), and estimate the crack strike and dip from polarization data again (step 2), and so on. When the iteration converges to some predefined tolerance, the foregoing loop stops and the final estimated crack strike, dip and density are obtained (step 6).

II.4.3 Residue Function Contours

For a given crack density such as $\hat{e}$, I define the residue function of crack strikes and dips for polarizations as

$$r_1(\varphi,\theta)=\sqrt{\frac{\sum_{i=1}^{n}[p_i-p(I_i,B_i;\varphi,\theta,\hat{e})]^2}{n-2}} \qquad \text{(II.4.9)}$$

which is identical to (II.4.6) (i.e. RMS of the residues for polarizations). To visualize this distribution, we construct a 2-D model space with the x-axis representing the crack strike and the y-axis the complement angle of the crack dip, and contour the residue function on this plane (Figure 34). Theoretically the nonlinear least squares rule requires that the regressed crack strike and dip be inferred from the point where the global residue function minimum is located (Seber and Wild, 1989; Draper and Smith, 1998). Obviously, the modeled crack strike and dip from this method are identical to previously obtained $\hat{\varphi}$ and $\hat{\theta}$.

Analogously, the residue function for delay times is defined as

$$r_2(\varphi,\theta)=\sqrt{\frac{\sum_{i=1}^{n}[\Delta t_i-\Delta t(I_i,B_i;\varphi,\theta,\hat{e})]^2}{n-2}}. \qquad \text{(II.4.10)}$$

And its contours are computed, too (Figure 34). The crack strike and dip regressed from (II.4.11) are generally different from $\hat{\varphi}$ and $\hat{\theta}$. However, the difference should be minor if our assumptions of the crack system are correct and the elastic constants of the cracked medium are well represented by the Macbeth's stiffness matrix.

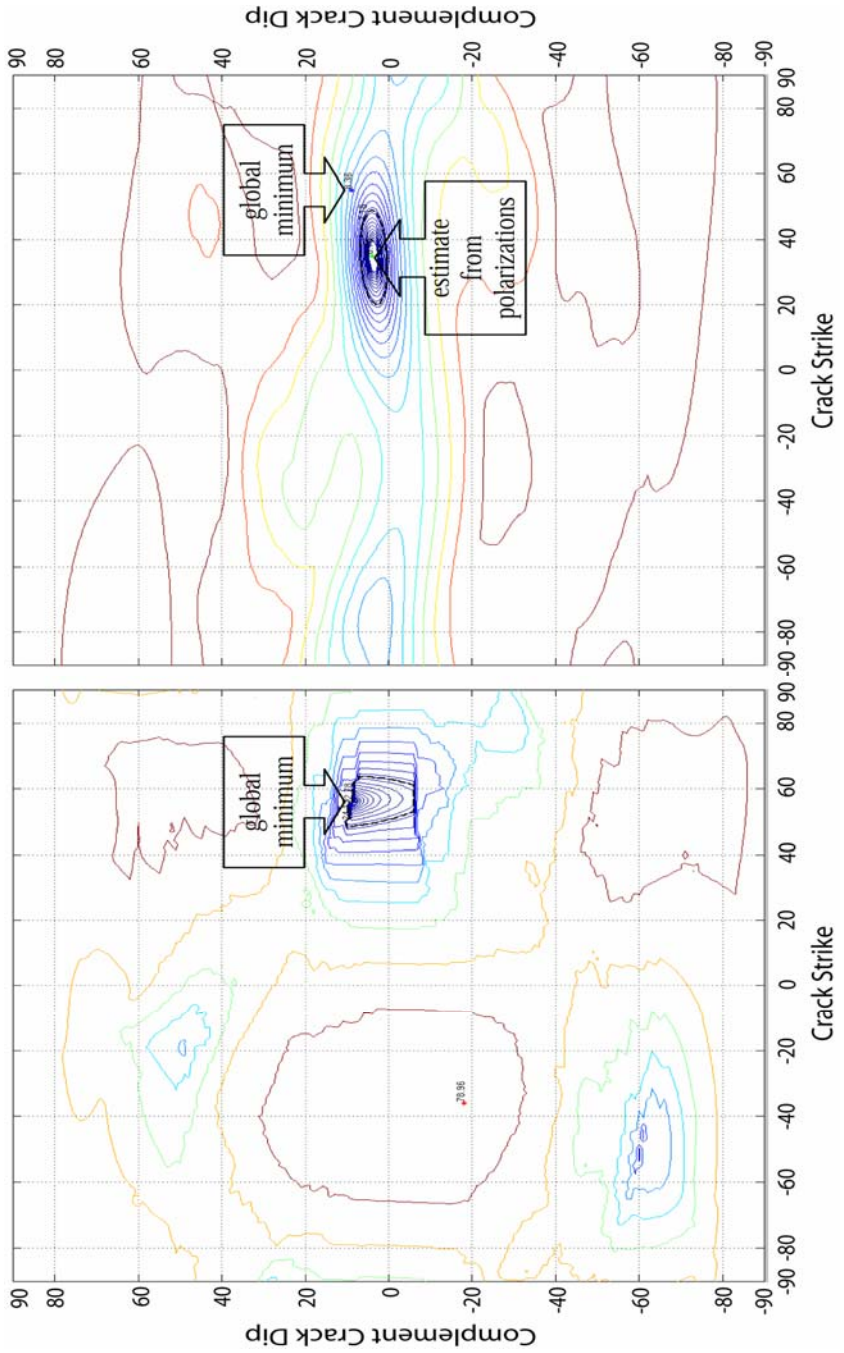

Figure 34. A 2-D model space is constructed, with the x-axis representing the crack strike φ and the y-axis the complement angle of the crack dip θ. If φ is positive the complement crack dip equals (90°-θ); and if φ is negative, it is -(90°-θ). The residue function contours are drawn (inverted by the scheme described by Figure 2) for recorded polarizations (left) and delay times (right) at station4 in NW Geysers in 1994. Thick black lines represent 95% confidence limit for modeled crack strike and dip.

II.4.4 Simulation Process

Substituting the modeled crack system $(\hat{\varphi}, \hat{\theta}, \hat{e})$ to equations (II.4.1) and (II.4.2), we may generate error-free surrogate polarizations $\tilde{p}_i$ and delay times $\Delta\tilde{t}_i$,

$$\tilde{p}_i = p(I_i, B_i; \hat{\varphi}, \hat{\theta}, \hat{e}) \tag{II.4.11}$$

$$\Delta\tilde{t}_i = \Delta t(I_i, B_i; \hat{\varphi}, \hat{\theta}, \hat{e}) \tag{II.4.12}$$

Moreover, we may also create error-contaminated surrogate data by adding synthetic errors with the approximate variances of the measurements to the above equations.

These surrogate data can then be applied to the same inversion procedure as described in section II.3.2, and produce their own residue function contours.

II.5 Applications

I applied this inversion scheme to numerous recordings from a number of seismic sites in The Geysers geothermal field, California, where the seismic events are typically shallower than 5 km. Two seismic arrays deployed in the NW and SE areas of The Geysers provided the seismographic data. In the NW Geysers seismic data were collected by a 16-station, digital, 3-component array. All 16 geophones recorded at 400 samples/sec and were buried about 30 meters below the ground surface. In the SE Geysers the data were recorded by a 12-station, digital, 3-component array recording at 480 samples per sec. All 12 stations had geophones on the ground surface, which did not perceptibly affect the quality of the seismic data as compared to the NW buried instruments. This is because noise levels contained in the data were generally relatively low (Elkibbi and Rial, 2003).

I assume the mass density of the rocks in The Geysers to be $2.7\times10^{3}\,kg/m^{3}$, and the cracks fully saturated by water and embedded in an otherwise isotropic matrix. We also assume the background rock matrix has zero porosity. The Lamé constants λ and μ are estimated from local vertical P-wave and S-wave velocity profiles in the NW and SE Geysers, respectively (Romero 1995; Kirkpatrick et. al., 1997). In the NW Geysers, both λ and μ are about $2.8\times10^{10}\,Pa$ with slight difference. However, In the SE Geysers λ is equal to $2.0\times10^{10}\,Pa$ and μ equals $2.6\times10^{10}\,Pa$.

Changes in crack aspect ratio can be produced by variations in the applied stresses as well as in the saturating fluid pressure. Delay times from shear-wave splitting measurements are sensitive to such changes in crack aspect ratio, i.e. equation (II.3.3). Therefore, it is important to use crack aspect ratio as another parameter in the inversion

scheme for fracture geometry and fracture density. In this approach, although a constant aspect ratio of 0.01 is assumed for simplicity, it is also possible to invert for fracture attributes with varying aspect ratios. In fact, the complete fracture inversion results from The Geysers appears in a companion paper (Elkibbi et al., 2004), in which we discuss the shear-wave splitting data thoroughly, invert for fracture strike and dip, fracture aspect ratio, and fracture density, and then relate these fracture attributes to the local geology and tectonic setting.

As an example, we applied the inversion scheme to the observations in station4 in NW Geysers. The outcome of the inversion gives a crack system striking N55E, dipping 81S and 0.061 crack density. The contours of $r_1(\varphi,\theta)$ and $r_2(\varphi,\theta)$ are shown in Figure 34. The main characteristic of these two plots is that the locations of the global minima for both are very close in the model plane, as anticipated from theoretical reasoning.

After generating surrogate data sets, we apply the same inversion approach to them. The error-free simulated data produced an identical crack model; while the surrogate data including synthetic errors produced a slightly different model (Figure 35). This strong agreement indicates robustness in the inversion scheme at least for this data set (indeed, this is the case for most of our data).

More importantly, Figure 35 reveals that the topographies of the three residue function contours, that is, those calculated from the observational, the error-free and the error-contaminated surrogate polarizations, are quite similar (i.e., the locations of their minima and maxima). In fact, this resemblance emerges frequently throughout this study. (The residue function of the delay times is less significant because of their relatively

higher uncertainty; hence delay times are not suitable for visual inspection.) The estimated models for some selected stations are listed in Table 3.

To summarize, the majority of modeled cracks in The Geysers are vertical or nearly vertical, and the variations in detected crack densities are slight. However, there are several exceptions. For instance, observations in station 6 in NW Geyser in 1988 are modeled by a very shallow crack system, i.e. dipping 30° south. Another example comes from station 1 in SE Geysers in 1999. The estimated crack dip is even shallower (22° to the south) and crack density is extremely high, i.e. 0.13. Since there is little geological evidence for low angle open cracks and large fracture intensity in The Geysers (Elkibbi et al., 2004), the detection of what appears to be anomalous crack dips and densities probably indicate that the present nonlinear inversion procedure is unsuccessful in these stations and further action must be considered.

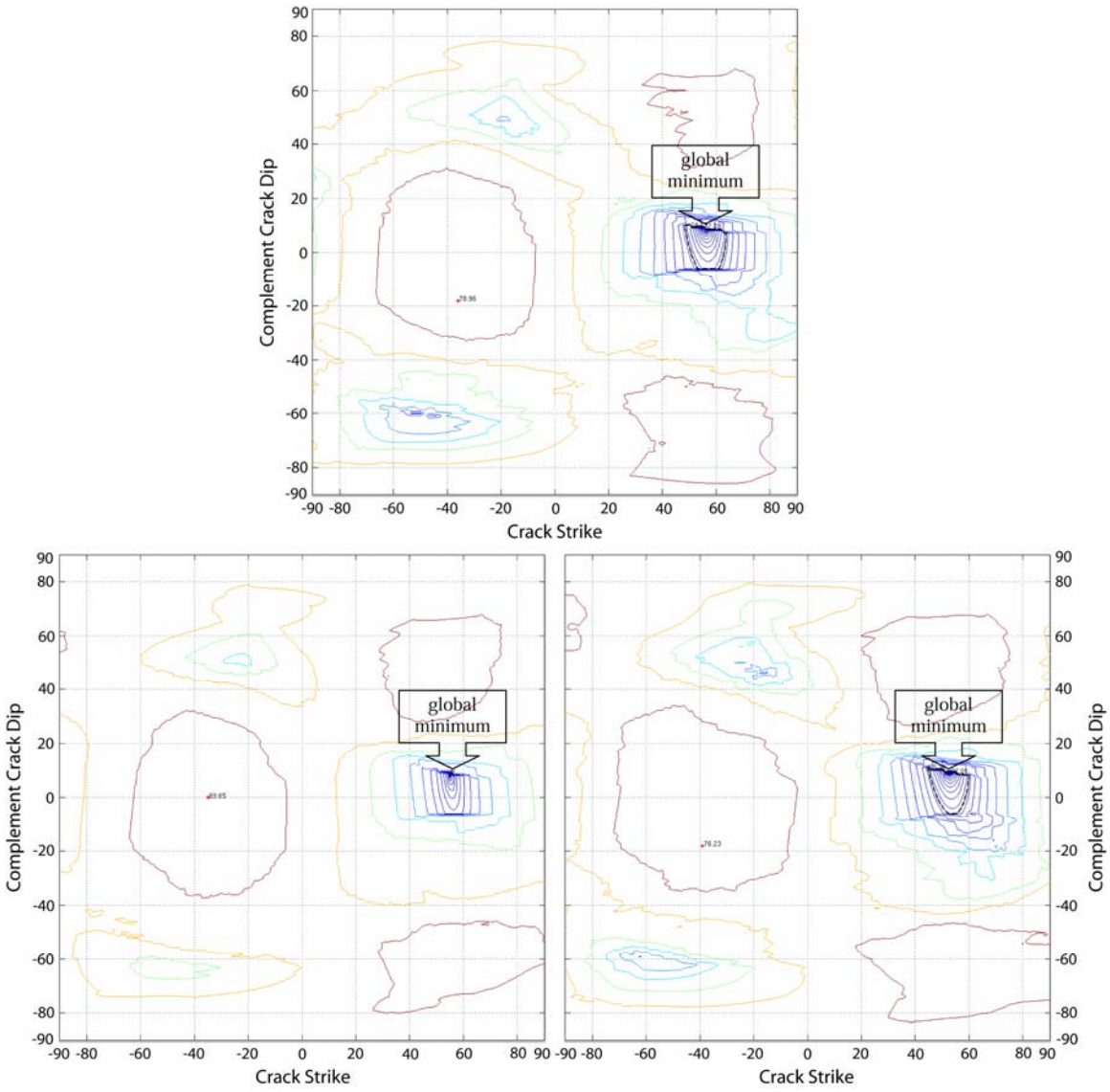

Figure 35. The residue function contours calculated from observed polarizations (top) at station4 in NW Geysers in 1994 as well as simulated ones without (bottom left) and with (bottom right) artificial errors. The global residue function minimum from each of these three data sets is marked and their concordance is striking. Furthermore, the resemblance of the whole topographies of the contours is also pronounced.

Table 3. Estimated fracture models from global minima of the residue functions in NW and SE Geysers. (From left to right, the columns represent the station names, the numbers of observations used, RMS of the residues calculated from estimated models for polarizations, estimated crack strikes (degrees from North), dip (degrees downward South positive), RMS of the residues calculated from estimated model for delay times, and estimated crack densities, respectively. This notation is also applicable to Table 4.)

Station	# of obs	rms of p	crack strike	crack dip	rms of Δt	crack density
NW-S01A-88	56	25.08	-18	85	5.19	0.03
NW-S02A-88	45	29.51	7	-74	4.39	0.026
NW-S06A-88	58	33.29	-21	-30	6.15	0.057
NW-S12A-88	32	32.44	58	-47	3.58	0.049
NW-S14A-88	34	19.19	25	24	6.05	0.091
NW-S01A-94	33	28.5	-17	-55	10.19	0.059
NW-S04A-94	54	22.78	55	81	8.36	0.061
NW-S06A-94	62	37.48	-60	-13	12.2	0.143
NW-S11A-94	45	21.01	21	86	14.13	0.078
SE-S01A-99	14	31.1	-22	-31	15.62	0.13
SE-S06A-99	66	28.13	-23	-74	6.76	0.051
SE-S14A-99	130	35.15	1	37	6.17	0.064

II.6 Correcting Estimates

Unlike the linear case, the RMS of the residues may have one global minimum as well as several local minima in a nonlinear process (Seber and Wild, 1989). And it is logical to examine the local minima in case the global minimum couldn't offer a credible answer. The topography of $r_1(\varphi,\theta)$ contours for this dataset is scrutinized and compared to those from simulated data. What follows exemplifies this idea.

For the shear-wave splitting data from station 6 in NW Geysers in 1988, I create the surrogate data and draw the corresponding residue function contours. The lack of resemblance between the residue function contour topographies of the actual and surrogate data (Figure 36) may indicate that our suspicion is warranted.

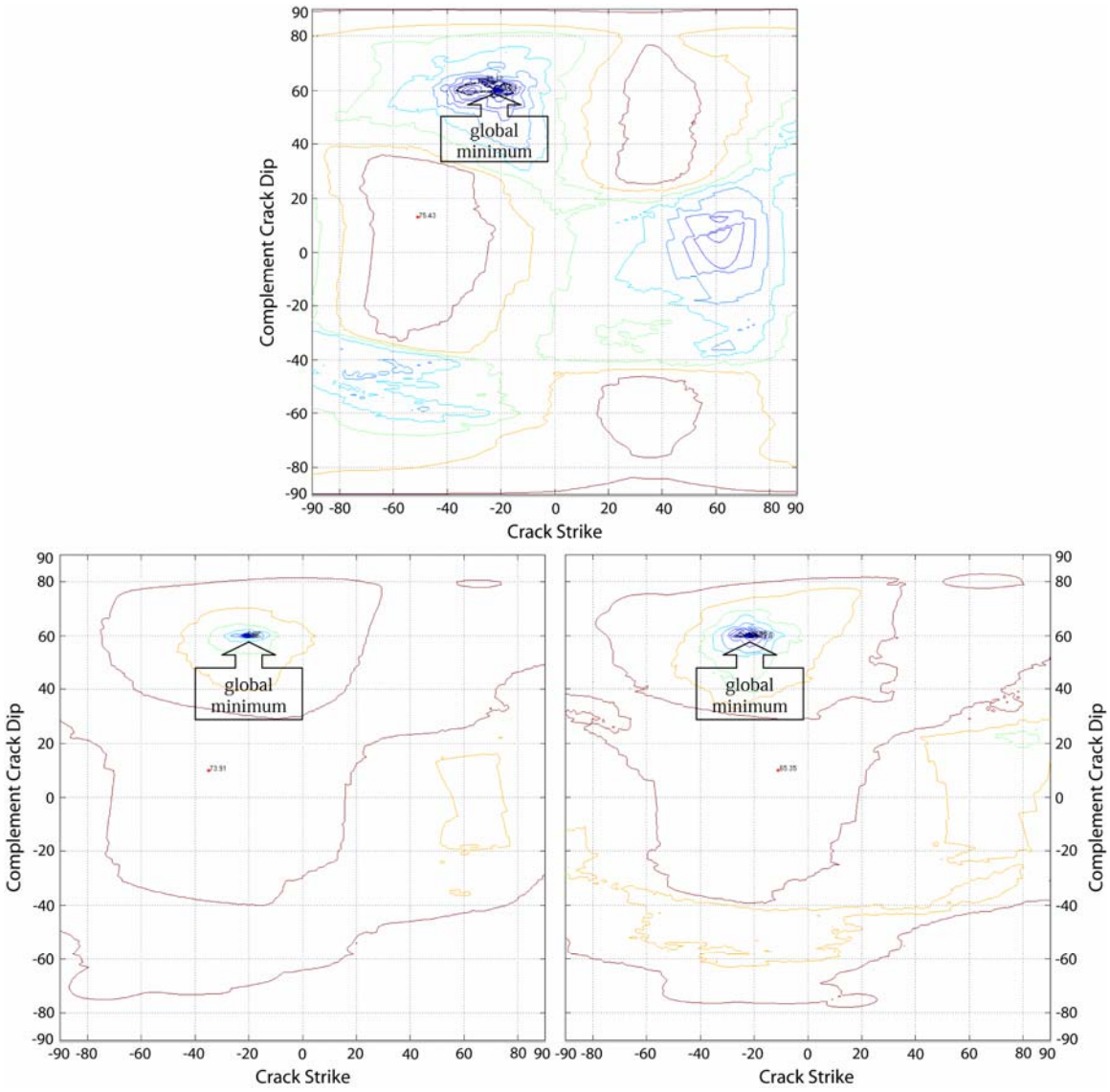

Figure 36. The residue function contours calculated from observed polarizations (top) at station6 in NW Geysers in 1988 as well as from simulated ones without (bottom left) and with artificial errors (bottom right). The similarity of the topographies of experimental contours and surrogate contours doesn't exist anymore.

Exploring the contour plot for the real data suggests that the most prominent local minimum is in the right middle part of the polarization contour plot. If the model is constrained within this range, the estimated crack strike changes from N21E to N60E,

crack dip becomes 83N and crack density is reduced from 0.057 to 0.026. According to this newly obtained crack model, I generate the surrogate data and invert them. The residue functions $r_1(\varphi,\theta)$ for the real and surrogate data are computed and contoured. Figure 37 shows that the resemblance of the topographies of the three contour plots has been substantially enhanced. Furthermore, we may speculate that the observed global residue function minimum is indeed one of the local minima, but randomly exaggerated by errors, as pointed out in Figure 37.

After implementing this correcting procedure to all the suspected models, the final results are summarized in Table 4. The corrected models are now more consistent with nearby crack systems, as well as with the local geology and tectonics. The only exception comes from station14 in SE Geysers. The fracture system underneath this station may be too complicated to be modeled by parallel uniform cracks. Indeed, there might exist three intersecting sets of fractures in the neighborhood of this station (Elkibbi et al., 2004).

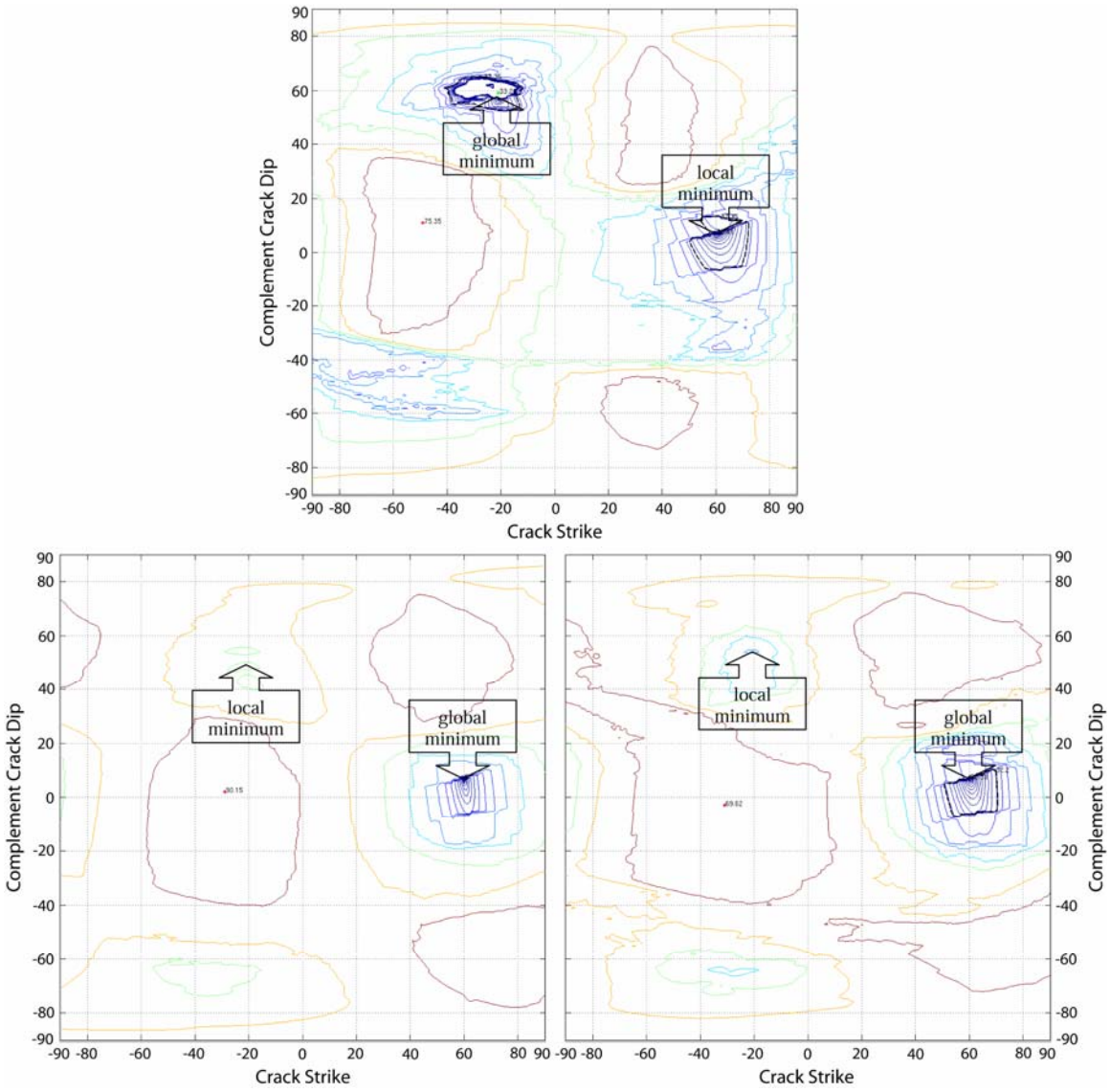

Figure 37. The residue function contours calculated, based on the local minimum, from observed polarizations (top) at station6 in NW Geysers in 1988 as well as from simulated ones without (bottom left) and with (bottom right) artificial errors. The resemblance of the topographies of the three contour plots is enhanced substantially comparing to Figure 5. The global minimum in the observed data is probably represented by a local minimum in both simulation data sets.

Table 4. Corrected estimated fracture models in The Geysers. (The bold fonts highlight the models that are estimated from local minima.)

station	# of obs	rms of p	crack strike	crack dip	rms of Δt	crack density
NW-S01A-88	56	25.08	-18	85	5.19	0.03
NW-S02A-88	45	29.51	7	-74	4.39	0.026
NW-S06A-88	**58**	**35.41**	**60**	**83**	**4.05**	**0.026**
NW-S12A-88	**32**	**32.75**	**40**	**85**	**4.75**	**0.041**
NW-S14A-88	**34**	**19.99**	**34**	**83**	**6.32**	**0.066**
NW-S01A_94	**33**	**32.38**	**-12**	**86**	**8.86**	**0.057**
NW-S02A-94	**18**	**27.22**	**-3**	**74**	**13.4**	**0.076**
NW-S04A-94	54	22.78	55	81	8.36	0.061
NW-S06A-94	**62**	**39.74**	**41**	**-83**	**12.15**	**0.056**
NW-S11A-94	45	21.01	21	86	14.13	0.078
SE-S01A-99	**14**	**43.27**	**80**	**-74**	**13.86**	**0.059**
SE-S06A-99	66	28.13	-23	-74	6.76	0.051
SE-S14A-99	130	35.15	1	37	6.17	0.064

II.7 Conclusions

The strong nonlinearity of this inverse problem creates substantial complexity, and the relatively higher uncertainty in delay time data makes the situation even worse. This study sheds some light onto this challenge. The main idea here is to simplify the inversion process by dividing the double-response regression problems into two connected single-response ones.

For each shear-wave splitting data set, the residue functions for polarizations and delay times are calculated. Their contour plots provide a vivid way to recognize their variations on the model plane. Surrogate data with and without synthetic errors are generated according to inverted crack model. The residue functions of polarizations for the real and surrogate data are of particularly interest to this approach. According to the similarity of the topographies of their contour plots, we may evaluate the reliability of the proposed inversion results.

In practice, it is possible for the automatic inversion procedure described in this paper to produce non-realistic crack models. We have shown, however, how to treat these discrepancies by making use of the local minima of the residue function for polarizations to do the inversion.

This approach has been successfully applied to the shear wave splitting data obtained from The Geysers geothermal fields in California, and is presumably applicable to artificially generated shear waves that split in cracked hydrocarbon fields.

BIBLIOGRAPHY

Adam, J., and Faure, H. (1997). Paleovegetation maps of the Earth during the last glacial maximum, and the early and mid Holocene: an aid to archaeological research. *Journal of Archaeological Sciences*, 24, 623-647.

Alley, R.B. (2000). The Younger Dryas cold interval as viewed from central Greenland. *Quat. Sc. Rev*., 19, 213-226.

Alley, R.B., Marotzke, J., Nordhaus, W. D., Overpeck, J. T., Peteet, D. M., Pielke Jr, R. A., Pierrehumbert, R. T., Rhines, P. B., Stocker, T. F., and Talley, L. D. (2003). Abrupt climate change. *Science*, 299, 2005-2010.

Alley, R.B., Anandarkrishnan, S. and Jung, P. (2001). Stochastic resonance in the North Atlantic. *Paleooceanography*, 16, 190-198.

Bard, E. (2003). North-Atlantic sea surface temperature reconstruction. *IGBP PAGES/World Data Center for Paleoclimatology Data Series #2003-026.* NOAA/NGDC Paleoclimatology Program, Boulder CO, USA.

Bender, M., Sowers, T., Dickson, M., Orchardo, J., Grootes, P., Mayewski, P.A., and Meese, D.A. (1994). Climate correlations between Greenland and Antarctica during the past 100,000 years. *Nature*, 372, 663-666.

Berger, A., and Loutre, M.F. (1991). Insolation values for the climate of the last 10 million of years. *Quat. Sci. Rev.*, 10, 4, 297-317.

Blunier, T., and Brook, E.J. (2001). Timing of millennial-scale climate change in Antarctica and Greenland during the last glacial period. *Science*, 291, 109-112.

Bond, G.C. and Lotti, R. (1995). Iceberg discharges into the North Atlantic on millennial time scales during the last glaciation. *Science*, 267, 1005-1010.

Broecker, W. S., Bond, G., Klas, M., Bonani, G. and Wolfi, W. (1990). A salt oscillator in the glacial North Atlantic? 1. The concept. *Paleoceanography*, 5, 469-477.

Broecker, W.S., Peteet, D.M., and Rind, D. (1985). Does the ocean-atmosphere system

have more than one stable mode of operation? *Nature*, 315, 2-26.

Campin, J.M. (1997). Modelisation tridimensinnelle de la circulation generale oceanique lors du dernier maximum glaciaire. PhD Thesis, Universite Catholique de Louvain, Louvain-la-Nueve, Belgium, 342pp.

Campin, J.M., and Goosse, H. (1999). A parameterization of density-driven downsloping flow for a coarse-resolution model in z-coordinate. *Tellus*, Ser. A, 51, 412-430.

Carcione, J.M. (2001). Wave Fields in Real Media: Wave Propagation in Anisotropic, Anelastic and Porous Media. 1st edn, pp. 1-15, Pergamon, New York.

Clark, P.U., Mitrovica, J., Milne, G., and Tamisiea, M. (2002). Sea-level fingerprinting as a direct test for the source of global meltwater pulse IA. *Science*, 295, 2438-2441.

Clark, P.U., Pisias, N.G., Stocker, T.F., and Weaver, A.J. (2002). The role of the thermohaline circulation in abrupt climate change. *Nature*, 415, 863-869.

Crampin, S. (1981). A review of wave propagation in anisotropic and cracked elastic media. *Wave Motion*, 3, 343-391.

Crampin, S. (1993). A review of the effects of crack geometry on wave propagation through aligned cracks. *Can. J. Expl. Geophys.*, 29, 3-17.

Crampin, S., Peacock, S., Gao, Y., and Chastin, S. (2004). The scatter of time-delays in shear-wave splitting above small earthquakes. *Geophys. J. Int.*, 156, 39-44.

Crampin, S., Volti, T., Chastin, S., Gudmundsson, A., and Stefansson, R., (2002). Indication of high pore-fluid pressures in a seismically-active fault zone. *Geophys. J. Int.*, 151, F1-F5.

Crampin, S., Zatsepin, S.V., Slater, C., and Brodov, L. (1996). Abnormal shear-wave polarizations as indicators of high pressures and over pressures. *58th Conf. EAGE. Amsterdam, Extended Abstracts*, 1. XO38.

Crouley, T. (1995). Ice age terrestrial carbon changes revisited. *Global Biogeochemical Cycles*, 9, 377-389.

Cushman-Roisin, B. (1994). Introduction to geophysical fluid dynamics. Prentice Hall, Englewood Cliffs, New Jersey, 320pp.

Dansgaard, W., Johnsen, S. J., Clausen, H. B., Dahl-Jensen, D., Gundestrup, N. S., Hammer, C. U., Hvidberg, C. S., Steffensen, J. P., Sveinbjörnsdottir, A. E., Jouzel, J., and Bond, G. (1993). Evidence for general instability of past climate from a 250kyr ice-core record. *Nature*, 264, 218-220.

Dansgaard, W., Johnson, S.J., Clausen, H.B., and Langway, C.C. (1971). Climatic record revealed by the Camp Century ice core. In "The Late Cenozoic Glacial Ages" (Turekian, K.K., ed.), pp. 37-56. Yale Univ. Press, New Haven.

Dansgaard, W., Clausen, H.B., Gundestrup, N., Hammer, C.U., Johnsen, S.F., Kristinsdottir, P.M., and Reeh, N. (1982). A new Greenland deep ice core. *Science*, 218, 1273-1277.

Draper, N.R. and Smith, H. (1998). Applied regression analysis. 3rd edn, pp. 505-566, A Wiley Interscience Publication, New York.

Deleersnijder, E., and Campin, J.M. (1995). On the computation of the barotropic mode of a free-surface World Ocean Model. *Ann. Geophys.,* 13, 675-688.

Deleersnijder, E., van Ypersele, J.P., and Capmin, J.M. (1993). An orthogonal curvilinear coordinate system for a World Ocean model. *Ocean Model*, 100, 7-10.

Elkibbi, M. and Rial, J.A. (2003). Shear-wave splitting: an efficient tool to detect 3D fracture patterns at The Geysers. *California. Proc., 28th Stanford Workshop on Geothermal Reservoir Engineering*, pp. 143-149, Stanford University, Stanford, CA.

Elkibbi, M., Yang, M. and Rial, J.A. (2004). The Geysers geothermal field: modeling crack-induced anisotropy in the subsurface. *Geophys. J. Int*., 162, 1036-1048.

Elliot, M., Labeyrie, L., and Duplessy, J.C. (2002). Changes in North Atlantic deep-water formation associated with the Dansgaard-Oschger temperature oscillations (60-110 ka). *Quat Sci. Rev.*, 21, 1153-1165.

Erten, D. and Rial, J.A. (1999). Extended studies of crack distribution and crack densities at NW Geysers. EOS AGU Spring Meeting, p. 101.

Fairbanks, R.G. (1989). A 17,000-year glacio-eustatic sea level record: influence of glacial melting rates on the Younger Dryas event and deep-ocean circulation. *Nature*, 342, 637-642.

Fichefet, T., and Morales Maqueda, M.A. (1997). Sensitivity of a global sea ice model to the treatment of ice thermodynamics and dynamics. *J. Geophys. Res*, 102, 12609-12646.

Ganachaud, A., and Wunsch, C. (2000). Improved estimates of global ocean circulation, heat transport and mixing from hydrographic data. *Nature*, 408, 453-457.

Ganopolski, A., and Rahmstorf, S. (2001). Radip changes of glacial climate simulated in a coupled climate model. *Nature*, 409, 153-158.

Ganopolski, A., and Rahmstorf, S. (2002). Abrupt glacial climate change due to stochastic resonance. *Phys. Rev. Let.*, 88 (3), 038501.

Gill, A.E. (1982). Atmosphere-Ocean Dynamics. International Geophysics Series, Volume 30, Academic Press, San Diego, 662pp.

Goosse, H., and Fichefet, T. (1999). Importance of ice-ocean interactions for the global ocean circulation: A model study. *J. Geophs. Res.*, 104, 23337-23355.

Goosee, H., Deleersnijder, E., Fichefet, T. and England, M.H. (1999). Sensitivity of a global coupled ocean-sea ice model to the parameterization of vertical mixing. *J. Geophys. Res.*, 104, 13 681-13 695.

Goosee, H., Renssen, H., Selten, F.M., Haarsma, R.J., and Opsteegh, J.D. (2002).

Potential causes of abrupt climate events: A numerical study with a three-dimensional climate model. *Geophys. Res. Let.*, 29, 1860, doi:10.1029/2002GL014993.

GRIP Project Members (1993) Climate instability during the last interglacial period recorded in the GRIP ice core. *Nature*, 364, 203-207.

Haarsma, R. J., Opsteegh, J.D., Selten, F.M., and Wang, X. (2001). Rapid transitions and ultra-low frequency behavior in a 40 kyr integration with a coupled climate model of intermediate complexity. *Climate Dynamics*, 17, 559-570.

Held, I.M. and Suares, M.J. (1978). A two-level primitive equation atmosphere model designed for climate sensitivity experiments. *Journal of Atmospheric Sciences*, 35, 206-229.

Holton, J.R. (1979). An introduction to Dynamic Meteorology. International Geophysical Series, Volume 23, 2nd edition, Academic Press, New York.

Hudson, J.A. (1980). Overall properties of a cracked solid. *Math. Proc. Camb. phil. Soc.*, 88, 371-384.

Hudson, J.A. (1981). Wavespeeds and attenuation of elastic waves in material containing cracks. *Geophys. J. R. Astr. Soc.*, 64, 133-150.

Hudson, J.A. (1986). A higher order approximation to the wave propagation constants for a cracked solid. *Geophys. J. R. Astr. Soc.*, 87, 265-274.

Hudson, J.A. (1988). Seismic wave propagation through material containing partially saturated cracks. *Geophys, J. R. astr. Soc.* 92, 33-37.

Hudson, J.A. (1990). Overall elastic properties of isotropic materials with arbitrary distribution of circular cracks. *Geophys. J. Int.*, 102, 465-469.

Hudson, J.A., Liu, E. and Crampin, S. (1996). Transmission properties of a fault plane. *Geophy. J. Int.*, 124,105-112.

Joos, F., and Prentice, I.C. (2004). A paleo-perspective on changes in atmospheric CO2 and climate. *The Global Carbon Cycle*, Held, C., and M. Raupach, Eds., Island Press, 165-186.

Joussaume S., and Taylor, K.E. (1995). Status of the Paleoclimate Modeling Intercomparison Project (PMIP). *Proc. 1st international AMIP scientific conference*, Monterey, USA, WCRP-95, 425-430.

Jouzel, J., Lorius, C., Petit, J.R., Genthon, C., Barkov, N.I., Kotlyakov, V.M., and Petrov, V.M. (1987). Vostok ice core: a continous isotope temperature record over the last climatic cycle (160,000 years). *Nature*, 329, 403-408.

Justino, F.B. (2004). The influence of glacial boundary conditions on the climate system during the Last Glacial Maximum. Ph.D. Thesis, der Mathematisch Naturwissenschaftlichen Fakultat, der Christian-Albrechts-Universitat, zu Kiel. pp119.

Kantha, L.H., and Clayson, C.A. (1994). An improved mixed layer model for geophysical applications. Journal of Geophysical Research, 99(C12), 25235-25266.

Kaspi, Y., Sayag, R., and Tziperman, T. (2004). A "triple sea-ice state" mechanism for the abrupt warming and synchronous ice sheet collapses during Heinrich events. *Paleooceanography*, 19, PA3004, doi:10.1029/2004PA001009.

Kerr, R.A. (2005). Confronting the bogeyman of the climate system. *Science*, 310,432-433.

Kirkpatrick, A., Peterson, J.E. and Majer, E.L. (1997). Three-dimensional compressional and shear-wave seismic velocity models for the Southeast Geysers geothermal field. *California. Proc., 22nd Stanford Workshop of Geothermal Reservoir Engineering*, pp. 399-410. Stanford University, Stanford, CA.

Knutii, R., Fluckiger, J., Stocker, T.F. and Timmermann, A. (2004). Strong hemispheric coupling of glacial climate through freshwater discharge and ocean circulation. *Nature*, 430, 851-856.

Lou, M. and Rial, J.A. (1997). Characterization of geothermal reservoir crack patterns using shear-wave splitting. *Geophysics*, 62, 487-495.

Lou, M., Shalev, E. and Malin, P.E. (1997). Shear-wave splitting and fracture alignments at the Northwest Geysers, California. *Geophys. Res. Let.*, 24, 1895-1898.

MacBeth, C. (1999). Azimuthal variation in p-wave signatures due to fluid flow. *Geophysics*, 64, 1181-1192.

Manabe, S., and Broccoli, A.J. (1985). The influence of continental ice sheets on the climate of an ice age. *J. Geophys. Res.*, 90(D1), 2167-2190.

Mann, M.E., Bradley, R.S., and Hughes, M.K. (1998). Global-scale temperature patterns and climate forcing over the past six centuries. *Nature*, 392, 779-787.

Marotzke, J. (1990). Instabilities and multiple equilibria of the thermohaline circulation. PhD Thesis, Institut fur Meereskunde, Kiel, pp126.

Marshall, S.J., and Clark, K.C. (1999). Modeling North America freshwater runoff through the last glacial cycle. *Quaternary Research*, 52, 300-315.

Marshall, S.J., and Molteni, F. (1993). Toward a dynamic understanding of planetary-scale flow regimes. *J. Atmos. Sci.*, 50, 1792-1818.

Mellor G.L. and Yamada, T. (1982). Development of a turbulence closure models for planetary boundary layers. Journal of Atmospheric Sciences, 31, 1791-1806.

McManus, J. F., Oppo, D.W. and Cullen, J.L. (1999). A 0.5-million-year record of millennial scale climate variability in the North Atlantic. *Science*, 283, 971-975.

Moberg, A., Sonechkin, D.M., Holmgren, Karin, Datsenko, N.M. and Karlen, W. (2005). Highly variable Northern Hemisphere temperatures reconstructed from low- and high-resolution proxy data. *Nature*, 433, 613-617.

Morales Maqueda M.A. (1995). Un modelo acoplado del hielo de mar y del oceano

superficial para estudios climaticos. PhD Thesis, Univesidad Complutense Madrid, Spain, 426pp.

Muller, R.A., and MacDonald, G.J. (2002). Ice ages and astronomical causes: Data, spectral analysis and mechanisms. Springer-Verlag press, 318 pp.

Oeschger, H., Beer, J., Siegenthaler, U., Stauffer, B., Dansgaard, W., and Langway, C.C. (1984). Late glacial climate history from ice cores. *Climate Processes and Climate Sensitivity, Geophys. Monogr.,* No. 29, Amer. Geophys. Union, 299–306.

Opsteegh, J. D., Haarsma, R.J., Selten, F.M., and Kattenberg, A. (1998). ECBILT: A dynamic alternative to mixed boundary conditions in ocean models. *Tellus*, 50A, 348-367.

Peacock, S. and Hudson, J.A. (1990). Seismic properties of rocks with distributions of small cracks. *Geophys. J. Int.*, 102, 471-484.

Pedlosky, J. (1979). Geophysical Fluid Dynamics. Springer Verlag, 710pp.

Peltier, W.R. (2004). Global glacial isostasy and the surface of ice-age Earth: the ICE-5G (VM2) model and GRACE. *Annual Review of Earth and Planetary Sciences*, 32, 111-149.

Peterson, L. C., Haug, G. H., Murray, R.W., Yarincik, K.M., King, J.W., Bralower, T.J., Kameo, K., Rutherford, S.D., and Pearce, R.B. (2000). Late Quaternary stratigraphy and sedimentation at site 1002, Cariaco Basin (Venezuela). *Proceedings of the ocean drilling program, scientific results*, Vol. 16, Leckie, R. M., Sigurdsson, H., Acton, G. D., and Draper, G., Eds., Ocean Drilling Program, 85-99.

Piotrowski, A.M., Goldstein, S.L., Hemming, S.R., and Fairbanks, R.G. (2005). Temporal relationships of carbon cycling and ocean circulation at glacial boundaries. *Science*, 307, 1933-1938.

Power S. B. and Kleeman, R. (1994). Surface flux parameterization and the response of OGCMs to high latitude freshening. *Tellus*, 46A, 86-95.

Rahmstorf, S. (2002). Ocean circulation and climate during the past 120,000 years.

Nature, 419, 207-214.

Rahmstorf, S. (2006). Thermohaline ocean circulation. *Encyclopedia of Quaternary Sciences*, Elias, C. A., Eds., Elsevier.

Raymo, M. E., Ganley, K., Carter, S., Oppo, D.W., and McManus, J. (1998). Millennial-scale climate instability during the early Pleistocene epoch. *Nature*, 392, 699-702.

Roemmich, D.H., and Wunsch, C. (1985). Two transatlantic sections: Meridional circulation and heat flux in the subtropical North Atlantic Ocean. *Deep-sea Research*, 32, 619-664.

Rial, J.A. (1999). Pacemaking the ice ages by frequency modulation of earth's orbital eccentricity. *Science***,** 285, 564-568.

Rial, J.A. (2003). Abrupt climate change: Chaos and order at orbital and millennial scales.
Global and Planet. Change, 41, 95-109.

Rial, J.A. (2004). Evidence for control of the Pleistocene ice ages by changes in earth's orbital eccentricity: The concealed pacemaker. *Global and Planet. Change*, 41, 81-93.

Rial, J.A. and Anaclerio, C.A. (2000). Understanding nonlinear responses of the climate system to orbital forcing. *Quaternary Science Reviews*, 19, 1709-1722.

Rial, J.A., and Lou, M. (1996). Fracture orientation and density from inversion of shear-wave splitting at the Coso, CA, geothermal reservoir. EOS AGU Spring Meeting.

Rial, J.A., Pielke Sr., R. A., Beniston, M., Claussen, M., Canadell, J., Cox, P., Held, H., de Noblet-Ducoudré, D., Prinn, R., Reynolds, J.F., and Salas, J.D. (2004). Nonlineairities, Feedbacks and Critical Thresholds within the Earth's Climate system. *Climatic Change***,** 65 , 11-38.

Rial, J.A., and Yang, M., (2006). Can abrupt climate change be anticipated? Submitted to *J. Climate*.

Romero, A.E. (1995). Application of seismic tomographic techniques in the investigation of geothermal systems. PhD Thesis, University of California,Berkeley, 155p.

Sachs, J. P., and Lehman, S.J. (1999). Subtropical North Atlantic temperatures 60,000 to 30,000 years ago. *Science*, 286, 756-759.

Sakai, K., and Peltier, W.R. (1995). A simple model of the Atlantic thermohaline circulation: Internal and forced variability with paleoclimatological implications. *J. Geophys. Res.*, 100(C7), 13 455-13 479.

Sakai, K., and Peltier, W.R. (1997). Dansgaard-Oeschger oscillations in a coupled atmosphere-ocean climate model. *J. Climate*, 10, 949-967.

Saltzman, B. (2002). Dynamical Paleoclimatology. Academic Press, 320 pp.

Saltzman, B., and Moritz, R. (1980). A time-dependent climatic feedback system involving sea-ice extent, ocean temperature, and CO2. *Tellus*, 32, 93-118.

Sandstrom, J. W. (1908). Dynamische Versuche mit Meerwasser. *Ann. Hydrogr. Marit. Meteorol.* 36, 6-23.

Sarnthein, M., Winn, K., Jung, S., Duplessy, J.C., Labeyrie, L., Erlenkeuser, H., and Ganssen, G. (1994). Changes in east Atlantic deepwater circulation over the last 30,000 years: eight time slice reconstructions. *Paleooceanography*, 9, 209-267.

Schoenberg, M. and Sayers, C.M. (1995). Seismic anisotropy of fractured rock. *Geophysics*, 60, 204-211.

Schulz, H., von Rad, U., and Erlenkeuser, H. (1998). Correlation between Arabian Sea and Green-land climate oscillation of the past 110,000 years. *Nature*, 393, 54-57.

Seber, G.A.F., and Wild, C.J. (1989). Nonlinear Regression. pp. 21-23, 588-599, Wiley Series in Probability and Mathematical Statistics, New York.

Severinghaus, J. P. and Brook, E.J. (1999). Abrupt climate change at the end of the last glacial inferred from trapped air in polar ice. *Science*, 286, 930-934.

Stauffer, B., Fluckiger, J., Monnin, E., Schwander. J., Barnola, J.M., and Chappellaz, J. (2002). Atmospheric CO2, CH4 and N2O records over the past 60000 years based on the comparison of different polar ice cores. *Annals of Glaciology*, 35, 202-208.

Stocker, T., (2001). Nonlinearities in the earth system: The ocean's role. *Geosphere-Biosphere Interactions and Climate*, Bengtsson, L. D., and C. U. Hammer, Eds., Springer, 147-162.

Stommel, H. (1961). Thermohaline convection with two stable regimes of flow. *Tellus*, 13, 224-230.

Talley, L.D., Reid, J.L., and Robbins, P.E. (2003). Data-based meridional overturning streamfunctions for the global ocean. *Deep-Sea Research*, 42, 477-500.

Tarasov, L. and Peltier, W.R. (2005). Arctic freshwater forcing of the Younger Dryas cold reversal. *Nature*, 435, 662-665.

Taylor, K. C., Mayewski, P.A., Alley, R.B., Brook, E.J., Gow, A.J., Grootes, P.M., Meese, D.A., Saltzman, E.S., Severinghaus, J.P., Twickler, M.S., White, J.W.S., Whitlow, S., and Zielinski, G.A. (1997). The Holocene-Younger Dryas transition recorded at Summit, Greenland. *Science*, 278, 825-827.

Vlahovic, G., Elkibbi, M., and Rial, J.A. (2002). Shear-wave splitting and reservoir crack characterization: the Coso geothermal field. J. Volcanology and Geothermal Res., 120, 123-140.

Veum T., Jansen, E., Arnold, M., Beyer, I., and Duplessy, J.C. (1992). Water mass exchange between the North Atlantic and the Norwegian Sea during the past 28,000 years. *Nature*, 356, 783-785.

von Storch, H., Zorita, E., Jones, J.M., Dimitriev, Y., González-Rouco, F., and Tett, S.F.B. (2004). Reconstructing past climate from noisy proxy data. *Science*, 306, 679-682.

Wang Y. J., Cheng, H., Edwards, R.L., An, Z.S., Wu, J.Y., Shen, C.C., and Doral, J.A.A. (2001). A high-resolution absolute-dated late Pleistocene monsoon record from Hulu Cave, China. *Science*, 294, 2345-2348.

Wang, Z., and Mysak, L.A. (2006). Glacial abrupt climate changes and Dansgaard-Oeschger oscillations in a coupled climate model. *Paleoceanography*, 21, PA2001, doi:10.1029/2005PA001238.

Weaver, A. J., and Sarachik, E.S. (1991). The role of mixed boundary conditions in numerical models of the ocean's climate. *J. Phys. Oceanogr.*, 21, 1470-1493.

Winton, M. (1997). The effect of cold climate upon North Atlantic deep water formation in a simple ocean-atmosphere model. *J. Climate*, 10, 37-51.

Winton, M., and Sarachik, E.S. (1993). Thermohaline oscillations induced by strong steady salinity forcing of ocean general circulation models. *J. Phys. Oceanogr.*, 23, 1389-1410.

Wright, D. G. and Stocker, T.F. (1991). A zonally-averaged model for the thermohaline circulation. Part I: model development and flow dynamics. *J. Phys. Oceanogr.*, 21, 1713-1724.

Wunsch, C. (2000). Moon, tides and climate. *Nature*, 405, 743-744.

Wunsch, C. (2002). What is the thermohaline circulation. *Science*, 298, 1179-1180.

Yang, M., and Rial, J.A. (2006). Internal oscillations of the thermohaline circulation and the Dansgaard-Oeschger events of the last ice age. submitted to *J. Climate*.

Zatsepin, S.V. and Crampin, S. (1997). Modelling the compliance of crustal rock – I. Response of shear-wave splitting to differential stresses. *Geophys. J. Int.*, 129, 477-494

Zhang S., GreatBach, R.J., and Lin, C.A. (1993). A reexamination of the polar halocline

catastrophe and implications for coupled ocean-atmosphere modeling. *J. Phys. Oceanogr.*, 23, 287-299.

Zhao, M., Beveridge, N.A.S., Shackleton, N.J., Sarnthein, M., and Eglinton, G. (1995). Molecular stratigraphy of cores off Northwest Africa: sea surface temperature history over the last 80ka. *Paleooceanography*, 10, 661-675.